PSFC/RR-04-2 **DOE-ET-54512-350**

Design of an ICRF Fast Matching System on Alcator C-Mod

A. Parisot

September 2004

Plasma Science and Fusion Center
Massachusetts Institute of Technology
Cambridge MA 02139 USA

This work was supported by the U.S. Department of Energy, Cooperative Agreement No. DE-FC02-99-ER54512.

Design of an ICRF Fast Matching System on Alcator C-Mod

by

Alexandre Parisot

Submitted to the Department of Electrical Engineering and Computer Science
in partial fulfillment of the requirements for the degree of

Master of Science in Electrical Engineering

at the

MASSACHUSETTS INSTITUTE OF TECHNOLOGY

January 2004

Author . . . . . .
Department of Electrical Engineering and Computer Science
January, 20th 2004

Certified by . . . . . .
Stephen J. Wukitch
Research Scientist
Thesis Supervisor

Certified by . . . . . .
Ronald R. Parker
Professor, Electrical Engineering and Nuclear Engineering
Thesis Supervisor

Accepted by . . . . . .
Arthur C. Smith
Chairman, Department Committee on Graduate Students

Design of an ICRF Fast Matching System on Alcator C-Mod

by

Alexandre Parisot

Submitted to the Department of Electrical Engineering and Computer Science
on January, 20th 2004, in partial fulfillment of the
requirements for the degree of
Master of Science in Electrical Engineering

Abstract

In Ion Cyclotron Radiofrequency Heating (ICRH) for tokamaks, fast variations of the antenna loading impedance limit flexible and robust high-power operations. In this thesis, novel solutions for real-time matching and reduction of these variations are investigated and studied for implementation on the Alcator C-Mod tokamak. Load tolerant prematching networks are reviewed and a prototype configuration for E-antenna is proposed. By maintaining low voltage standing wave ratio in the network for a wide range of loading conditions, it could allow robust high power operations without the need of fast matching. However, typical conditions could create current imbalance effects ; the performance of the system could be degraded and the phasing between the antenna affected, with side-effects on the overall behavior of the antenna in plasma. Another possible option for real-time matching uses ferrite loaded transmission lines, whose electrical length could be varied over timescales as fast as a few milliseconds. A potential ferrite material is identified and experimentally characterized in a small-scale low power experiment. This leads to design guidelines for a high power ferrite phase shifter and a fast-matching network using such tuners.

Thesis Supervisor: Stephen J. Wukitch
Title: Research Scientist

Thesis Supervisor: Ronald R. Parker
Title: Professor, Electrical Engineering and Nuclear Engineering

Acknowledgments

Throughout this work, I have received much help and support from quite a few people.

I would like to thank first the entire Alcator C-Mod team, and especially Yijun Lin, Paul Bonoli, Charles Schwartz, Richard Murray, William Beck, Valerie Censabella, Ed Fitzgerald, Andy Pfeifer, Sam Pierson, Megan Tabak, Bruce Lipschutz, David Terry, Rui Viera, Jim Irby, Steve Wolfe and Professor Miklos Porkolab, with whom I had the chance to work more directly. Special thanks to Makoto Takayasu, who gave me access to his facility and magnets and offered a great assistance in setting up experiments. Very special thanks to Peter Koert, with whom I worked closely on this project, and whose advice, intuition and experience were always unvaluable.

I also owe thanks to my fellow graduate students Eric, Tim, Liang, Davis, Vincent, John, Brian, Balint, Brock, Kirill, Howard, Jerry, Jennifer, Will, Joan... With them I have shared the very special experience of graduate studies, as labmates, classmates and foremost, as friends. I am indebted to Professor Molvig and Professor Freidberg for introducing me to the subtilties of plasma and tokamak physics. Niels Basse also contributed to this work indirectly, by regularly and gradually improving my squash skills.

Above all I wish to thank my advisor Professor Ron Parker, for his endless and continuous support, help and guidance during this year and a half. And Steve Wukitch for his supervision, his availability, his constant encouragements and his extraordinary patience in any situation. Both have given me the motivation to reach this point and to go beyond it, towards a doctorate degree.

Contents

List of Figures

List of Tables

Chapter 1

Background and motivations

As physics explored the structure of matter and the interactions which bind its different constituents, new methods to produce and use energy were successively discovered; they drove and allowed in return sustained industrial and technological development. Fusion is now standing as the current frontier in this process. While its military applications - the hydrogen bomb - followed quickly the Second World War and the first use of fission reactions, research on *controlled* fusion for energy production is still well under way. Fifty years of intense scientific work, after the early attempts of Dr. Lyman Spitzer in the 50's, showed the tremendous difficulty of the effort. Numerous theoretical, experimental and technological problems were encountered, many experimental devices built all over the world and much resources spent in a challenging attempt to use on Earth this energy that powers the stars. So far, although no scientific evidence suggests that using fusion for energy production is *un*feasible, practical applications are still out of our reach and might well be for a least another thirty to fifty years.

Yet, fusion energy appears more and more as a critical need for our future. All the other sources of energy have limitations in terms of available fuel, production potential or ecological side-effects, while fusion provides electricity and hydrogen fuel very effectively from a virtually infinite reservoir - water - and with little or at least controllable impact of the ecosystem. At the present rate of industrial, economic and population growth, and given the current effects of other sources and estimated resources, major energy shortages and significant changes in the earth ecological parameters are extremely likely to start occurring

within the next fifty years. Although not easy to achieve, fusion energy is an attractive potential solution, and certainly the only one if drastic measures are not taken to reduce significantly the world energy consumption.

This work deals with a very specific and narrow aspect of current fusion research. Although modest, it may help bringing this whole effort a step closer to its goal - as did and do all the previous and present contributions of the scientists, engineers, technicians in the fusion community.

1.1 Fusion and tokamaks

1.1.1 Fusion energy

Fusion reactions involve bringing together two atomic nuclei. For controlled fusion applications, the most promising involves deuterium and tritium nuclei :

$$D + T \rightarrow He^4 + n^1(+17.6MeV)$$

In this process, 17.6 MeV from nuclear forces are transferred into kinetic energy of the reaction products, but the mutual electrostatic repulsion of the nuclei must be overcome to bring them close enough during a sufficient time for the reaction to occur. This can be achieved by heating a melange containing deuterium and tritium to high temperatures, thus using the thermal velocity to provide the initial energy. The technique is called *thermonuclear* fusion and requires about 10 keV (figure 1-1).

At these temperatures, the melange is fully ionized and forms a plasma, which must be confined to counteract its rapid thermal expansion. Two techniques are currently being investigated : inertial and magnetic confinement. In *inertial* confinement fusion, the D-T melange, initially solid, is embedded into a solid capsule. Typically, a short-pulse high energy laser beam is used to heat the capsule surface and trigger its rapid expansion both outward and inward, which compresses the D-T solid up to pressures and temperatures required for fusion. In *magnetic* confinement, magnetic fields are used to maintain the plasma at the center of the device chamber and away from its walls, allowing sufficient

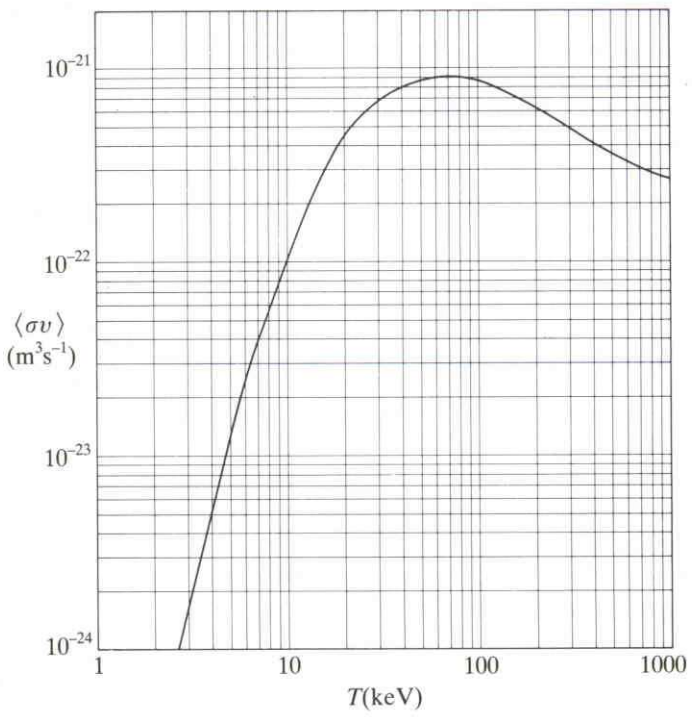

Figure 1-1: Reaction rate for DT reactions as a function of temperature. From [1]

densities and temperatures to be reached. By nature, this technique can potentially lead to steady-state self-maintained fusion.

1.1.2 Magnetically confined thermonuclear fusion devices

Determining appropriate magnetic geometries for confinement is not a straightforward issue. Constraints are present for the two possible sources of magnetic field in the plasma - the sets of external coils and the plasma current itself. As the temperature is increased, significant losses can also occur along the field lines in the magnetic mirror geometry. Historically, these runaway losses, along with various instabilities, limited the maximum temperature and confinement time in early magnetic mirror machines.

As the American and European fusion program in the 60's struggled to improve the peak temperatures $\approx$ 100 eV in mirror machines, Russian scientists reported achieving temperatures of $\approx$ 1 keV in a toroidally symmetrical device, the *tokamak*, an acronym of *toroidal magnetic chamber* in Russian. The torus geometry with a mainly toroidal magnetic field allows field lines to remain in the plasma volume and therefore limits the runaway

losses to very high energy particles. But the price to pay is a much more complicated physical and magnetic geometry. The equilibrium and stability for the plasma require complex coil configurations and limits the operating conditions of tokamaks to specific regimes. The magnetohydrodynamics (MHD) model has helped gain much intuition and understanding on the underlying physics and has allowed optimization toward better characteristics for fusion. Very successful and promising tokamak operation has been obtained, so that now its design appears as the most likely candidate for commercial fusion devices. As part of the International Thermonuclear Experimental Reactor (ITER) project, ignition should be achieved in a large-size tokamak which is expected to produce thermal energy at the level of an electricity-producing power station. This might be the next and single major step before our level of experience and understanding allow us to build a demonstration electricity-generating power plant (DEMO).

Based on MHD considerations, the magnetic configuration (figure 1-2) used by most present tokamak and retained for the ITER design is a combination of a large toroidal magnetic field $\sim$ 2-8 Tesla, a smaller poloidal field generated by the toroidal current in the plasma, a vertical field used to control its radial position and different fields which help modifying its shape. A central primary coil is used to generate and control the plasma current. Additional geometrical constraints are associated with the plasma-wall interactions, which can lead to contamination of the plasma volume by metal impurities from the walls. The diverted configuration, with its characteristic magnetic x-point in the torus cross-section, is used to prevent the plasma interior from being in direct contact with a solid surface.

1.2 Auxiliary heating and Ion Cyclotron Radio-frequency Heating

1.2.1 Necessity of auxiliary heating

As seen above, the fusion rate is a strong function of temperature. In tokamaks, some form of heating must therefore be provided before the device can reach *burning plasma*

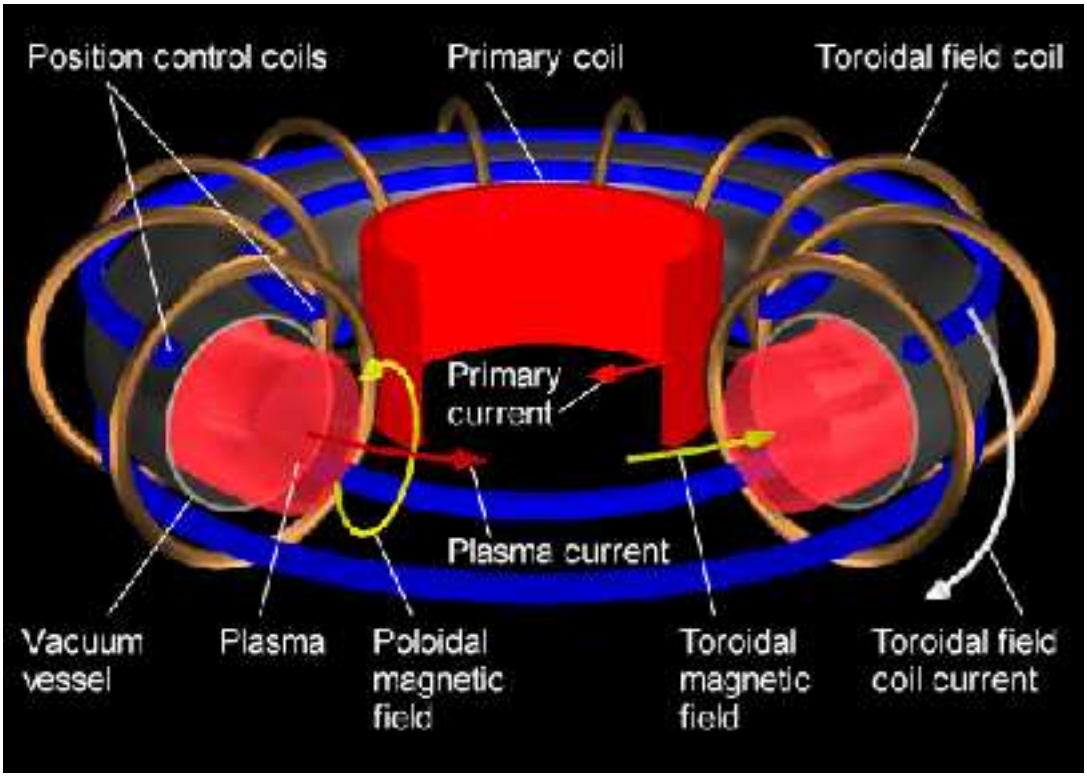

Figure 1-2: Schematic drawing of a tokamak.

conditions, in which the self-heating from of α-particles resulting from the fusion reactions can balance the power losses.

To increase the plasma temperature close to ignition level, auxiliary heat must be supplied to the plasma. In a tokamak, the toroidal current provides a natural source of plasma heating, called *ohmic* heating, through the resistance of the plasma, which stems mainly from ion-electron collisions. At low temperatures, ohmic heating can quite strong, but as the ion-electron collision frequency scales as $T^{-3/2}$, it decreases strongly as the temperature increases. As losses increase with temperature, ohmic heating has therefore intrinsic limitations.

A simple calculation can give an order of magnitude of the maximum temperature in ohmically heated plasmas. Using the Spitzer resistivity and assuming a flat current profi le in a circular plasma torus, we can write the ohmic heating power :

$$P_{ohmic} = \eta j^2 V_{torus} = \eta j^2 2\pi^2 R a^2 = 2\eta I^2 \frac{R}{a^2}$$

with $\eta \approx 8 \times 10^{-8} T_e^{-3/2}$ the Spitzer resistivity for a pure deuterium plasma, R the major radius, a the minor radius, I the total current and j the current density, T_e the electron temperature in keV.

For the prospective ITER parameters, T_e = 1 keV and I = 21 MA, this gives $P_{ohmic} \approx 70MW$. For T_e = 10 keV, the ohmic heating is signifi cantly reduced $P_{ohmic} \approx 2.3MW$. The radiation and particles losses can be estimated using empirical scalings for the energy confi nement time, $P_{losses} = \frac{3nT}{\tau_E} V_{torus}$, where n is the plasma density. For ITER, we can take $\tau_E \sim 6s$ and $n = 10^{20} m^{-3}$, so that $P_{losses} = P_{ohmic}$ gives $T \sim 3.2keV$.

This is of course a simple estimation, and in practice, more complicated scalings or values for the resistivity and the energy confi nement time with non-uniform current profi les and impurities have to be taken into account. Yet, it turns out that the maximum temperature achievable through ohmic heating for reactor-size devices remains of the same order. The $T^{-3/2}$ dependence of the resistivity is dominant over the other parameters. In order to reach ignition in a reactor, auxiliary heating sources are therefore required. Neutral beams can be used to introduce fast ions in the plasma and the resulting slowing down transfers the beam energy to the plasma bulk. Another possibility is to use radiofrequency waves launched from the vessel and penetrating into the plasma, where the wave energy can be transferred to the different species in certain conditions. The ion cyclotron radiofrequency heating (ICRH) is one such scheme.

1.2.2 ICRF Heating

The ion cyclotron radiofrequency heating technique takes profi t of the damping encountered by electromagnetic waves as the wave frequency is close to the cyclotron frequency of plasma ion species, which is a associated to their gyration movement in a magnetic fi eld. It has proved very effective for ion heating and presently most of the large and medium-sized tokamaks use multi-megawatt ICRF systems for this purpose. The current status of ICRF physics and technologies will be reviewed in chapter 2, and we summarize here the main points to introduce the objective of this thesis work.

Presently, good theoretical models are available to study and predict wave absorption in

the plasma core, and conditions for good absorption have been determined and successfully realized in experiments. Some issues remain and the complexity of the problem requires numerical treatment, but there is good confi dence that the underlying physics is mostly understood, with fair predictive capabilities. The most promising scheme to date uses the fast magnetosonic wave, which can be launched by inductive loop antennas. Present antenna designs have achieved relatively good performance, and techniques have been developed to avoid the problems of impurity production or parasitic coupling that occured in early ICRF experiments. While it is still diffi cult today to predict the effective performance of an antenna design in plasma conditions, most ICRF experiments have been able to reach the point where the antenna geometry and behavior in plasma is no longer the limiting factor for the maximum heating power. Rather, the performance is presently set by available impedance matching techniques. As the fast wave coupling to the tokamak plasma is imperfect and depends on conditions at the edge, the loading resistance of the antenna is often low and rapidly varying. The large mismatch between the generator and antenna impedances result in very high voltages in the transmission line network, and electrical breakdown limits the maximum power which can be transferred to the plasma.

In this work, novel techniques for impedance matching are investigated and possible designs are proposed for the ICRF system in the Alcator C-Mod tokamak. While these upgrades are expected to improve the effi ciency and robustness of the ICRF system in C-Mod, this study is also relevant for future ICRF designs, as novel techniques could be evaluated during tokamak operation in C-Mod. This thesis summaries the approach, results and conclusions, with the following outline :

- Chapter 2 reviews briefly the present status of ICRF physics and technologies, and presents existing impedance matching systems

- Chapter 3 presents the Alcator C-Mod tokamak and its present ICRF system, and reviews novel techniques for impedance matching for C-Mod.

- Chapter 4 is a study of *load tolerant* confi gurations, with a proposed design for experimental test and evaluation on Alcator C-Mod

- Chapters 5, 6 and 7 present the investigation of ferrite-loaded stripline tuners for fast impedance matching system, and the design of a system using such tuners for Alcator C-Mod.
- Chapter 8 concludes the thesis and gives indications for further work.

Chapter 2

ICRH Physics and Technologies

2.1 ICRH Physics

2.1.1 Wave absorption in the ICRF range of frequencies

Waves propagation in tokamak plasma is often very complicated. In general, different species are involved, and the plasma has inhomogeneous two or three-dimensional density, temperature and magnetic field profiles. In addition, the geometry of the tokamak vessel is far from being simple, leading to complex boundary conditions. The response of the plasma species to the wave excitation involves relaxation effects, damping or growth of the wave near resonances. Plasma oscillations are associated with the inertial relaxation of charged species in order to restore quasi-neutrality, and occur at the plasma frequency $\omega_p = \sqrt{\frac{n(Ze)^2}{m\epsilon_0}}$. The magnetic field introduces gyration effects with the characteristic cyclotron frequency $\Omega = \frac{ZeB}{m}$. As the phase velocity of waves approaches the harmonics of cyclotron frequencies for the different particles, resonance effects occur. Velocity distribution functions, sometimes different from the usual Maxwellian form, have to be taken into account in the treatment of these effects and this altogether makes most practical situations only approximately tractable with analytical approaches ; numerical codes are required to obtain more accurate and detailed predictions.

Yet, much intuition and understanding of wave propagation and absorption can still be gained from simplified models. For instance, one can treat the plasma as a zero-temperature

frictionless fluid of ions and electron, approximatively charge neutral, homogeneous in space and immersed in a uniform static magnetic field. In this model, called *cold plasma model*, the wave equation becomes :

$$k \times (k \times E) + \frac{\omega^2}{c^2} \epsilon . E = 0$$

where ϵ is the cold plasma dielectric tensor for a magnetic field along the z axis :

$$\epsilon = \begin{vmatrix} S & -iD & 0 \\ iD & S & 0 \\ 0 & 0 & P \end{vmatrix}$$

$$S = \frac{1}{2}(R + L), D = \frac{1}{2}(R - L)$$

$$R = 1 - \sum_s \frac{\omega_{ps}^2}{\omega(\omega + \Omega_s)}$$

$$L = 1 + \sum_s \frac{\omega_{ps}^2}{\omega(\omega - \Omega_s)}$$

$$P = 1 - \sum_s \frac{\omega_{ps}^2}{\omega^2}$$

and the summation index s corresponds to the different species. In the ion cyclotron range of frequencies, $R \approx \sum_{ions} \frac{\omega_{pi}^2}{\omega(\omega+\Omega_i)}$ and $L \approx \sum_{ions} \frac{\omega_{pi}^2}{\omega(\omega-\Omega_i)}$.

With these notations, the wave equation can be written, assuming $k_y = 0$ for simplicity :

$$\begin{vmatrix} S - n_\parallel^2 & -iD & n_\parallel n_\perp \\ iD & S - n_\parallel^2 - n_\perp^2 & 0 \\ n_\parallel n_\perp & 0 & P - n_\perp^2 \end{vmatrix} \begin{vmatrix} E_x \\ E_y \\ E_z \end{vmatrix} = 0$$

where we introduced $n_\parallel = \frac{c}{\omega} k_\parallel$ and $n_\perp = \frac{c}{\omega} k_\perp$.

The dispersion relation is obtained by taking the determinant, leading to :

$$n_\perp^4 S + n_\perp^2 (D^2 - (S - n_\parallel^2)(S + P)) + P((S - n_\parallel^2)^2 - D^2) = 0$$

When the two solutions are well separated, they can be written, with $|S|, |D| \ll |P|$:

$n_\perp^2 = \frac{(S-n_\parallel^2)^2 - D^2}{S - n_\parallel^2 - \frac{D^2}{P}} \approx \frac{(S-n_\parallel^2)^2 - D^2}{S - n_\parallel^2}$ Fast magnetosonic wave

$n_\perp^2 = \frac{P}{S}(S - n_\parallel^2) - \frac{D^2}{S} \approx \frac{P}{S}(S - n_\parallel^2)$ Slow wave

The approximate expressions correspond to $|\frac{D}{P}\frac{D}{S-n_\parallel^2}| \ll 1$, and can be used away from the $S = n_\parallel^2$ layer.

At least two properties of the fast magnetosonic waves make it a very good candidate for radio-frequency heating :

First, its polarization is such that the $E_\parallel$ component of the wave is always small. In contrary, the slow wave can encounter a resonance - the ion-ion hybrid resonance - near the plasma edge where the density is low, and there the shielding effects of the electrons is insuffi cient so that large $E_\parallel$ components are present. We will see the undesirable consequences of this large parallel electric fi eld in the next section. As the fast wave is primarily a wave with strong $E_\perp$ component, it can be launched quite effectively by antennas presenting poloidal currents to the plasma.

Second, the fast wave can be extremely well damped or converted into other well-damped waves in the plasma core. The relevant parameter to quantify this effect is the *single-pass absorption* which measures the absorbed fraction of the incident power on the absorption region for one pass only, before subsequent reflection of the unabsorbed wave on reflecting cut-off layers or on the vessel walls. Good absorption conditions can be obtained from different schemes, which are now discussed:

Ion cyclotron absorption

The ion cyclotron resonance provides conditions for good absorption depending on the composition of the plasma and the temperature. As the cyclotron frequency increases with the magnetic fi eld, the regions where resonance effects occur depend on magnetic fi eld profi le. The toroidal fi eld is dominant and varies with a good approximation as the inverse of the major radius, therefore defi ning cylindrical resonant surfaces, where for the cyclotron

frequency or its harmonics equals the frequency of the fast wave. Spatial localization for absorption regions can therefore be controlled effectively. However, at low or moderate temperatures, no absorption is encountered at the first harmonics resonance surface for ion species with high concentration. This effect is due to the right-hand polarization of the fast wave at the cyclotron resonance, opposite to the free ion motion. Good absorption can be obtained with high $k_{||}$ waves for higher plasma temperatures, however. Alternatively, higher harmonics of the cyclotron frequency can also be used for heating.

An alternative scheme using ion cyclotron absorption of the wave can be used with a multi-species plasma. If an ion species with low concentration (*minority*) is present in a plasma containing other species (*majority* species) with higher concentration, the fast wave can be strongly damped on the minority ions at their resonance surfaces. The single pass absorption reaches a maximum for a certain minority fraction, usually a few percent.

Direct electron absorption. Mode conversion.

If the plasma temperature is high enough, direct absorption by bulk electrons can be significant. Transfer of energy from the wave to the electrons can also result from conversion of the fast wave to different waves or modes, like the slow wave, Ion Bernstein wave and Ion Cyclotron wave, which damp strongly on electrons in the plasma core.

These different process allow effective transfer of energy from the wave to the plasma species under a wide range of conditions.

However, fast wave heating techniques are impeded by the presence of an evanescent layer at low plasma densities, as can be seen from the dispersion relation (see [4]). This problem and its practical consequences will be examined in section 2.2. Another practical limitation of fast wave heating is related to *antenna-plasma* interactions.

2.1.2 Antenna-plasma interactions

Early experiments using ICRF antennas reported strong density rise and impurity influxes during ICRF pulses [5] ; the effect could be severe enough to lead to disruptive termination of the discharges. In order to avoid direct contact between the antenna straps and the

plasma, and to lower the coupling to the slow wave, a Faraday shield was installed in front of the antenna box, and it was found to have a positive effect on impurity production and heating efficiency during ICRF for low power experiments. Vacuum conditioning of the antenna and wall conditioning were also found to improve the antenna performance. One of the most important parameters of antenna-plasma behavior, however is the antenna phasing [6] [7]. Two strap or four-strap antennas with adjacent straps driven out of phase have impurity influxes as low as 2% of those in the dipole case, when current straps are driven in phase. The empirical observations above allowed somewhat controlled edge-antenna interactions during ICRF and therefore successful operations of the antennas. The limiting factor for the heating power is now often breakdown limits in the antenna structure or in the transmission line network, as will be presented in the next section, and antennas can operate with little parasitic effect on the plasma discharge.

Different mechanisms have been investigated to explain the observations above. We describe them below, for the low single pass absorption case and the high single pass absorption case.

Low single pass absorption : parasitic modes and far field sheaths [8]

If the single pass absorption is low, the following effects may occur:

(i) The fast wave is not completely absorbed on one pass and therefore encounters the walls or limiters either directly or after multiple reflections on cutoff surfaces.

(ii) Slow waves modes are be generated at the wall or directly for the antenna (screenless operations).

(iii) Waves with strong $E_{||}$ components (slow wave, surfaces modes, etc...) drive RF sheaths (see the good single pass absorption section).

All these effects result in increased impurity release from the walls or the limiters. The dependence on the antenna phasing is due to the fact that waves with higher $k_{||}$ are better absorbed in the plasma core, and therefore out of phase phasing should result in higher single pass absorption than in the dipole case.

Good single pass absorption : near field effects, impurity release from the Faraday Shield [9]

Electrons accelerated by the $E_{||}$ fields lead to rectified sheaths restoring the quasi-neutrality. The associated potentials also have strong gradients in the perpendicular direction, and the resulting electric fields drive E $\times$ B convection. As a result of this, ions can be accelerated with energies $Ze\Phi$ above the sputtering yield of the sheath limiter components. The impurity release is therefore increased. For high single pass absorption, parasitic waves launching can be minimal compared to the net power in the fast wave ; however, as presented in [10], $E_{||}$ fields can be generated by r.f. flux linkage in circuits connecting two points of the Faraday shields along the field line - the alignment of the shield with the field lines is impossible in practice for all operating condition . This results in significant impurity release from the Faraday shield itself. By operating with adjacent straps out of phase, the flux linkage potentials can be canceled or reduced and the impurity release from the shield can be brought down to negligible numbers compared to the dipole phasing.

For high single pass absorption tokamaks, far field effects are minimal, and by driving adjacent straps out of phase, near field effects can be effectively minimized. Therefore, there is little parasitic effect on the discharge, and the most important limitations of the present system arise from impedance matching considerations.

2.2 Impedance matching techniques

2.2.1 The impedance matching problem in ICRH systems

Wave absorption in the ICRF range of frequencies is presently well understood, at least to the extent that conditions for strong absorption of the fast wave are known and can be realized experimentally. However, before reaching the ion cyclotron resonance or mode conversion layer in the plasma core, the fast wave must be launched effectively from the antenna structure. As can be seen from the dispersion relation [4] of the fast wave, an evanescent region is always present in the space between the absorption region and the antenna. The antenna straps are typically isolated from the plasma, and the wave must

tunnel through this region before reaching a sufficiently dense plasma where propagation towards the core can occur.

Even with strong single pass absorption, this imperfect coupling limits the amount of power which can be transferred to the plasma for given strap currents. A significant fraction of the power used to maintain the current distribution on the straps is therefore reflected back toward the generator. This situation is equivalent to the effect of a mismatched termination in the transmission line network, and a commonly used model substitutes the antenna with a lumped load with impedance $Z_{ant} = R + jX$. Typically R $\sim .5 - 20\Omega$. The characteristic impedance of the coaxial lines in the network is usually chosen to maximize either the power-carrying capabilities or the breakdown voltage limits, therefore setting Z_0 in the 25-50 Ω range.

This low resistive loading $R \ll Z_0$ results in high voltage standing wave ratio in the lines and potentially at the generator output, which strongly reduce its efficiency. To avoid this undesirable situation, an impedance matching network has to be inserted in the network to isolate the generator from the load. The mismatch can be then effectively reduced on the generator side, but while the net power from the generator equals the power coupled to the plasma at the antenna in steady-state, a significantly higher circulating power is present between the antenna and the impedance matching network, with high VSWR in this section. Electrical breakdown is very likely to occur in the corresponding coaxial lines. Even if the match can be performed as close as possible to the antenna structure, this limits in practice the maximum power which can be transferred to the plasma.

Another complication arises from the variations in the antenna loading impedance Z_{ant}. Significant and rapid changes in the conditions at the edge of the plasma are frequent in tokamak operation and it is not clear to date if enough operating range flexibility will be available for final fusion devices in order to avoid these effects. The transition between L and H confinement modes is the source of sudden increases or decreases in the loading resistance, related mainly to the abrupt evolution of the edge density profiles [11]. It occurs on timescales as fast as 10^{-4} seconds (figure 2-1). Another source of loading impedance variations is Edge Localized Mode activity.

Presently, most impedance matching networks are adjustable only between discharges

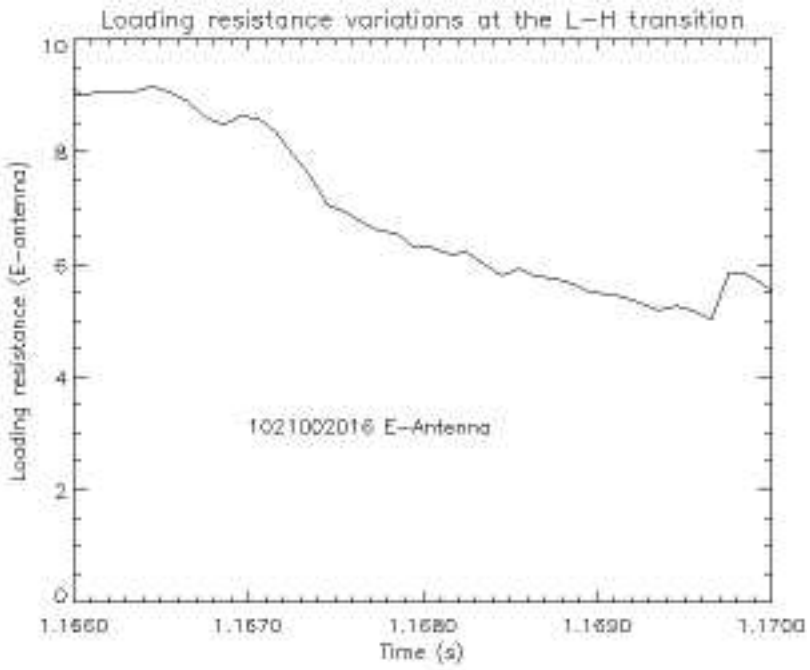

Figure 2-1: Typical time evolution of the loading resistance on Alcator C-Mod during a L to H transition.

or slowly during long discharges. Therefore the rapid and signifi cant changes make it impossible for the network to operate with low VSWR at all times. Two directions might be investigated for possible improvements :

- **Fast matching system** The impedance matching system is tunable on very short timescales - ideally as fast as 10^{-4} s.

- **Robustness** The prematching or matching network is effectively reducing the loading impedance variations so that the mismatch at its feed point remains acceptable, at least for typical load characteristics. Such systems might also be called *tolerant/resilient to load variations*.

It is also worth noting that both systems correspond to **automatic matching systems**, which means that, potentially, the system does not requires the presence of a human operator. This reduces the required manpower to operate the system.

Table 2.1: ICRF antenna parameters

Tokamak	Coupled Power (MW)	Power density (MW/m^2)	Max voltage (kV peak)	Frequency range (MHz)
JET (A2)	8-14	2.5	35	25-55
JT-60 U	7	6	35	102-131
Asdex Upgrade	4-6	2.4	26	30-60
Tore Supra	9.5	12-15	45-50	35-80
DIII-D	3.6	3	25	30-60
C-Mod (D,E)	3.5	10	45	80
TEXTOR	3.6	6-10	36	26-38

2.2.2 Possible options for fast-matching/robustness

Since the mid 80's and early 90's, several potential fast-matching or resilient systems have been investigated. The most relevant [12] will be described here, as an account for possible options in Alcator C-mod. Most of these systems implement a reactive component with fast tuning capabilities in the transmission line network. Achieving the fastest tuning possible while not compromising other desirable constraints (like the power handling capability, heating efficiency and impurity production control) is the technical challenge that each of these designs has to face, with various aspects involved. The reader may refer to table 2.1 for typical parameters achieved while operating these different systems.

Fast capacitors stub tuner system in Textor

Textor implemented in the early 90's a double stub tuner system using variable capacitors. The system [13] actually consists of a row of two double tuner system (Figure 2-2). From the load to the generator, the first is a traditional slow-moving double tuner system for coarse matching. The second uses small variable capacitors to perform fine fast matching. Each capacitor is positioned by a servo-motor driven mechanism.

The system has been tested for high power operations with plasma loading in 1992. Its response time is $\sim$ 40 ms ([13] and figure 2-3) for typical discharges. It has been used routinely since then.

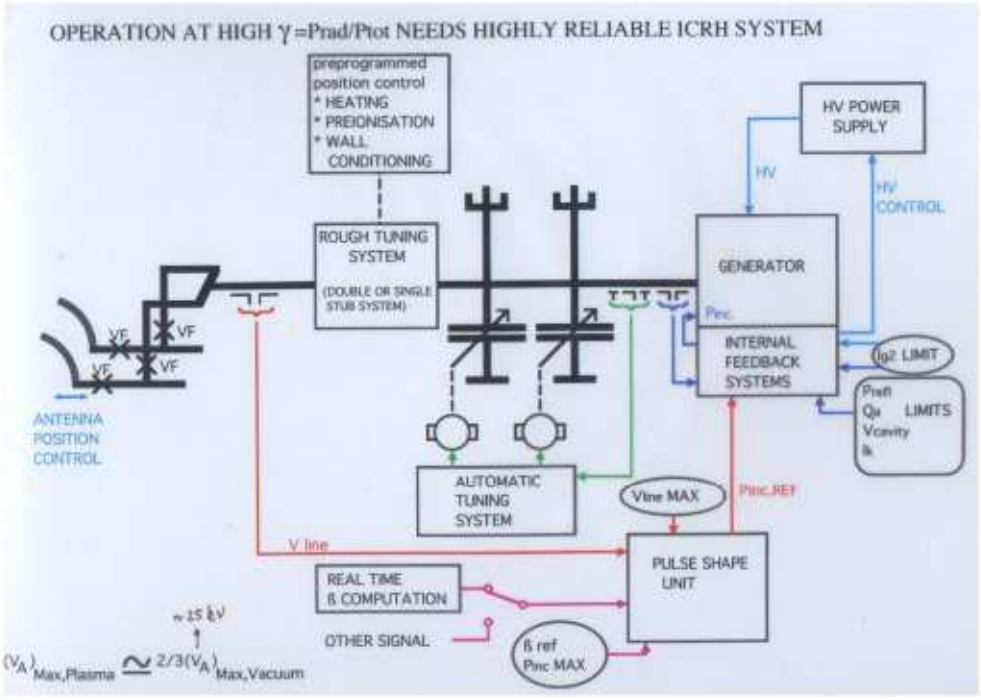

Figure 2-2: Schematic layout of the impedance matching network in Textor.

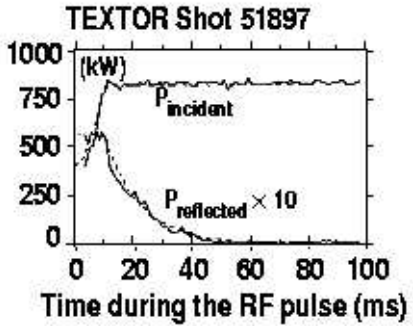

Figure 2-3: Response time of the impedance matching network in Textor.

Resonant double loop antenna in Tore Supra, TFTR and JET

The resonant double loop (RDL) design is a now well tested antenna scheme which was proposed [2] by Owens at Oak Ridge National Laboratory (ORNL). It is presently used on Tore Supra and is part of ITER-FEAT ICRH antenna design. The time constant for fast matching using tunable stub-tuner phase shifter pairs is typically $\sim$ 100 ms, but the system

can in principle exhibit a *load tolerant* behavior which makes it robust, as will be shown in chapter 4. Furthermore, the matching is realized in the antenna structure itself and therefore the feedthrough and transmission line network are not exposed to high VSWR (The tore Supra system keep VSWR below ~ 1.2 in plasma conditions).

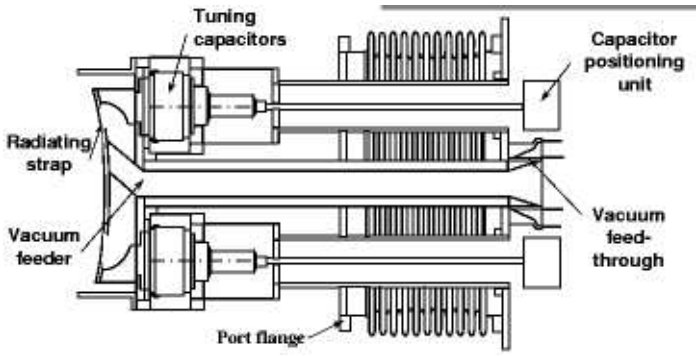

Figure 2-4: Resonant double loop confi guration in Tore Supra.

A drawing for the presently used tuning capacitors (built by Comet Technick - Switzerland) is presented in fi gure 2-5. About 40 units have been used since the beginning of the operations (10 years ago). The capacitors are indeed submitted to high electrical, thermal and mechanical loading. The dielectric material used will also exposed to high neutron radiation in a burning plasma experiment and therefore the device seems impractical in reactors conditions.

ITER Design Team is [14] currently working on variants of the presently used RDL structures to replace the lumped tuning components with sections of transmission lines. A prototype ITER-like load tolerant antenna is being designed for JET.

Fast ferrite tuner - Advanced Ferrite Technology

By changing the magnetization of a ferrite material, the electrical length of a transmission line component can be changed within one to several milliseconds. A matching system using fast ferrite tuners (FFT) has been developed by Advanced Ferrite Technology (AFT) and successfully tested under plasma conditions in ASDEX upgrade, with a response time of about 4 ms.

A ferrite tuner relies on the change of the magnetic permeability μ in ferrites with an

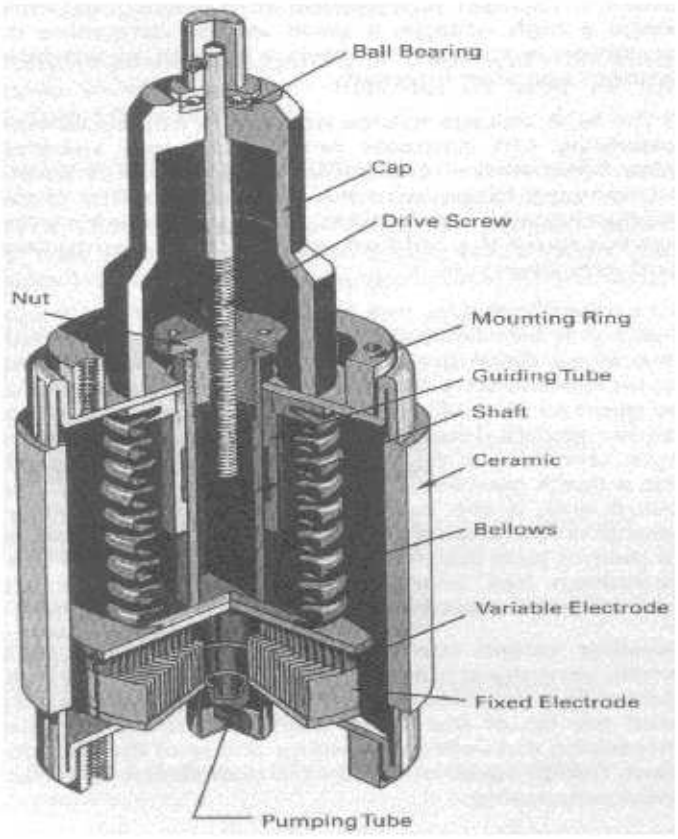

Figure 2-5: Variable capacitor used in Tore Supra RDL.

external magnetic field. When a piece of transmission line is partially filled with ferrimagnetic materials, varying μ allows to change the electrical characteristics of the line, either through the phase velocity $v_p = \frac{1}{\sqrt{\mu\varepsilon}}$ or through the boundary conditions. A combination of permanent magnets and magnetic fields coils produces the tuning external field and therefore the electrical length of the line can be adjusted dynamically through the current in the coils. The response time of the device, including the data acquisition and control system, is expected to be very low (one to several milliseconds).

A fast ferrite stub tuner (Figure 2-6) has been developed by the German company Advanced Ferrite Technnologies (AFT) in the early 90's. A double stub tuner system using such devices has been tested under plasma conditions in DIII-D [15] and ASDEX Upgrade [16] and is to be implemented on ASDEX Upgrade [17]. Under plasma conditions, an achievable matching speed is $\leq$ 500 ms according to these tests. A maximum voltage of

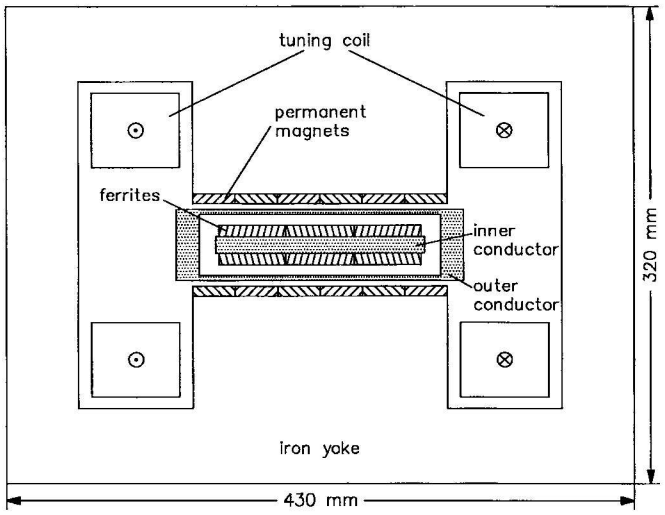

Figure 2-6: Cross section schematic of the fast ferrite tuner designed by AFT

70 KV with 3 bar SF_6 was targeted in the specifi cations of the initial design.

Liquid stub tuner - LHD

A liquid stub tuner has been developed and implemented on the Large Helical Device (LHD) [18]. It uses the difference of RF wavelengths between a gas medium and a liquid. By changing the level of the liquid, the electrical length of the device can be varied from 0.26 to 0.45 wavelengths at 36 MHz. An RF power of 1 MW has been transferred to the plasma by a double stub tuner system using such components. The tuners can withstand 63 kV for 10s and 50 kV for 30 minutes. The system has a response time of 7 s, and therefore cannot be considered as a fast-matching option for C-mod.

Traveling wave antenna on DIII-D, JFT-2M

The traveling wave antenna structure [19] is designed to maintain good impedance matching without dynamic tuning during abrupt changes in the antenna loading. Through external components in the transmission line network, the mutual inductance of the antenna straps is increased so that the changes in the strap impedance due to the plasma loading evolution are reduced. If the number of straps is suffi cient and the array form a set of resonators, all the power is radiated before the traveling wave reaches the end of the structure. The system

has a small bandwidth.

The system was implemented and tested on DIII-D [20]. Between 79 and 81 MHz, the reflected power is reduced to 1% to 4 %, showing attractive robustness without any special fast tuning component. A recirculator circuit is used to reinput the uncoupled power to the TWA structure.

Fast frequency feedback techniques

Another possibility for fast matching relies on fast variations of the generator frequency (typically half a MHz in a few hundred microseconds) . If the length of the transmission lines in the ICRF network are long enough, varying the frequency changes the effective electrical length of the different sections. This technique effectively introduces a fast phase shifter in the system, with a very fast response time.

The JET C and D antennas [21] have been equipped with a system using this technique. The frequency control allows variations as fast as 300 kHZ in 300 μs. A high characteristic impedance section is used to lower the voltage in the 70 m long transmission line acting as a phase shifter. Finally, an adjustable stub tuner realizes the final impedance matching before the generator. This system is particularly suited to keep the voltage standing wave ratio low during ELM activity.

Before studying the feasibility and attractiveness of these techniques for the Alcator C-Mod ICRF system, we will describe the Alcator C-Mod tokamak and its present ICRF systems in the next section.

Chapter 3

Present ICRH system in C-Mod

3.1 The Alcator C-Mod tokamak

3.1.1 Presentation

Alcator C-Mod is the third tokamak of the Alcator series. It started operating at the Massachusetts Institute of Technology in May 1993. It is a compact, high density (up to $10^{21}m^{-3}$), high fi eld (up to 8 Tesla) and high power density device, thus exploring a unique regime in the world fusion program. Typical parameters for Alcator C-Mod discharges are listed in table 3.1. A drawing of the tokamak is shown on fi gure 3-1.

The vacuum chamber is made of stainless steel and covered with molybdenum tiles. Ten horizontal ports and ten vertical (top and bottom) ports provide access to the plasma

Table 3.1: Typical parameters of the Alcator C-Mod tokamak

Major radius	0.67 m
Minor radius	0.22 m
Toroidal fi eld	max 8 T
Elongation	1.6
Triangularity	.5
Plasma current	max 2 MA
Average density	max $10^{21}m^{-3}$
Central electron temperature	up to 5 keV

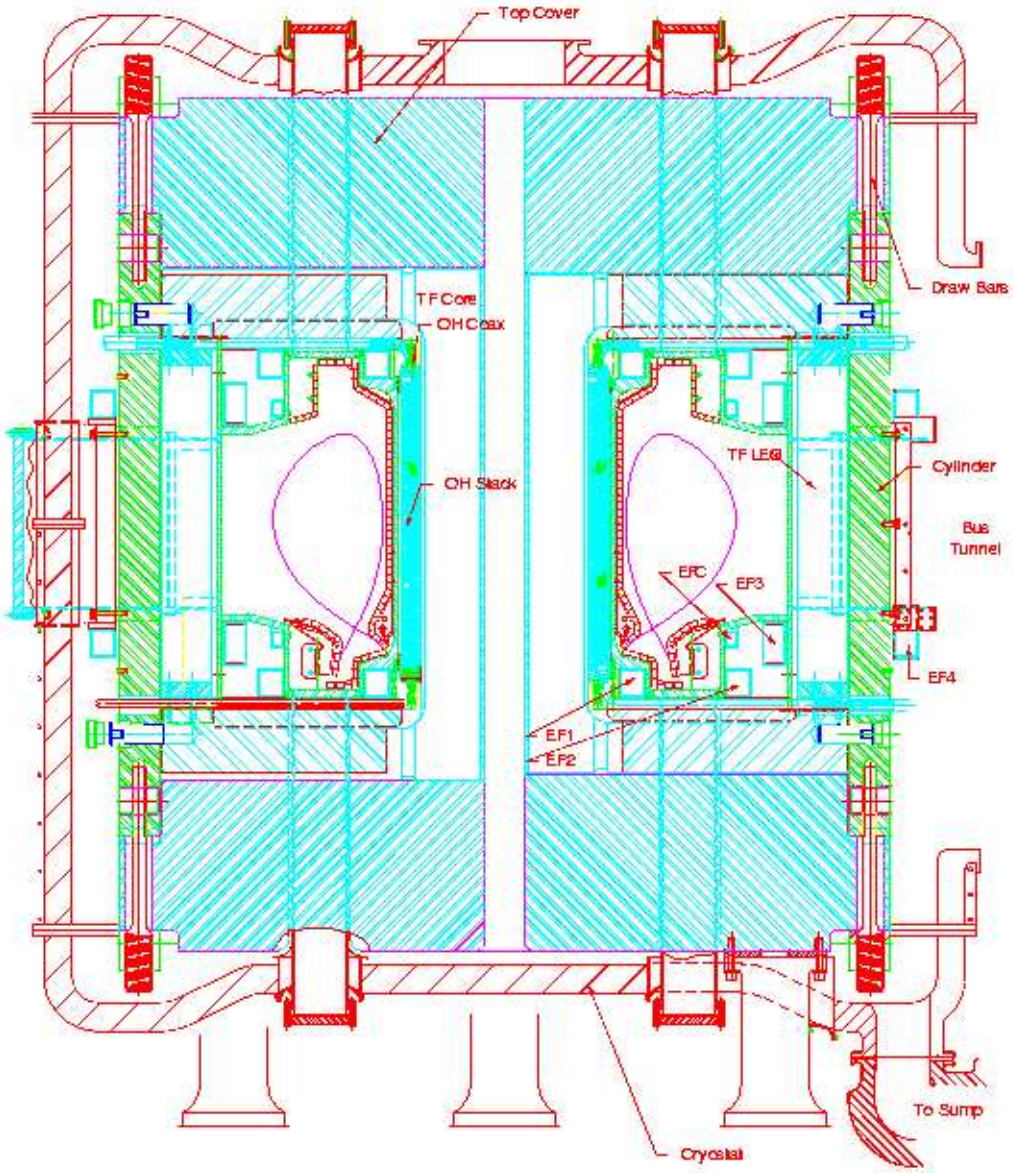

Figure 3-1: Cross section of the Alcator C-Mod tokamak. This drawing does not take into account the modifi cation of the divertor geometry in 2001.

for diagnostics or auxiliary heating. In addition to the 8 T toroidal field created by the toroidal coils, the plasma shape can be controlled by 4 sets of poloidal coils and its current generated by 3 sets of coils in the central column. All coils are cooled by liquid nitrogen. Both limited and diverted shapes (upper or lower single null and double null) are available. The discharge length is about 2 seconds, during which the required 500 MJ are delivered by an alternator, and about 10 to 20 minutes are needed between discharges both to cool down and to bring the alternator up to speed using electrical power from the grid. Extensive data on different plasma parameters is collected for each discharge by a set of diagnostics devices and made available through the MDS-plus system.

ICRH is the only auxilary heating system in C-Mod, and it is used extensively during experimental campaigns. Currently, three ICRF antennas are installed on the machine, in the D, E and J horizontal ports (figure 3-2). The center-grounded end-fed two-straps antennas at D (figure 3-3) and E port are structurally identical and they operate with fixed dipole phasing at 80.5 and 80 MHz respectively. They have been used since the beginning of the C-Mod tokamak operations in 1994. The antenna at J-port (figure 3-3) is a compact four strap antenna designed and installed in 1998 in collaboration with the Princeton Plasma Physics Laboratory ; its operating frequency can be adjusted between 40 and 80 MHz by using an appropriate setup for the transmitters and the transmission line network. Different phasings can be used for J antenna, like (0,π,0,π), (0,0,0,0), (0,π,π,0), (0,$\pi/2$,π,$3\pi/2$), and can be used for heating or current drive. Details on the antenna structure and geometry can be found in [22].

Investigation and understanding ICRF heating and current drive is one of the primary objectives of the Alcator C-Mod program ; this includes gaining experience and knowledge in the design and operation of reliable and efficient RF launchers and transmission systems. This present work is part of this effort. Among the other proposed upgrades to the RF system in Alcator, we can mention the design and implementation of a new four strap antenna at E-port, which will replace the existing D and E antennas.

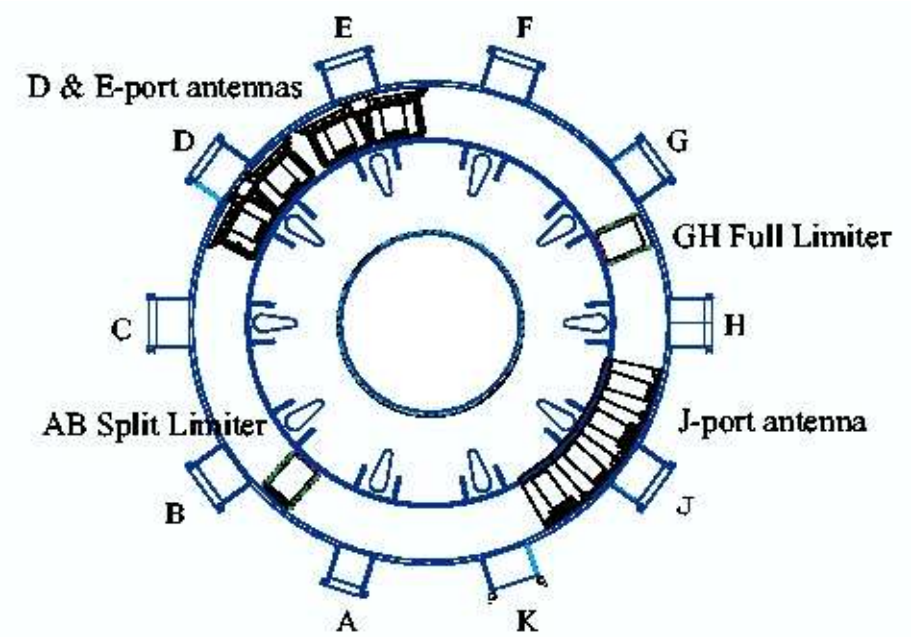

Figure 3-2: Top view of the Alcator C-Mod vessel.

3.1.2 Present ICRF system

Transmission of the ICRF power from the source to the antenna uses a network of low loss coaxial transmission lines (figure 3-5. Copper is used for the inner conductor while the outer is either copper or aluminum. Close to the antenna structure, high pressure sulfur hexafluoride SF_6 gas is injected after pumping and maintained around 3 bar, which substantially increases the breakdown limits in the corresponding sections. Teflon spacers are used all along the network to hold the central conductor in place. From the transmitter to the antenna feedthrough, the outer to inner diameter ratio in the coaxial lines is set with various combinations so that the impedance of the lines is 50 Ω, which corresponds to a good trade-off between power-carrying limits and breakdown limits (fig. 3-6).

The behavior of the network is monitored by a set of directional couplers (DCs), with typically -60 to -70 dB attenuation for the measured direction and -90 dB for the reverse direction. Pairs of such couplers located at the same location give forward and reflected power measurements. The phase is obtained through demodulators boards, and the three channels are digitized to the acquisition system. In addition to directional couplers, voltages probes and some current probes are also present at specific locations. Typically, measurements

Figure 3-3: Picture of D-Antenna as installed in the vacuum vessel.

Figure 3-4: Picture of J-Antenna as installed in the vacuum vessel.

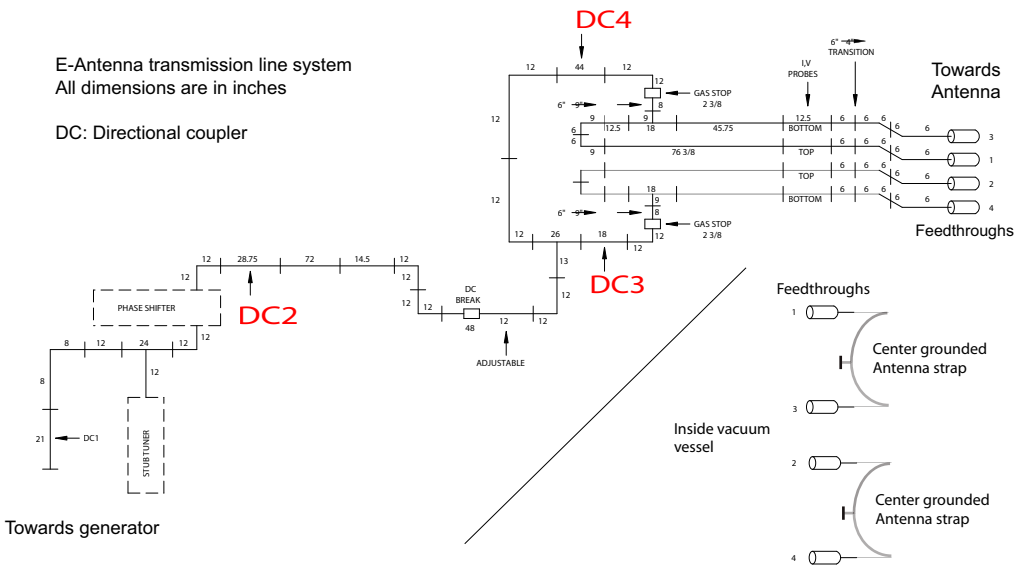

Figure 3-5: Schematic diagram of the transmission line network for E-Antenna.

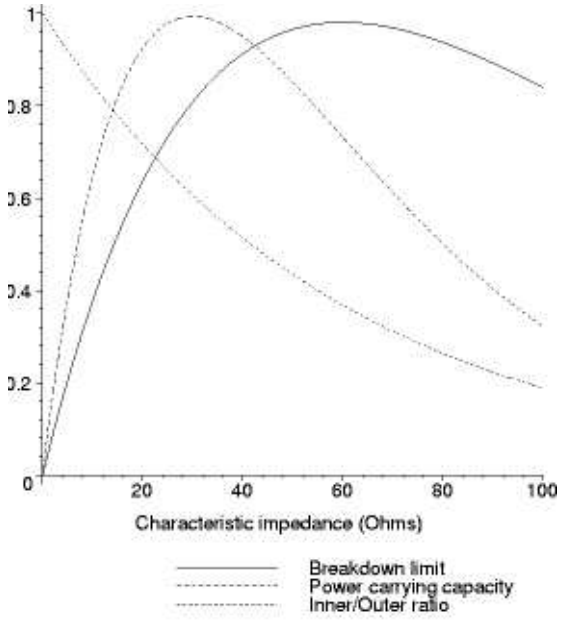

Figure 3-6: Power and voltage limits in a coaxial line as a function of its impedance.

are done close to the high voltages points, as permitted by possible physical layouts of the sections.

The impedance matching uses a stub tuner/phase shifter pair, which is adjustable between discharges. The phase-shifter/stub tuner matching network will be presented in chap-

ter 5.

Different arc detection systems were initially available on the C-Mod ICRF network [23]. They rely on logarithmic demodulator modules with different voltage/current probe or directional coupler positions. High VSWR, high reflected wave power or phase differences induced by arcing can be tracked by the modules, and the excitation from the transmitter can be removed within 10 μs. Although phase difference faults are present in the system, usually arcs manifest themselves through the increased VSWR in the matched part of the network. This method is robust and reliable, although in principle high current point arcs remain undetected in principle. Inspection of lines suggest that most breakdown occurrences take place near high voltages points or at insulating surfaces, and therefore the present system is effective in limiting their effect.

3.1.3 Typical loading variations for D and E antennas

Currently, the antenna loading resistance is low compared to the characteristic impedance in the transmission lines and corresponds to reflection coefficient around 0.8 in the unmatched part of the network, with some variations both in magnitude and phase during the discharges. By tuning the phase shifter-stub tuner for *average* conditions within this range, this mismatch can be reduced in the transmitter side of the network, allowing acceptable high power operations ; the typical reflected power on the transmitter side is less than 5 % in most conditions. However, the unmatched part is still subject to high VSWR and strong circulating power, and residual loading variations with plasma conditions lead to a still significant loss of power from the unmatched reflected power, namely up to 5-10 %. The variations of the coupling with the plasma parameters have been studied in 2001 and 2002 for the three antennas in C-Mod.

Typical Smith Chart loadings at DC2 are shown on fig 3-8 and 3-9 for D and E antennas. The variations of the loading impedance of the antenna are restricted to a small area of the Smith Chart. The loading impedance at DC2 varies from 5 to 10 Ω for both D and E.

Loading variations during operations can be related to variations of the density profiles at the edge of the plasma [24]. In most conditions, the fast-wave cutoff surface is in the

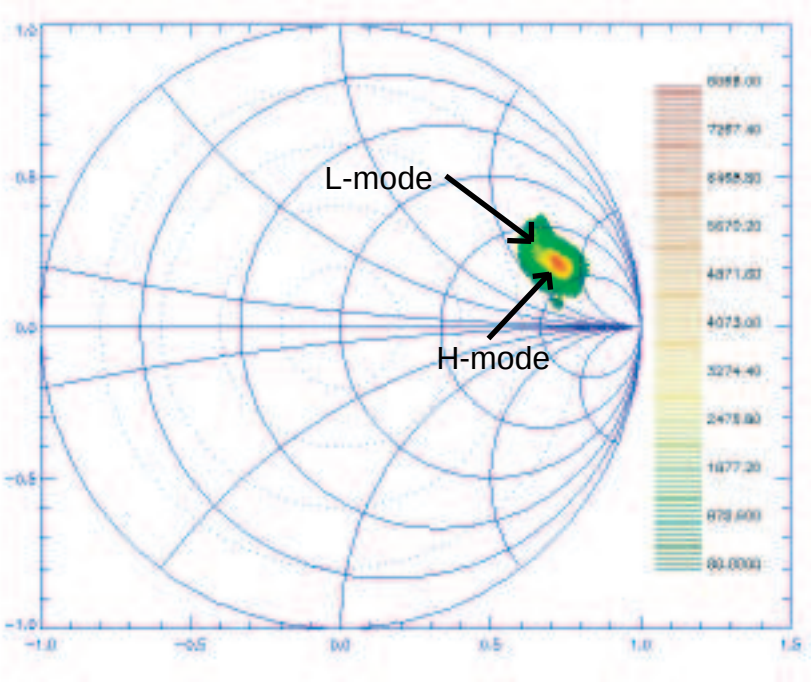

Figure 3-7: Loading at DC2 for E-Antenna during the second half of the 2003 campaign. The colors correspond to the aggregated time.

limiter shadow and the short evanescent layer distance results in relatively high coupling compared to other large-size tokamaks. Edge activity and changes confinement modes affect the antenna coupling on short timescales and therefore result in rapid changes of the antenna loading.

On Alcator C-Mod, small irregular ELMs (grassy ELMs) can be encountered in some conditions, but they do not result in significant variations of the antenna loading impedance. The most important source of loading variations for C-Mod is the L-H transition, which typically occurs on timescales as short as 10^{-4} s. The loading resistance can drop by a factor of 2 during the L to H transition. Some variations can be also seen in the reactive part of the loading impedance during this transition, as can be seen on the Smith Charts (phase changes), although the effect is relatively small.

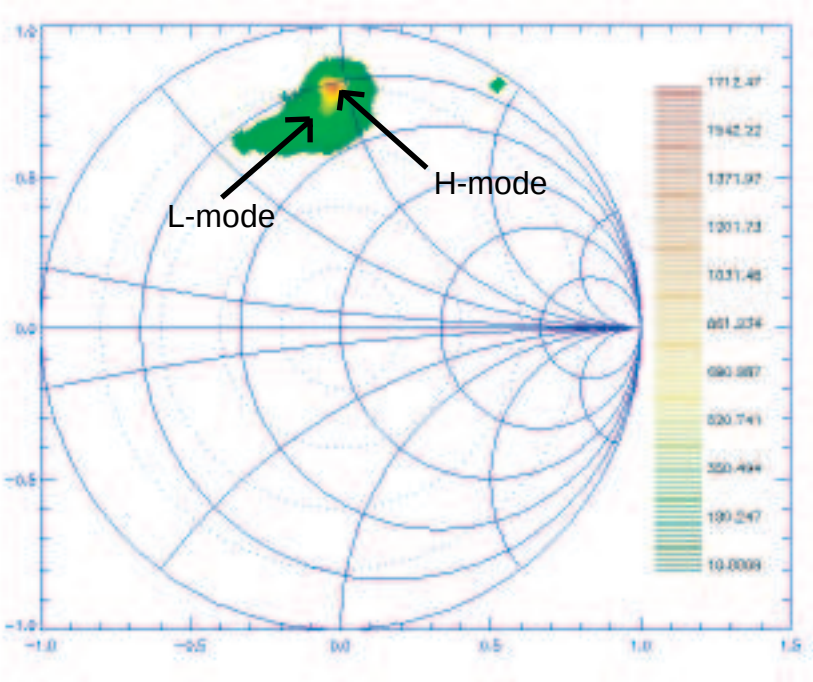

Figure 3-8: Loading at DC2 for D-Antenna during the 2002 campaign.

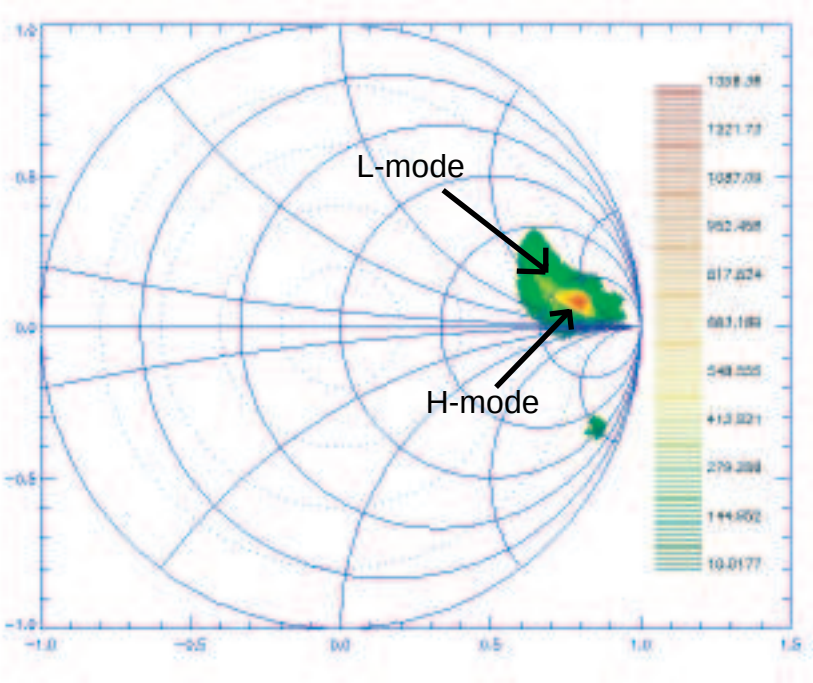

Figure 3-9: Loading at DC2 for E-Antenna during the 2002 campaign. The colors correspond to the aggregated time.

3.2 Fast-matching systems for Alcator C-Mod

In the last chapter, several existing and proposed techniques for fast-matching and load tolerant operation were briefly mentioned. Some of these systems are either unfit for Alcator C-Mod, or their implementation would not bring a significant improvement over the present situation. Only the ferrite-tuner based system and the load tolerant technique seem both feasible and likely to improve the matching situation on C-Mod.

Therefore, from the general objective outlined in chapter 1, the focus of this work can be split in two separate directions :

1] Investigate the design and implementation of a load tolerant configuration on D and E antennas, inspired from the RDL designs in TFTR, Tore Supra and JET.

2] Design a tuner whose electrical length can be varied on timescales as fast as a few hundred microseconds to a few milliseconds. The ferrite-loaded transmission line section is presently the only acceptable baseline for this tuning speed requirement.

We will study 1] in the next chapter, while chapters 5, 6 and 7 will be devoted to 2]. A summary of the findings, conclusions and a presentation of open questions and future work can be found in chapter 8.

Chapter 4

Load Tolerant Configuration

Effective impedance matching systems are usually composed of structurally complex tuners. Therefore, they usually have lower breakdown thresholds than coaxial lines and present higher risk of arcing. While protecting them and detecting arcs in their structure is critical, it is also desirable to lower the VSWR at their input. The maximum power can be thus determined by voltage limits at other regions of the network, and it is usually higher. This technique is called *prematching*, and can be performed effectively by including additional fixed components.

For example, a fixed impedance matching network can be used between the fast matching system and the antenna, as on Textor. Alternatively, sections of transmission lines with higher or lower characteristic impedance can be used as quarter wavelength transformers. These two solutions are simple and reliable, with little limitations. However, they leave the loading variations unchanged in magnitude. Another approach is the resonant double loop (RDL) configuration, which has been first investigated at Oak Ridge National Laboratory and has been installed on Tore Supra, JET and TFTR, as presented in chapter 2. It was realized in the late 90's that this system could have *load tolerant* capabilities. This possibility has attracted much attention from the community since then. However, while the present ITER design targets load tolerant operations using a RDL design, there has been no experimental test so far.

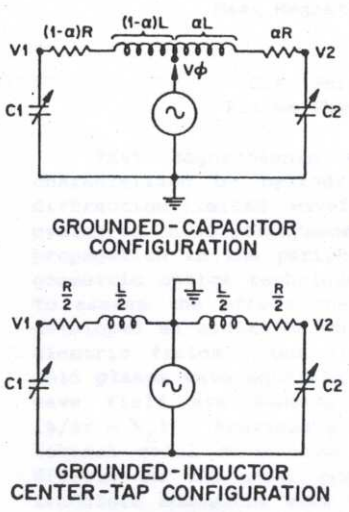

Figure 4-1: Resonant double loop antenna schematics (from [2])

4.1 RDL prematching network and robustness

4.1.1 Resonant Double Loop antenna network

The resonant double loop configuration was first introduced [2] by T.L. Owens at ORNL, as a possible way to achieve prematching in the antenna structure itself. The VSWR could be lowered in the antenna feedthrough, which is traditionally a likely location for electrical breakdown. Although the original work only included center-tapped antennas 4-1, only small modifications are required to obtain an equivalent design for center-grounded straps with similar characteristics.

For a given loading impedance in the straps, the values of the capacitors or inductors can be adjusted to obtain a certain impedance at the feed point. By setting this output impedance equal to the characteristic impedance of the transmission line, the antenna can therefore be matched at this point, assuming that the feedthrough introduces little mismatch. The analytic study leads to a quadratic equation for the capacitances (resp. inductances) of the capacitor pair (resp. inductor pair) and therefore there are in general two different configurations for a given loading impedance.

This also means that for a given configuration, there are two values of the antenna loading impedance which can lead to matched conditions at the tap point. If $Z = R + jX$

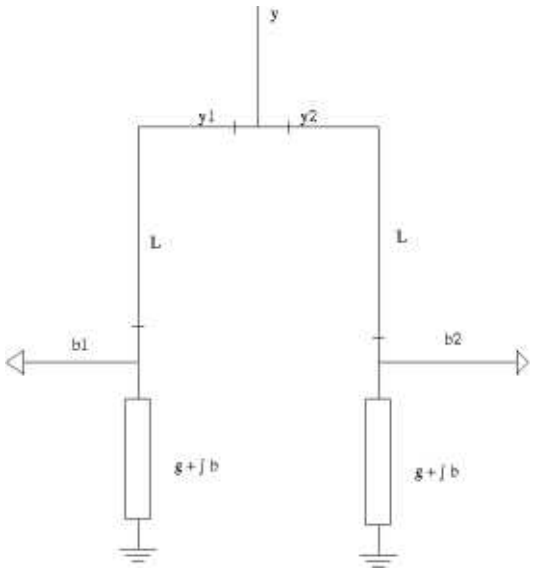

Figure 4-2: Conjugate tee network.

is the impedance of the straps, and $\rho(Z)$ is the reflection coeffi cient as seen from the feed point, ρ is a positive continuous function with two roots and therefore it has an extremum point Z_{ltol} in the complex plane. The loading variations around Z_{ltol} can be then effectively reduced by the system, and the network would be load tolerant. We will develop on this approach in the next section, with a C-Mod relevant confi guration.

4.1.2 Conjugate tee network

As D and E antennas in Alcator C-Mod are center-grounded, the resonant double loop confi guration can be obtained without using tunable capacitors, by inserting shunt stubs in the loop, leading to the schematics on fi gure 4-2. We assume here that the load impedance at the antenna ports is the same for the two ports in all operating conditions and we will work with normalized impedances, i.e. take the characteristic impedance of the transmission line $Z_0 = 1$. For $L = \frac{\lambda}{4}$ at the operating frequency, the transformation from the admittance $y = g + jb$ at the antenna port to the admittance y at the feed point of the loop can be determined through the following steps.

The admittance at the stub end of the L section is :

$$y_1 = g + j(b + b_1)$$

$$y_2 = g + j(b + b_2)$$

The L section transforms y_1 and y_2 according to a phase shifter transformation. For simplicity here, we consider $L = \frac{\lambda}{4}$, so that the admittance is transformed into its inverse [25]. The final admittance at the feed point is the sum of the admittances from the two legs y_{l1} and y_{l2} :

$$y = y_{l1} + y_{l2} = \frac{1}{g + j(b + b_1)} + \frac{1}{g + j(b + b_2)}$$

Equivalently,

$$y = g(\frac{1}{g^2 + (b + b_1)^2} + \frac{1}{g^2 + (b + b_2)^2}) - j(\frac{b + b_1}{g^2 + (b + b_1)^2} + \frac{b + b_2}{g^2 + (b + b_2)^2})$$

For simplicity, we can assume that the typical loading at the antenna port is $g_0 \in [0, +\infty]$, purely real, and study the effect of small variations $g = g_0 + \Delta g$ around this point. From the equation above, we see that we can obtain a purely real impedance at the feed point by choosing $b_1 = -b_2$, which we will assume for simplicity in the reminder of this section.

Resistive variations Variations in the resistive part of the loading impedance ($b = 0$) lead then to :

$$y = \frac{2g_0 + 2\Delta g}{(g_0 + \Delta g)^2 + b_1^2}$$

The condition for obtaining a match at the feed point is a second-order equation :

$$(g_0 + \Delta g)^2 - 2(g_0 + \Delta g) + b_1^2 = 0$$

Two solutions are found if $b_1 < 1$:

$$\Delta g = 1 - g_0 - \sqrt{1 - b_1^2}$$

$$\Delta g = 1 - g_0 + \sqrt{1 - b_1^2}$$

The resulting VSWR is kept low in the region between the two matched points, as seen on figure 4-3 for a typical case. The maximum in the region for y is always found for $\Delta g + g_0 = b_1$ and the parameter b_1 also determines the size of the region between the two matched points and the resulting maximum of the VSWR in this region. There is a trade-off for the maximum VSWR and the extent of the region between the matched points. The initial loading g_0 can not be matched ($\Delta = 0$ for one solution) if $g_0 > 2$.

In this configuration, therefore, the initial loading at the conjugate stubs must be closed to matched conditions, with low initial reflection coefficient. In chapter 2 and 3, we have seen that this is not the case for ICRF antennas, and therefore either the initial loading at the antenna port must be prematched to lower the reflection coefficient, or the characteristic impedance of the transmission lines must be made very low, with potential side effects on the breakdown limits. The conjugate tee network is not strictly speaking a prematching network, but required components for prematching are easily added to the configuration as we will see below.

Inductive variations The analysis above corresponds to the standard approach in studying potential load tolerant configurations. The network seems highly effective at keeping the VSWR low for a wide range of loading conditions ; however, a major complication occurs as soon as inductive variations in the loading impedance are involved, namely the input current will split at the feed point in an unbalanced way.

The current ratio between the two branches can be evaluated through the ratio of the conductances of the two legs at the tee :

$$\frac{|I_2|}{|I_1|} = \sqrt{\frac{Re(y_2)}{Re(y_1)}}$$

With the formula above, in the $L = \frac{\lambda}{4}$ case, we obtain :

$$\frac{|I_2|}{|I_1|} = \sqrt{\frac{g^2 + (b + b_1)^2}{g^2 + (b + b_2)^2}}$$

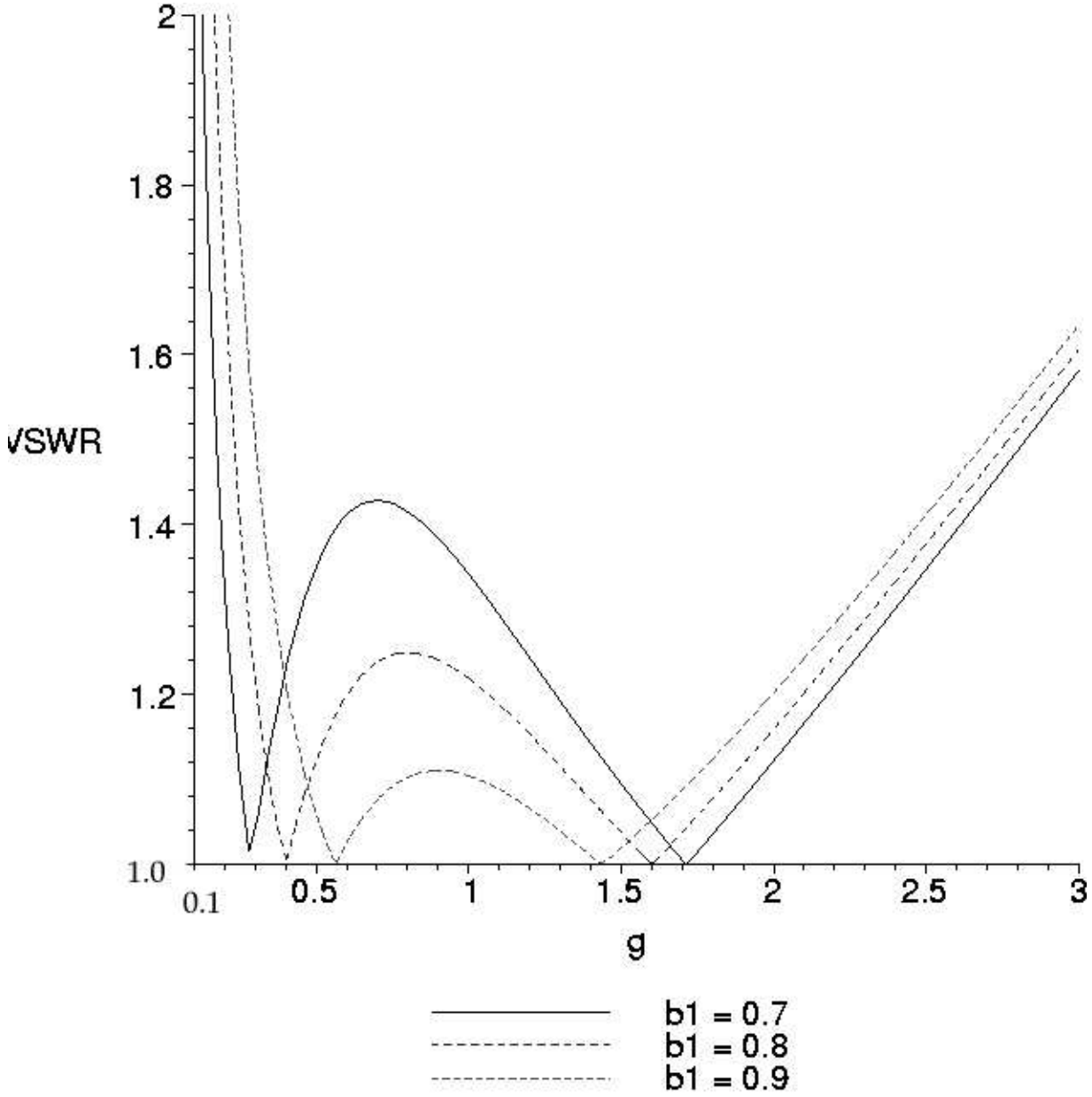

Figure 4-3: Calculated VSWR at the feed point for different values of the normalized stub reactance b_1 and of the loading conductance g.

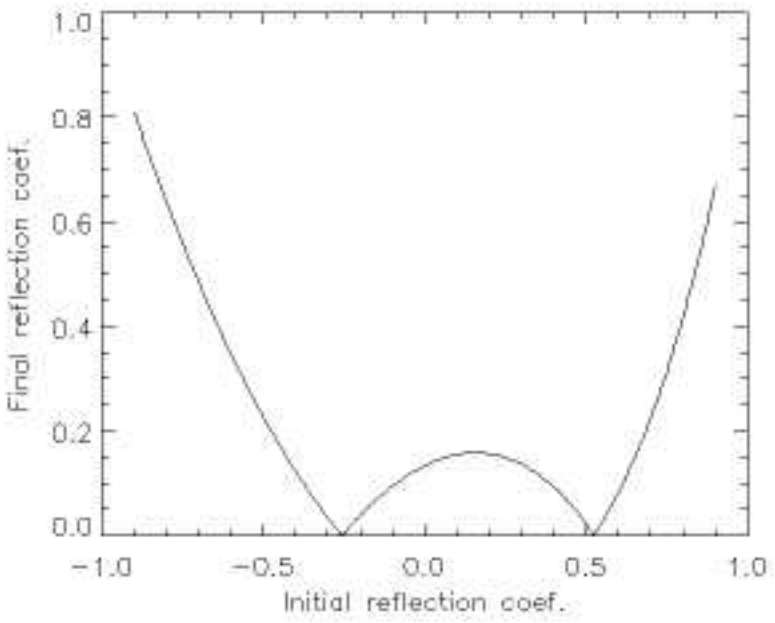

Figure 4-4: Reflection coefficient at the feed point for different values of the reflection coefficient after the antenna straps. The final reflection coefficient is reduced below 0.2 for the range -0.4 to 0.6

If $b_1 = -b_2$, $b = 0$ results in a balanced current splitting between the two legs and therefore the two straps. However, as soon as $b \neq 0$, a significant current imbalance is introduced, with potential side-effects on the current distribution in the antenna straps. We will illustrate this effect with a more general approach using numerical simulations.

General case

The analytic description becomes less intuitive as the loading is not purely dissipative or as the lengths of the different sections are changed. The numerical approach was preferred and a code in IDL was developed to study the different configurations. Ideal transmission line theory was used to model the different sections and components, and we used the Smith Chart representation [25] to present the results.

The simple calculations above can be numerically reproduced, as shown on figure 4-4. The analytic approach above showed that the system behaves appropriately for purely real impedances, but it becomes less intuitive as reactive variations are introduced. This is rendered with the model on the Smith Chart color plot in figure 4-5. The colors show the final

reflection coefficient at the tee for all ranges of antenna port impedances in the Smith chart. We can see in dark green two solutions found for the match at the feed point, and between these two solutions the reflection coefficient is kept low. This is also true for changes in the reactive part of the impedance, which correspond to deviation from the horizontal axis. If the input impedance at the antenna port can be prematched to be centered in the green region, then its variations will have only moderately affect the reflection coefficient in the main line from the feed point to the generator, and the VSWR will be kept low for a wide range of loading conditions. Various prematching techniques can be used to transform the initial impedance at the antenna port into the wide green region at the center of the Smith chart, or equivalently the characteristic impedance of the feed line can be varied to match the initial loading.

The undesirable effect of inductive variations can be evaluated in more detail with this approach. As the two branches are now asymmetric, the two legs of the tee see different conductances and unbalanced current splitting can occur. For the same configuration as above, this effect is represented on figure 4-6. The color represent $|\frac{I_1}{I_2} - 1|$, where I_1 and I_2 are the currents respectively in the top and bottom branches. We see that the network induces strong current asymmetry between the two branches as reactive components of the load are present. The effect becomes severe even for moderate phase changes in the loading impedance.

The unequal current splitting can be a major drawback of this technique, as control is lost on the current distribution in the straps. As introduced on chapter 2, controlling the $k_{||}$ profile from the antenna is of primary importance for efficient and robust antenna operations, and therefore we expect negative side-effects on the antenna behavior, although it is not yet clear how severe they will be in plasmas conditions.

4.2 Prototype Design for Alcator C-Mod

As we have seen above, load tolerant configurations can potentially reduce the negative impact of fast loading variations in ICRF networks. Although this makes them very attractive candidates for future designs, we have also identified potential side-effects on the

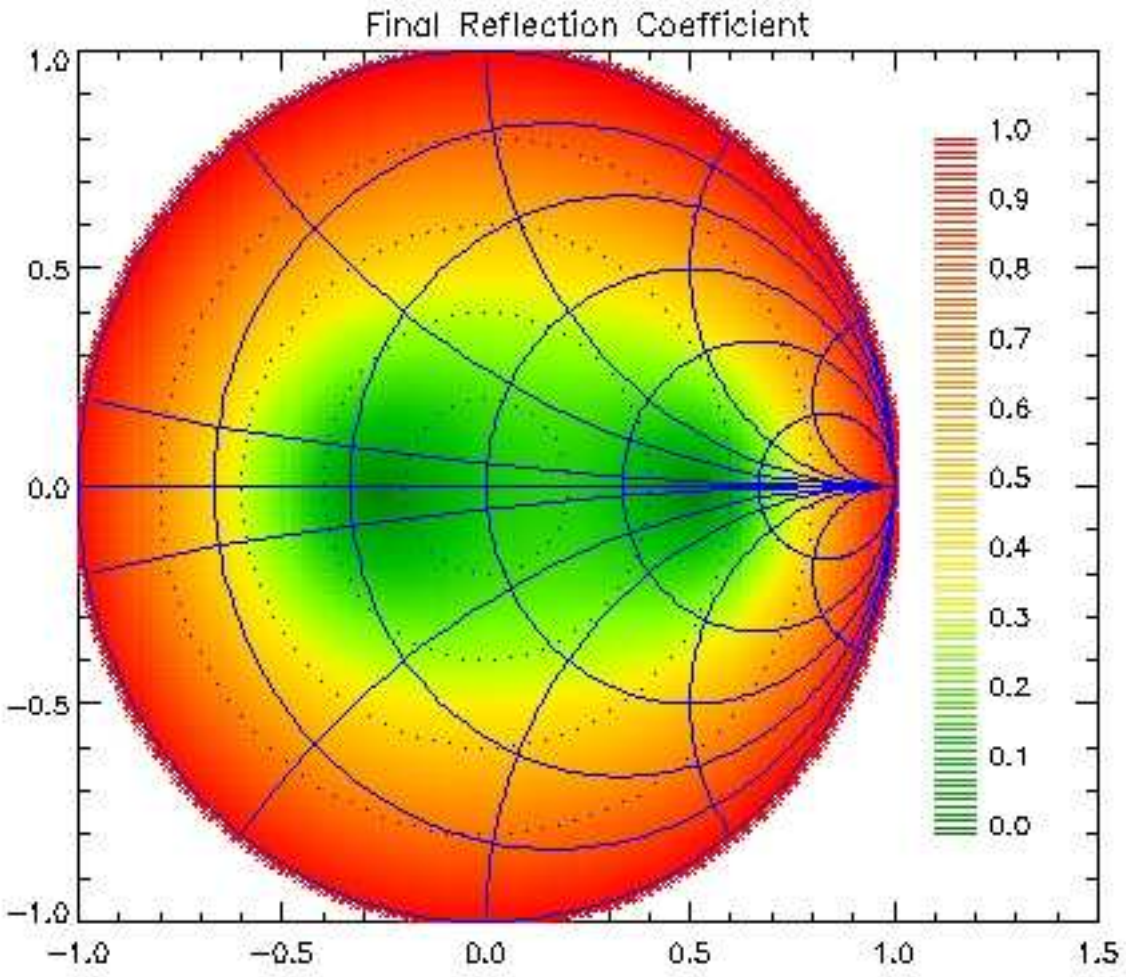

Figure 4-5: Smith Chart plot of the reflection coeffi cient (color) as a function of the load impedance (same parameters as in fi gure 4-4). We see that the conjugate tee system offers some resilience to load variations in a large area of the Smith chart.

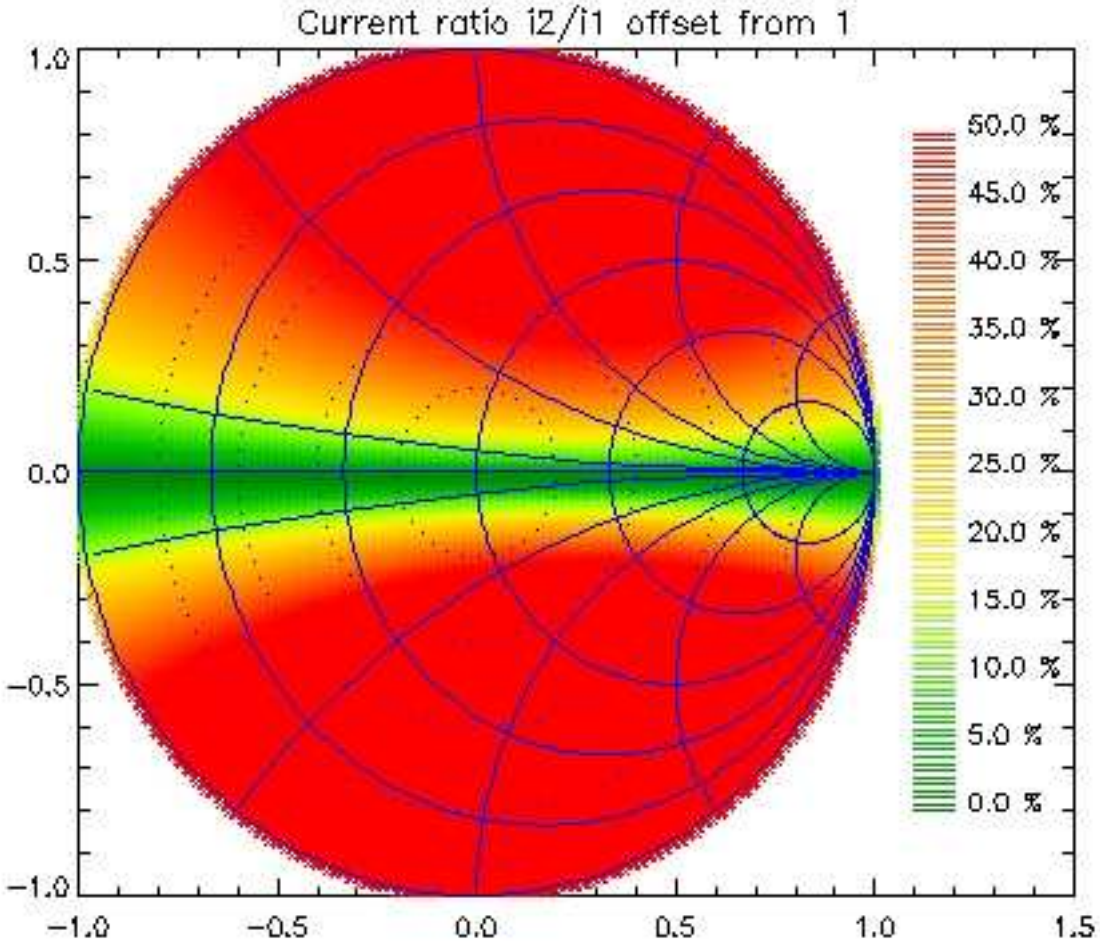

Figure 4-6: Current asymmetry between the two branches. The color represent $|\frac{I_1}{I_2} - 1|$, where I_1 and I_2 are the currents respectively in the top and bottom branches.

overall behavior of the antenna and it is therefore essential to evaluate the performance of a prototype design. This could be done relatively easily on the C-Mod D and E antennas, through simple modifications of the existing network. We will detail the design approach in this section.

4.2.1 Design strategy and method

As mentioned above, the loading impedance at the ICRF antenna ports is usually located in the outside regions of the Smith Chart, as the loading impedance is usually low compared to the characteristic impedance of the network. Therefore prematching systems have to be used between the ports and the stubs in the conjugate tee network. An elegant approach consists in using a fixed phase shifter-stub tuner matching network in order to perform this task : a single stub can indeed act as both as part of this matching network and as part of the conjugate tee network, providing the required reactive component in the line. This leads to the schematic located on figure 4-7.

The design strategy follows :

- **A. Conjugate tee configuration** Obtain a load tolerant configuration using the conjugate tee network as above, and determine the region in the input Smith Chart where low reflection coefficient occur. This gives possible stub lengths $l_{1,loadtol}$ and $l_{2,loadtol}$.

- **B. Prematching** Using a stub tuner-phase shifter matching network, transform the actual loading at the antenna ports to have typical loading in the region above at the prematching stub tuner output. At this point we obtain the two stub lengths $l_{1,prematch}$ and $l_{2,prematch}$.

- **C. Effective stub lengths** By adding the required shunt reactive components for the conjugate tee network stubs and the prematching stubs from the ST-PS pair in each port, determine the length $l_{i,final}$ of a single stub performing these two effects at once. For i = 1,2

$$l_{i,final} = arctan(\frac{1}{\frac{1}{tan(2\pi l_{i,loadtol})} + \frac{1}{tan(2\pi l_{i,prematch})}})$$

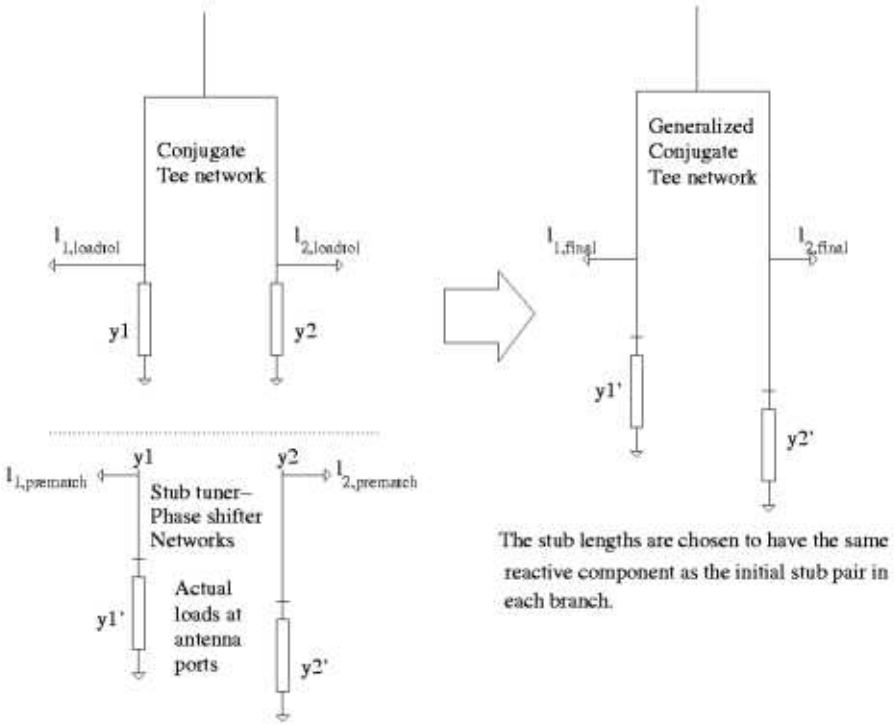

Figure 4-7: Generalized conjugate tee configuration using phase shifter-stub tuner pre-matching pairs.

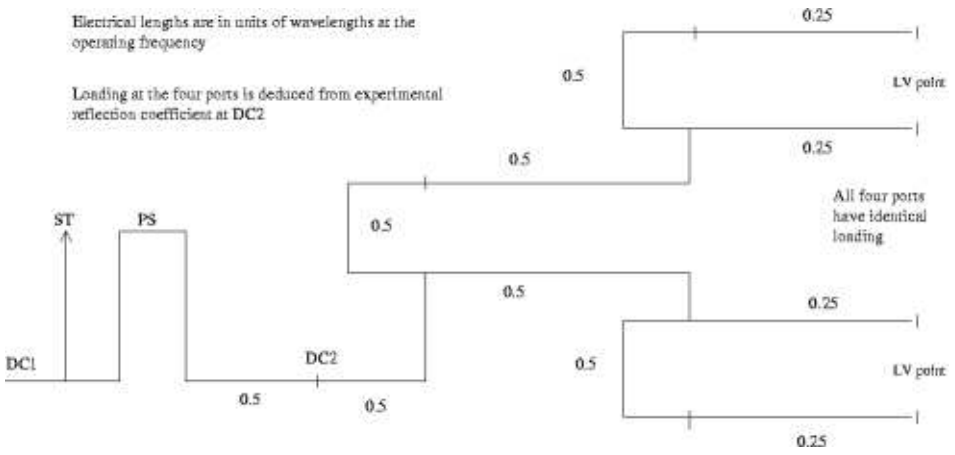

Figure 4-8: Initial network layout for evaluation of the load tolerant configuration. See figure 3-5 for the actual network.

Lengths are in units of wavelengths at the operating frequency.

The procedure leaves some freedom in the chosen lengths of the sections, and for a given loop configuration with fixed stub positions, a load tolerant configuration can also be found only by adjusting the stub lengths in most cases. By adding some constraints, the final impedance at the tee can also be set to a given value, for example 50Ω, by adjusting the stub positions. A traditional impedance matching network can still be used if the final impedance is not 50Ω. Note however that for very high reflection coefficient loadings, the stub reactance required to obtain matched conditions at the conjugate tee is quite high, and small stub length and good precision are required.

A simulated example for load tolerant operations is shown on figures 4-9 and 4-11. The antenna loading as measured at the end of the feedthroughs is computed from the experimental reflection coefficient at DC2. Assuming the four ports have the same loading and if the antenna loading remains unaffected by the presence of the stubs - which is unclear -, ideal transmission line theory allows us to compare the loading variations obtained with a traditional impedance matching system and with or without a load tolerant configuration. The model predicts very low VSWR over the typical loading impedances in C-Mod antennas in this particular configuration, and comparison with the non load-tolerant case shows a substantial improvement. This demonstrates the attractiveness of this network.

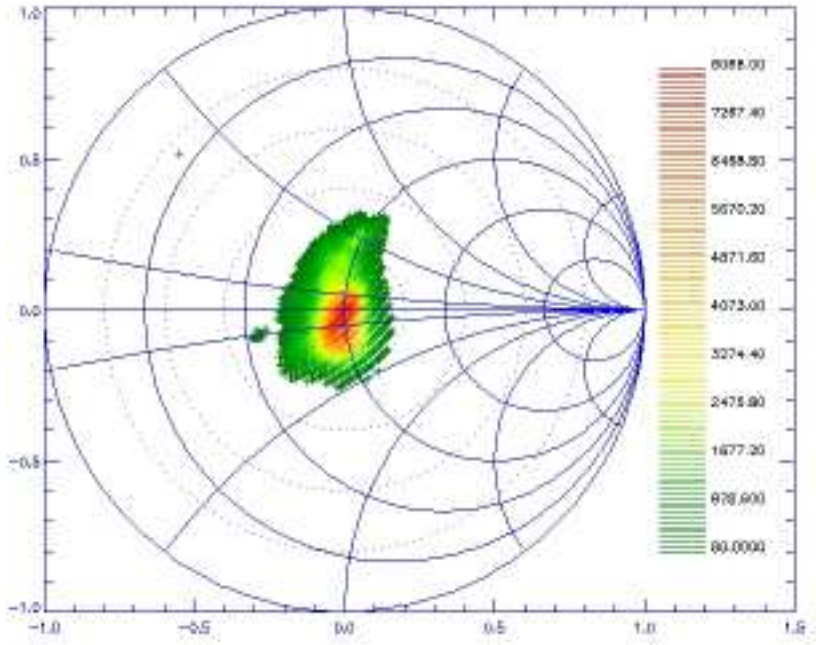

Figure 4-9: Simulated reflection coeffi cient as seen from the transmitter side at DC1 without the load confi guration (fi gure 4-8). The initial antenna loading corresponds to fi gure 3-7.

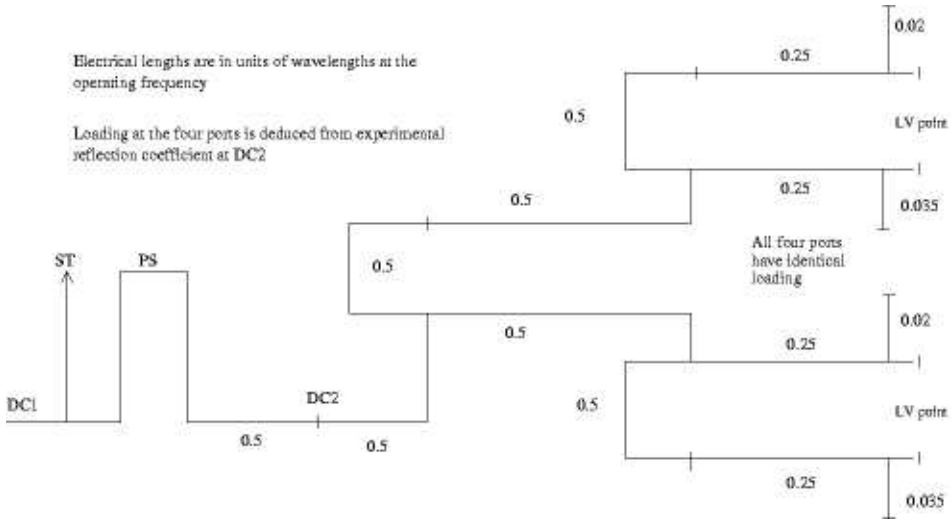

Figure 4-10: Possible confi guration for a load tolerant confi guration using the conjugate tee network, starting from fi gure 4-8

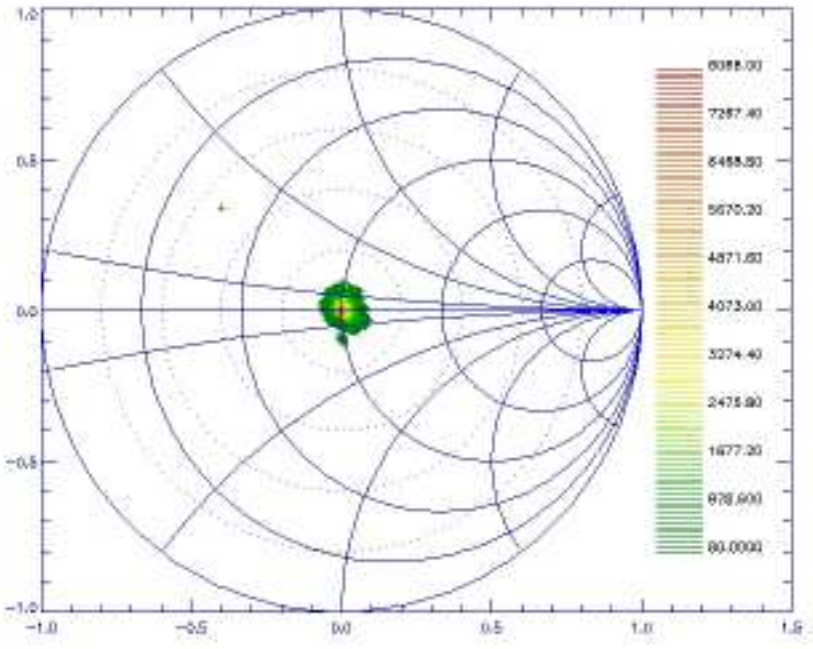

Figure 4-11: Simulated reflection coeffi cient as seen from the transmitter side at DC1 with the load confi guration (fi gure 4-10). The initial antenna loading correponds to fi gure 3-7 and is assumed to be unaffected by the stubs.

4.2.2 Proposed configuration for experimental test

The design of a prototype load tolerant confi guration on the C-Mod D and E antennas stems from the approach highlighted above. Simulations showed that the $\frac{\lambda}{4}$ allows better ability to obtain matched at the feed point. Voltage and current probes were used to determine the loading impedance at the antenna port during the 2002 campaign. Unfortunately only one set of probes were functionning correctly, but the resulting position on the Smith Chart is compatible with measurements of S-parameters in vacuum. The input loading at the probe position is shown on fi gure 4-12 and the deduced confi guration on fi gure 4-13.

Different complications are expected to occur from the formal treatment above. The fi rst one results from the impact of the stub insertion on the loading impedance itself. While it is reasonable to expect that the loading impedance will remain unaffected, it can not be excluded, especially as the current ratio between the branches departs from the balanced situation and changes the poloidal spectrum of the antenna. The second one is the direct coupling between the straps. Measurements in vacuum show that in the non-radiating situ-

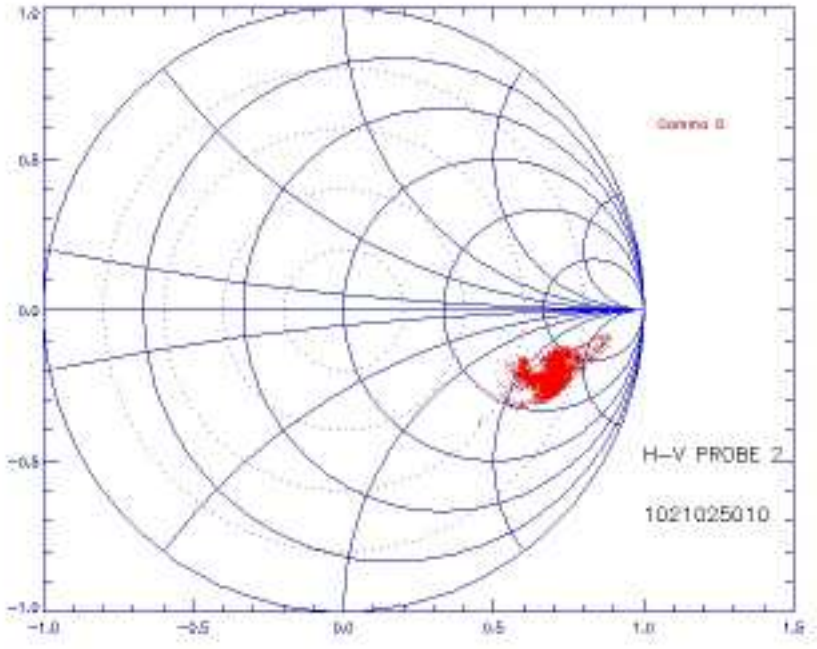

Figure 4-12: Reflection coeffi cient at the current-voltage probes for a typical discharge.

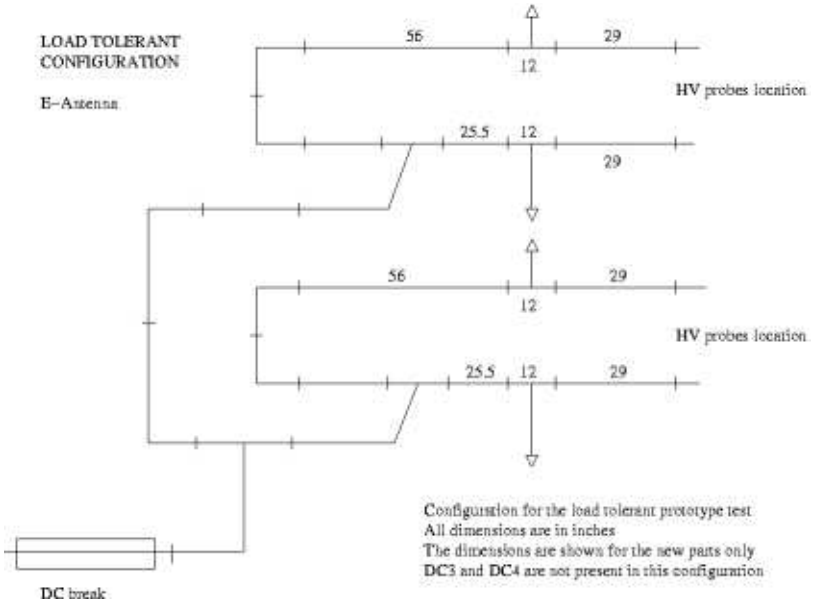

Figure 4-13: Confi guration for a load tolerant network for E-Antenna.

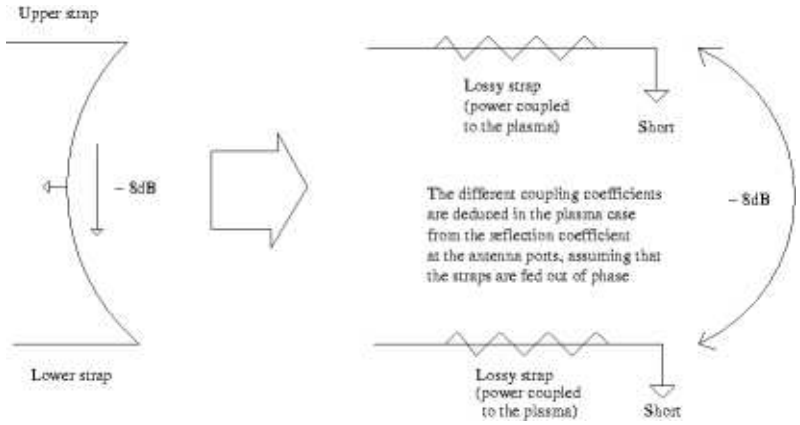

Figure 4-14: Simple model for the coupling in the two legs of each strap.

ation, there is a -8 dB coupling between the two sides of a given strap on D and E antennas and a -20 dB coupling between adjacent straps. While the -20 dB coupling is not expected to be critical, the current imbalance induced by the conjugate tee configuration can potentially change the effective reflection coefficient in the antennas ports through the -8 dB coupling : in the symmetric case, the transmitted port from one strap to the other adds to the reflected power in each port in the same way, but as unbalance is induced, the reflected coefficient is effectively increased on the branches which receive less power and decreased in the branch which receive more. This could induce significant deviations for the main assumption of identical loading impedance for all four antennas port and render the load tolerant cancellation process ineffective. Figure 4-14 illustrates this issue.

These two effects will be monitored during the experimental evaluation, as to date no simulation approach can accurately predict the self-consistent loading of the antenna. With some assumptions, however, we can obtain an order of magnitude for the severity of these processes. For the typical input loading above, fig 4-15 shows the expected loading at DC2. The colors highlight the current imbalance resulting from the loading variations. Figure 4-16 attempts to calculate the self-consistent effect of the -8dB coupling on the reflection coefficient at the effect due to current imbalance, using the phenomenological model highlighted on figure 4-14 and typical parameters. These two examples show that the current imbalance effect can be quite severe and may totally deteriorate the system performance.

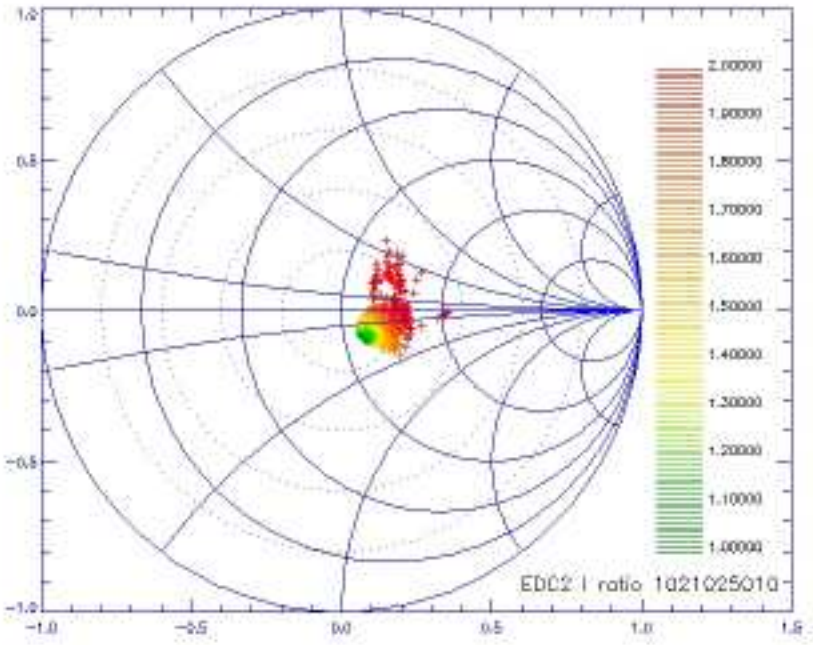

Figure 4-15: Simulated reflection coeffi cient at DC2 for a typical discharge - without current imbalance effects.

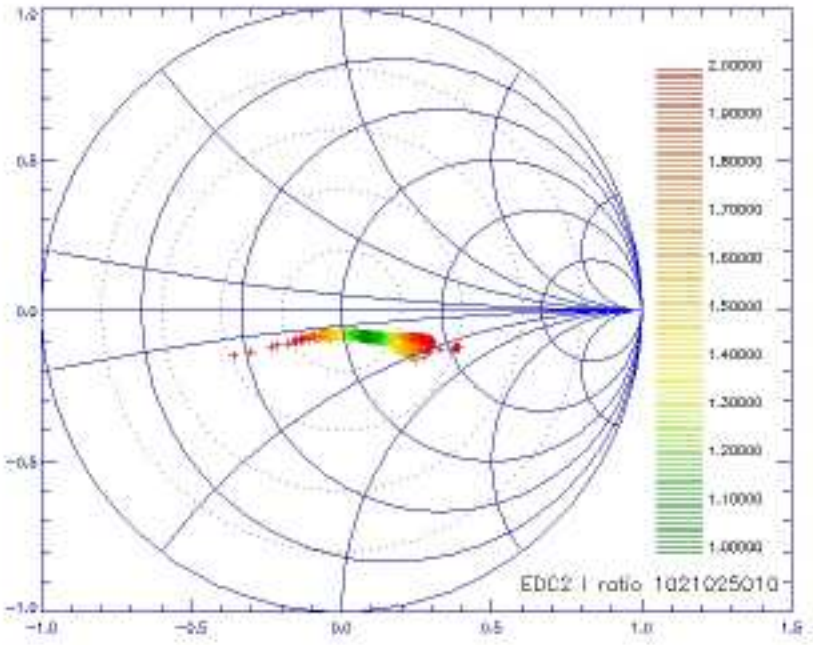

Figure 4-16: Simulated reflection coeffi cient at DC2 for a typical discharge - with potential current imbalance effects.

4.2.3 Impact on Antenna behavior

Another source of concern associated with the current imbalance effect is the degradation of the phasing control, and its effect on antenna behavior, heating efficiency and overall performance. For the specific configuration in D and E, only the poloidal phasing is expected to be affected, as more current might be present on the upper strap than on the lower, or the opposite. Most antennas have their poloidal phasing centered around zero, and it is not clear which effects can be expected from an uncentered poloidal spectrum. The heating efficiency may be reduced in this case, and it is not excluded that loading variations could result from this as well.

As introduced in chapter 2, the phasing of the antenna is also critical to obtain low impurity production. If the single pass absorption is not degraded by the load tolerant configuration, only near field effects could come into play. The main impurity release mechanism would then be come from the Faraday shield. The standard model for this phenomena has been developed in JET [10] and TFTR [26]. As the current is reduced in the upper part of each strap and increased in the lower part by the current imbalance effects described above, we expect only a partial cancellation of the magnetic fluxes between adjacents along the field lines, although the effect should not be as severe as in the pure monopole case.

Chapter 5

Fast-matching system based on ferrite tuners

In this chapter, we present impedance matching networks suitable for a fast matching systems and introduce a principle design for a ferrite-loaded phase shifter. In the next chapter, we will present ferrite materials and their behavior in more detail, leading to more precise design guidelines in chapter 7.

5.1 Impedance matching systems using ferrite tuners

Different impedance matching networks can be used with a quick-response time ferrite phase shifter. We focus here on the *Phase shifter-Stub tuner* network and the *Double stub tuner* network, which will be presented in the next two subsections. While the systems work well with ideal phase shifter and stub tuners, using ferrite loaded tuning components may create some deviations from the standard behavior. This will be discussed in a third subsection.

5.1.1 Phase shifter - stub tuner matching network

The phase shifter/stub tuner matching network is shown on figure 5-1. As its name suggests, it consists of a pair with one $\frac{\lambda}{2}$-tunable phase shifter and one $\frac{\lambda}{2}$-tunable stub tuner.

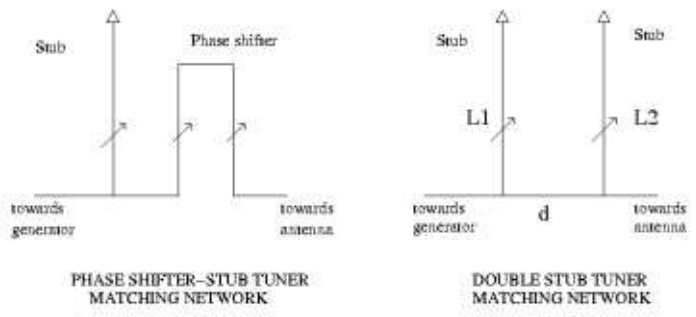

Figure 5-1: Schematic layout of phase shifter-stub tuner and double stub tuner matching networks.

There is no limitation on the ranges of impedance which can be matched ; however, strong mismatch imposes stub lengths close to zero or $\frac{\lambda}{2}$ at the operating frequency, and the system becomes diffi cult to adjust for perfect match.

In general, there are two solutions for the lengths of the tunable elements which lead to matched conditions for a certain loading. The procedure is rather simple. The phase shifter is adjusted so that the real part of the impedance at the tee of the shunt stub corresponds to 50Ω ; the stub length is then set to cancel the imaginary part of the effective load at the tee, thus leading to a 50Ω load back to the transmitter.

One technical diffi culty with the phase shifter-stub tuner network stems from the design requirement of a low loss and high power phase shifter. We will adress this issue in chapter 7.

5.1.2 Double stub tuner

The double stub tuner network is an alternative to the phase shifter-stub tuner network. Its main advantage comes from the use of stub tuners only, which are easier to design. However the system cannot match all load impedances. A schematic layout is given on fi gure 5-1.

For a distance $L = \frac{3\lambda}{8}$ between the two stubs, the so-called *forbidden area* is shown of fi gure 5-2. As this area can be rotated by an appropriate additional transmission line, it does not appears too restrictive.

For a given load impedance $Z = G_L + jB_L$, two possible electrical length settings are

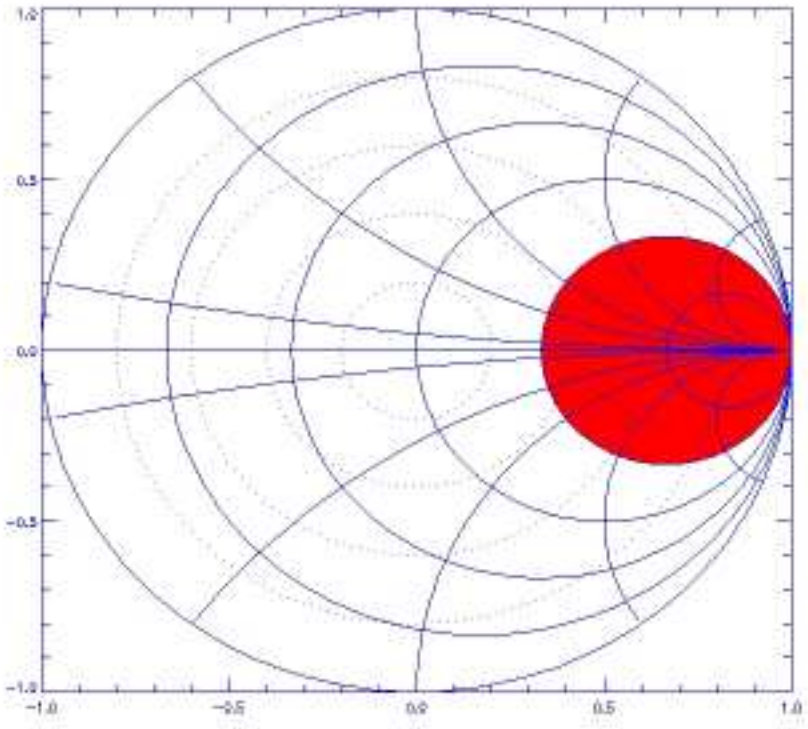

Figure 5-2: Forbidden area for the double stub matching network.

available for the matching in a double stub tuner network :

$$L_1 = \frac{\lambda}{2\pi} tan^{-1}\left(\frac{G_L t}{\pm\sqrt{G_L(1+t^2) - G_L^2 t^2} + G_L}\right)$$

$$L_2 = \frac{\lambda}{2\pi} tan^{-1}\left(\frac{1}{-B_L + \frac{1\pm\sqrt{(1+t^2)G_L - G_L^2 t^2}}{t}}\right)$$

where $t = tan\frac{2\pi d}{\lambda}$ and d is the electrical length of the transmission line between the two stubs. The $\pm$ go together.

An interesting way to decrease the costs of the system is to use a double stub tuner matching network with one or two $\frac{\lambda}{4}$ stubs instead of the less restrictive $\frac{\lambda}{2}$ stubs. It turns out that the first stub limits the matching area vertically, and the other one horizontally. Although the possible matching area is significantly reduced, with a load with rather constant characteristics, this solution may be used. Using the two solutions increase the flexibility. However, for an automated approach, restricting the system to one solution will allow for

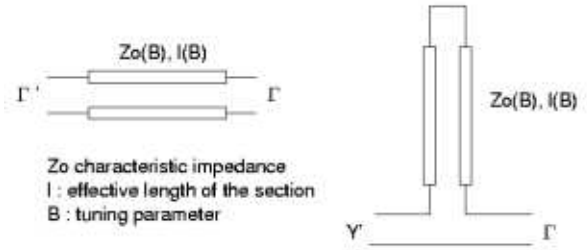

Figure 5-3: Variable impedance phase shifter and stub tuner.

a smooth control function.

We saw in chapter 3 that the typical range of impedances at DC2 for the D and E antenna networks is relatively narrow. It turns out that a double $\frac{\lambda}{4}$-stub tuner network can match typical loads for the two antennas. The costs of implementing this network are signifi cantly lower than for a standard double $\frac{\lambda}{2}$-stub tuner network, and the design of the components is also easier in this case.

5.1.3 Effect of variable impedance stub-tuner/phase shifter matching devices

Using ferrite-loaded phase-shifters or stub tuners may introduce signifi cant deviations for the ideal behavior above. Indeed, as the permeability of the ferrite is changed, we also expect the impedance of the waveguide to vary, as it should depend on $\sqrt{\frac{\mu}{\epsilon}}$. Therefore the impedance of the tuner will change as we vary their electrical length by applying the external magnetic fi eld. To take this into account, we can model the tuners as transmission lines whose electrical length l and impedance Z are function of a tuning parameter, here denoted by B. The functions $l(B)$ and $Z(B)$ are assumed to be known beforehand, either through calibrations or simulations. Figure 5-3 shows a schematic representation of this model.

Variable impedance phase shifter

The variable impedance phase shifter corresponds to a transformer with impedance $Z(B)$ and length $l(B)$. Therefore its behavior is rather straightforward. Compared to the standard phase-shifter, $Z(B) \neq Z_0$ will induce a change in the magnitude of the reflection

coefficient in addition to the phase change. The effect is rather straightforward on the Smith Chart, as the mismatch will shift the center of rotation for the match point together with the angle of rotation as B is changed. The mathematical formalism is less simple, and if Γ is the complex reflection coefficient at the unmatched side of the tuner, the reflection coefficient in the tuner will be :

$$\Gamma(x) = \frac{(1+\Gamma)Z_0 - (1-\Gamma)Z(B)}{(1+\Gamma)Z_0 + (1-\Gamma)Z(B)} exp(4i\pi \frac{l-x}{\lambda})$$

Therefore the reflection coefficient at the matched side is given by :

$$\Gamma' = \frac{(1+\Gamma(0))Z(B) - (1-\Gamma(0))Z_0}{(1+\Gamma(0))Z(B) + (1-\Gamma(0))Z_0}$$

The overall behavior is essentially the same as for an ideal phase shifter, and this formula can be used to take variable impedance effects into account for the control system.

Variable impedance stub tuner

The stub tuner can be modeled as a phase shifter shorted at one end and in parallel with the input branch on the unmatched side.

The reflection coefficient at the end of the tuner, before the transition to the 50Ω network, is then simply $\Gamma(0) = -exp(4i\pi \frac{l}{\lambda})$. The admittance of the two branches add, and therefore the resulting admittance at the matched side is, if Γ is the reflection coefficient at the unmatched branch:

$$Y' = \frac{Z_0^2}{Z(B)} \frac{1 + exp(4i\pi \frac{l}{\lambda})}{1 - exp(4i\pi \frac{l}{\lambda})} + Z_0 \frac{1-\Gamma}{1+\Gamma}$$

From this expression, we see that the variable impedance does not introduce any fundamental change in the behavior of the stub tuner, as no dissipative part is involved. The variable impedance only modifies the functional dependence of the stub susceptance with respect to the controlled parameter B, with no change in the accessible range. Within this model, therefore, the double stub tuner matching network should essentially behave the same way, with different *effective* lengths.

For given functions Z(B) and l(B), we can determine the *effective* length l_{eff} of a stub tuner which would lead to the same reactive component as the variable impedance stub

tuner. We need to solve :

$$\frac{Z_0}{Z(B)}\frac{1+exp(4i\pi\frac{l(B)}{\lambda})}{1-exp(4i\pi\frac{l(B)}{\lambda})} = \frac{1+exp(4i\pi\frac{l_{eff}(B)}{\lambda})}{1-exp(4i\pi\frac{l_{eff}(B)}{\lambda})}$$

It is important to track situations when the effect of the variable impedance would compensate the phase shift in the tuner and therefore reduce the variations in the effective length. This can be done as Z(B) and l(B) are known. At this point, we assume the following dependence :

$$l(b) = \frac{\lambda}{4}(1+b)$$

$$Z(b) = Z_0(1+\frac{b}{2})$$

In this situation, the reactive component Im(Z) = Y added by the stub is plotted on figure 5-4. Like for the phase shifter, we see that in this case, the variable impedance does not affect the overall behavior of the stub tuner, but it must be taken into account.

From this we conclude that in principle, variable impedance tuners should not significantly impact the expected behavior of double stub tuner or phase shifter/stub tuner matching networks. The deviations from ideal tuners must be taken into account for the control system, however.

5.2 Principle design of ferrite tuners

Different transmission line geometries are available for transmission of high power RF waves. The dielectric volume - usually air or a gas with better breakdown voltage characteristics - between the inner and outer conductor can be partially or totally loaded with a ferrimagnetic material, which affects the propagation velocity. The magnetic properties of the ferrites can be varied using an external field, thus allowing some control on the effective electrical length of the device.

The applicability of this technique for our purposes is mainly limited by:

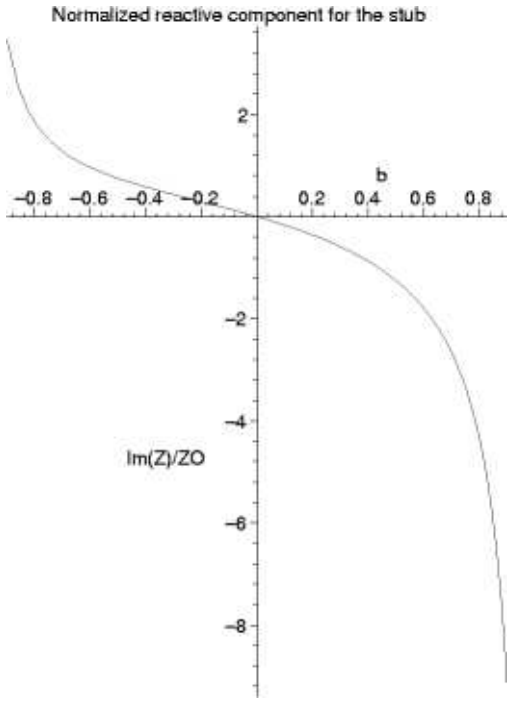

Figure 5-4: Reactive component added by the shunt stub as a function of the control parameter b for the example shown here.

- **1. Power dissipation and heat release** Ferrites are lossy materials in certain conditions, and the dissipation of RF power in the ferrite leads both to a net power loss in the device and to substantial and potentially damaging temperature increase in the ferrites.

- **2. Size, cost and weight** The 3.75 m wavelength at 80 MHz imposes constraints on the dimensions of the device to obtain appropriate electrical length excursions. Ferrite materials, as well as magnets, are costly.

- **3. Tuning speed** The tuning speed of the device is limited by eddy currents effects in the structure and the self-inductive response of the coils.

- **4. Electric breakdown** As the size of the device is reduced, the electrical field can be substantial in the structure, leading to electrical breakdown.

- **5. Transitions to coaxial lines** If the retained geometry is not coaxial, a appropriate transition is required. Its transmission and reflection properties should be compatible with operation constraints of the device.

On the overall, these issues are related both to the chosen waveguide geometries and specific behavior of ferrite materials. In this section, we introduce the first aspect, while the second, which requires more information of the physics of ferrites, will be examined in the next chapter.

Two categories of waveguide geometry have been studied as possible candidates for this design.

5.2.1 Rectangular/Ridged waveguide

The electrical length variations for a rectangular/ridged waveguide are obtained with thin ferrite slabs located respectively in the walls of the rectangular waveguide and between the ridges for the ridged waveguide. The phase shift is obtained by changing the boundary conditions of the waveguide, which affects the group velocity of the waves.

Regarding the losses, the ferrite-loaded rectangular waveguide phase shifter possesses the very desirable property of having most of the power flow outside the ferrite material. It is not the case for the ridged waveguide or the stripline. However, modes in the rectangular waveguide are not TEM, and the TE10 is evanescent if the width of the guide is less than half a wavelength at the operating frequency. For 80 MHz, this corresponds to 1.9 meters. The height of the waveguide is then set by voltage breakdown considerations, and can be of the order of 10-20 cm. In principle, the transition to a coaxial line does not introduce any technical difficulty.

Using a ridged waveguide allows to reduce the size of the device. The width of the guide is actually lower by a factor of 3 for the same frequency range. However, to obtain the required phase shift, the ferrite slab has to be inserted in regions of high power flow. Besides, the transition coaxial line-ridged waveguide, though relatively straightforward for the non-loaded case, is somewhat complicated by the insertion of the ferrite. Higher order modes are excited in the structure.

On the overall, two main issues are encountered with both the rectangular waveguide and the ridged waveguide.

Physical size The cross-section area of the device is relatively big in both cases. As

the cost of the system depends practically on the volume between the coils and permanent magnets, this is not desirable.

Higher order modes Even if the size of the device can be made compatible with the required frequency range 40-80 MHz, the proximity to the cutoff induced unwanted effects which could not be controlled appropriately in the CST field code simulations (The code is described in the next chapter). This casts some doubt on the feasibility of the system in such conditions.

5.2.2 Stripline

The ferrite loaded stripline is another possible general geometry for a phase shifter. The wave is in a quasi-TEM mode, so that the frequency range 40-80 MHz does not impose any constraints on the size of the device. The length is set mainly by the maximum achieve phase shift/unit length, while the cross section area stems from breakdown limits and characteristic impedance considerations. The most effective geometry corresponds to ferrite slabs surrounding entirely the inner conductor. In this case, substantial power flows in the ferrite and dissipation effects can be important ; therefore, the stripline tuner has to be cooled. The transition from a coaxial line to a stripline is not problematic.

In principle, the stripline design is rather straightforward and it does not exhibit the same limitations as for the rectangular/ridged waveguide tuner. The detailed design will stem from the choice and characterization of an appropriate ferrite material, which we will explore in the next chapter.

Chapter 6

Experimental characterization of a ferrite sample

Ferrite materials have been routinely used as phase shifters in the microwave range of frequencies for more than 40 years. Signifi cant progress have been made in ferrite processing and the wide range of commercially available ferrite products makes it possible to obtain an equally wide range of properties and specifi cations, depending on the particular application. However, little use of ferrite materials is currently being done in the VHF range of frequencies (10 - 100 MHz) and therefore a theoretical approach was required to identify appropriate properties and eventual trade-off in this case. Eventually, an experimental characterization of potential samples had to be carried out.

6.1 Physics of ferrite materials for VHF frequencies

6.1.1 General description

The term *ferrites* corresponds to a class of oxide materials which exhibit *ferrimagnetism* or *uncompensated antiferromagnetism*. The spinel (general formula $MO.Fe_2O_3$ where M is a divalent metal ion like Mn^{2+}, Ni^{2+}, Cu^{2+}, Co^{2+}, Fe^{2+}, Zn^{2+} or more often combination of them) is by far the most widely used ferrite and the two terms are almost synonymous. The lattice is composed of a closed packed oxygen arrangement and between the oxygen

layers are interstices that may accommodate metal ions. The unit cell length is about 8.5 Angstrom. The interstices are divided in two categories, tetrahedral sites (8 occupied sites in the unit cell) and octahedral sites (16 occupied sites in the unit cell) ; the first are smaller, so as the divalent ions are generally larger than Fe^{3+}, we would expect them to go in the octahedral sites, unless the divalent ions have a specific electronic configuration which is favorable for tetrahedral bonding with the oxygen ions (for example Zn^{2+}). The second type of arrangement is called *inverse spinel*, while the first is called *normal spinel*.

Because of the super-exchange interaction, the magnetization of the two sublattices are antiparallel below a certain temperature (Neel temperature), but as the sublattices are composed of ions which different magnetic moments and as the sites are not symmetric with respect to the super-exchange interaction intensity, they do not compensate like in antiferromagnetism : there is a *spontaneous magnetization* or *polarization*, even without an applied magnetic field.

In bulk material, domains containing about $10^{12}$to 10^{15}atoms with parallel magnetization are formed, and their dimensions are on the order of microns. Their size and shape are determined by the minimization of the magnetostatic energy, the magnetocristalline anisotropy energy, the magnetrostrictive energy and the domain wall energy. The dynamic behavior of domains is described by two mechanisms, magnetization rotation and domain wall motion. If we start with a demagnetized specimen and increase the static applied magnetic field, reversible then irreversible motion of walls occurs to enlarge the volume of domains whose magnetization is in the direction of the field, increasing the total magnetization in this direction. Finally, when the external field is high enough, the magnetization in the remaining domains will rotate and align to the direction of the field, thus leading to *saturation*. There is an infinite number of degrees of magnetization between the unmagnetized and saturation conditions. The transition is described by the magnetization curve and the ratio M/H is defined as the magnetic susceptibility.

The constitutive relation of the ferrites follows from $\underline{B} = \mu_0(\underline{H} + \underline{M})$. If the variations of H are large enough compared to the saturation field, then the B-H relation is a typical *hysteresis* loop. The ratio μ=B/H is called the *magnetic permeability*. Note that even if H does not vary up to the saturation field, the B-H curve might show a hysteresis-like loop

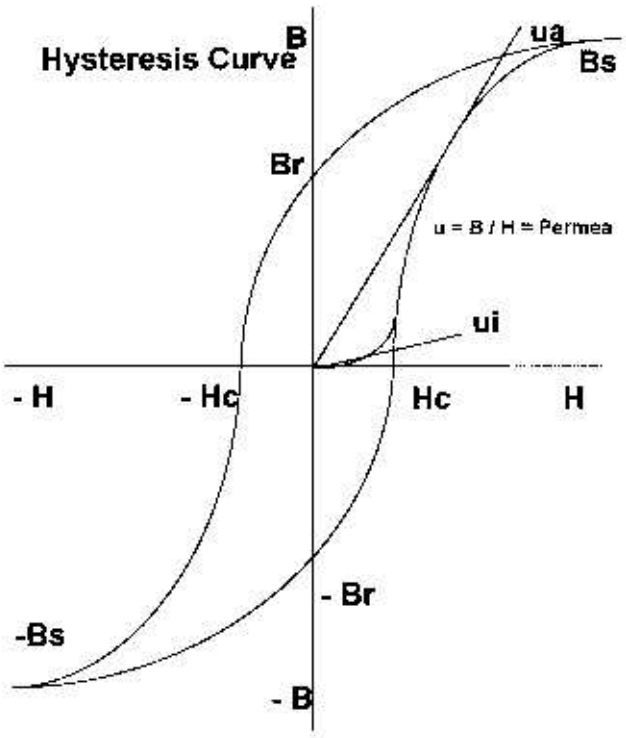

Figure 6-1: Typical hysteresis curve for ferrite materials.

form, a *minor loop*.

6.1.2 AC properties

As the AC current goes through one sine-wave cycle, the magnetization goes through one hysteresis loop. This loop is different from the DC loop, due to additional losses, in particular those linked with eddy currents, or equivalently, magnetic diffusion. As the resistivity of the ferrites is high, compared to metallic materials for example, eddy currents do not result in signifi cant losses until relatively high frequencies (UHF and above) are reached. As a result of these losses, the permeability is frequency-dependent and it tends to decrease with frequency. Empirically, this decrease takes the form of a limit for the product $f\mu$ of the frequency and the initial relative permeability, typically 3×10^9 Hz. This frequency-permeability equation is often called Snoek's limit.

At high frequencies, the magnetization does not cycle only in phase with the alternating magnetic fi eld any more, and we must introduce a dissipative out-of-phase component for the B-H relation. Therefore we defi ne a complex permeability $\mu = \mu_1 + j\mu_2$. The frequency

dependence of μ is illustrated in figure 6-2 in the Megahertz range of frequencies.

In analogy with lossy dielectric materials, we define a magnetic loss factor $= \frac{\mu_2}{\mu_1}$. Higher loss factors correspond to higher losses.

6.1.3 Specific AC losses in the VHF range

In the VHF range, two additional losses occurs.

The first one is related to *domain wall motion* driven by the time varying magnetic field [3]. To this resonance phenomena, in which the domain walls move in phase with the RF field, is associated damping losses in the VHF range, typically around 50 MHz. By pulverizing the ferrite and creating thus a powdered structure, it is possible to restrict the domains to the very small volumes of the grains and therefore to suppress wall motions and associated losses. Eddy currents losses are also reduced in this case, but it is harder to obtain high initial permeabilities.

The second one is caused by ferromagnetic spin resonance in the natural internal magnetic field and are commonly called *low-field losses*. The internal anisotropic magnetic fields for a powdered specimen actually depend on the shapes of the randomly oriented domains in the ferrite. For a powdered ferrite, the anisotropic field B_{anis} results from the particles and we can model the corresponding domain using tiny spheres, slivers and flat chips [27]. Given this broad variety of shapes, a broad range of resonant frequencies $\omega_r = \gamma B_{anis}$ is expected and typically low-field losses occur from 100 MHz to several GHz. By applying an external magnetic field, the internal fields for each particles can be increased and the resonant frequency range might be displaced to higher frequencies. Thus, low field losses might be significantly lowered in the low VHF range (10-100 MHz) by applying a moderate DC external field.

6.1.4 Magnetization curves for powdered specimens

As we mentioned above, in powdered ferrites, domain wall motion is eliminated by effectively producing single particle domains. Residual anisotropy still exists in the grains, and therefore the grains exhibit an easy axis of magnetization to which the magnetization

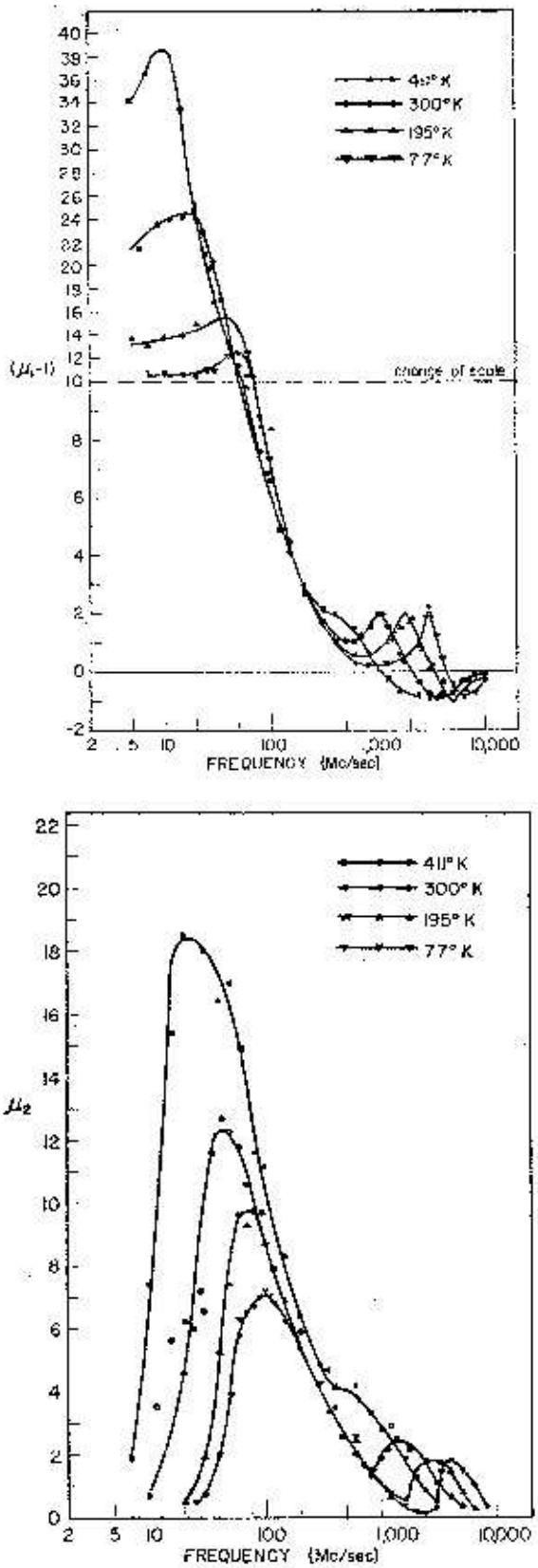

Figure 6-2: Example of initial permeability dependence on permeability, for different sample temperatures. From [3]

of the grain tends to relax. The applied magnetic field induces a rotation of the domain magnetization from the easy axis ; if the applied magnetic field is weak, the magnetization can rotate back to the easy axis upon removal of the field. This is called *reversible magnetization rotation*.

If the externally applied field is further increased, the domain magnetization can rotate irreversibly toward the direction of the magnetic field. As the field is removed, the magnetization does not necessarily return to its original direction, but instead to the closest easy axis in terms of angle. This is *irreversible magnetization rotation*.

The magnetization curve for bulk material results from the addition of these effects [28] for randomly oriented single-domain particles. Typically, irreversible rotation occurs above a given critical field, while below this field the magnetization varies reversibly with the applied field. As the field is increased, the magnetization increases in the direction of the field and this increase is lower if the externally applied field is already high.

6.1.5 Ferrite tuner in the VHF range - Appropriate ferrite materials

As we explained above, a ferrite tuner relies on the ability to change the permeability of ferrite material by changing appropriately an externally applied magnetic field. In the microwave range of frequencies, this effect is obtained using the ferrimagnetic resonance, which results in a peak of the permeability around the frequency given by $\omega = \gamma H_0$, where H_0 is the externally applied field. By changing the field, the resonance frequency is changed and if this is done around the operating frequency, significant variations of μ are induced. To obtain the same effect in the VHF range, we need an external field $H_0 \sim 28$ gauss (for 80 MHz). This is totally impractical.

For an appropriately chosen ferrite material, the initial permeability at zero field can be different from 1 in the VHF range. Therefore, varying an external magnetic field for zero field to the saturation field will effectively induce a variation of the permeability between $\mu_{initial}$ and 1.

From the general characteristics above, a set of criteria in our specific case can be obtained. Namely,

- **1. Initial permeability** The ferrite material chosen must exhibit high initial permeability in the 40-80 MHz range. If possible, the variation with the frequency should be small.

- **2. Resistivity** To avoid eddy currents losses, the resistivity of the ferrite must be high.

- **3. Microstructural aspects** The chosen ferrite must be powdered, with small and if possible homogeneous grain size

- **4. Saturation field** As the external field is to be varied to reach saturation ($\mu = 1$), the saturation magnetization must be small

Experimentally, high frequencies and high permeability are incompatible. As we also mentioned before, powdering processes also reduce the permeability compared to sintered materials. The condition 2. is usually obtained by using NiZn ferrites, which display high resistivity [29] while retaining high permeability.

6.2 Experimental characterization of a potential ferrite sample

From the criteria above, a potential ferrite sample (TT2-101) has been purchased from the Trans-Tech company. TT2-101 is a powdered NiZn ferrite, with $4\pi M_0 \sim 3000$ gauss. Measurements of the initial permeability in the low VHF range have been provided by Trans-Tech :

	μ'	μ''	Magn. loss factor
33 MHz	35.199	0.33871	0.01
55 MHz	45.819	4.6653	0.10

A small size experiment has been built with two sample pieces in order to characterize the RF properties of the material for the specific application discussed here.

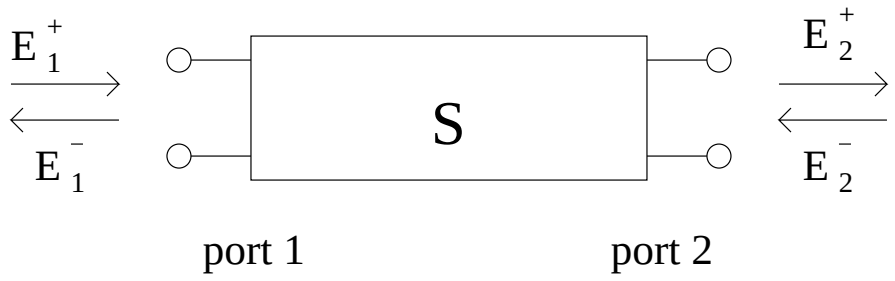

Figure 6-3: Schematic two port component.

6.2.1 Experimental setup

Two TT2-101 ferrite slabs (0.5" x 1" x 6") were used to assemble a ferrite loaded stripline, with an unmatched 4" to type N adapters at both ends. A network analyzer (Aligent 8753ES) allowed a characterisation of the stripline behavior under different conditions.

The S-parameter formalism is convenient to represent and analyze the measurements. The stripline section is modeled as a two port component. The two ports are labeled 1 and 2, and the forward direction is considered to be from 1 to 2. In transmission line theory, the behavior of the system is linear and therefore it can be represented through :

$$\begin{vmatrix} E_1^- \\ E_2^+ \end{vmatrix} = \begin{vmatrix} S_{11} & S_{12} \\ S_{21} & S_{22} \end{vmatrix} \begin{vmatrix} E_1^+ \\ E_2^- \end{vmatrix}$$

where the indices refer to the port, and the $\pm$ correspond to signals traveling in the forward direction (+) and reverse (-).

The S matrix contains complex S-parameters, which characterize the system behavior. S_{11} and S_{22} correspond to reflected signals, while S_{12} and S_{21} correspond to transmitted signals. We will use the term *attenuation* for the magnitude of the S-parameters, although it may be misleading for reflection. The argument of each S-parameters indicates the phase shift induced by the component. The defi nition can be extented to the case of a system with a single port, and we only need to know S_{11} in this situation.

In order to characterize the ferrite sample and determine these S-parameters under different conditions, the following experiments were conducted.

- **A. First test with small magnets** Permanent magnets were used to create a magnetic

Figure 6-4: Stripline structure between the two coils (in red) (Parts B, C and D).

Figure 6-5: Initial experiment setup (Part C - Power test).

field of about 500 Gauss in the line and to induce phase shifts in the line. The field was uncontrolled and only parts of the line could be magnetized, but the goal was to determine if promising phase shifts could be obtained.

- **B. Coil setup** To obtain an homogeneous field, two magnetic coils were used, up to 3000 Gauss. The current-field curve for the coils was obtained with a Gaussmeter. S-parameters were then obtained with applied magnetic field, in both directions perpendicular to the propagation direction. The phase shift data was obtained as a function of the applied field, and reflection/transmission coefficient would give information on the impedance of the line through CST modelisation.

- **C. Power test** The experiment above was repeated with a 500 W RF signal going through the line and ultimately to a 50 Ohms load. The generator was protected from high VSWR by a phase-shifter stub-tuner network, and the S21 attenuation was obtained with directional couplers at both ends and powermeters. A demodulator board allowed phase measurements. This was a check to see if some unusual behavior would take place at higher power.

- **D. Losses measurements** The line was transformed into a cavity by shorting one end using copper pieces. The S11 parameter was measured with and without ferrites in the stripline. The effect of the magnetic field was then evaluated using the permanent magnets. This was a rather quick test to evaluate our control of the losses through the applied field, as predicted for low field losses.

6.2.2 Experimental results

A. First test with small magnets The magnetic field in the ferrite was increased with permanent magnets, with a maximum field up to 600-1000 Gauss. Phase shifts up to 5 degrees could be obtained. Compared to initial CST computations, this was judged promising, given the size of the stripline and of the ferrite samples.

B. Coil setup The S11 attenuation in dB, and the attenuation (dB) and phase (deg) of S21 for the stripline have been measured for increasing values of the applied magnetic field,

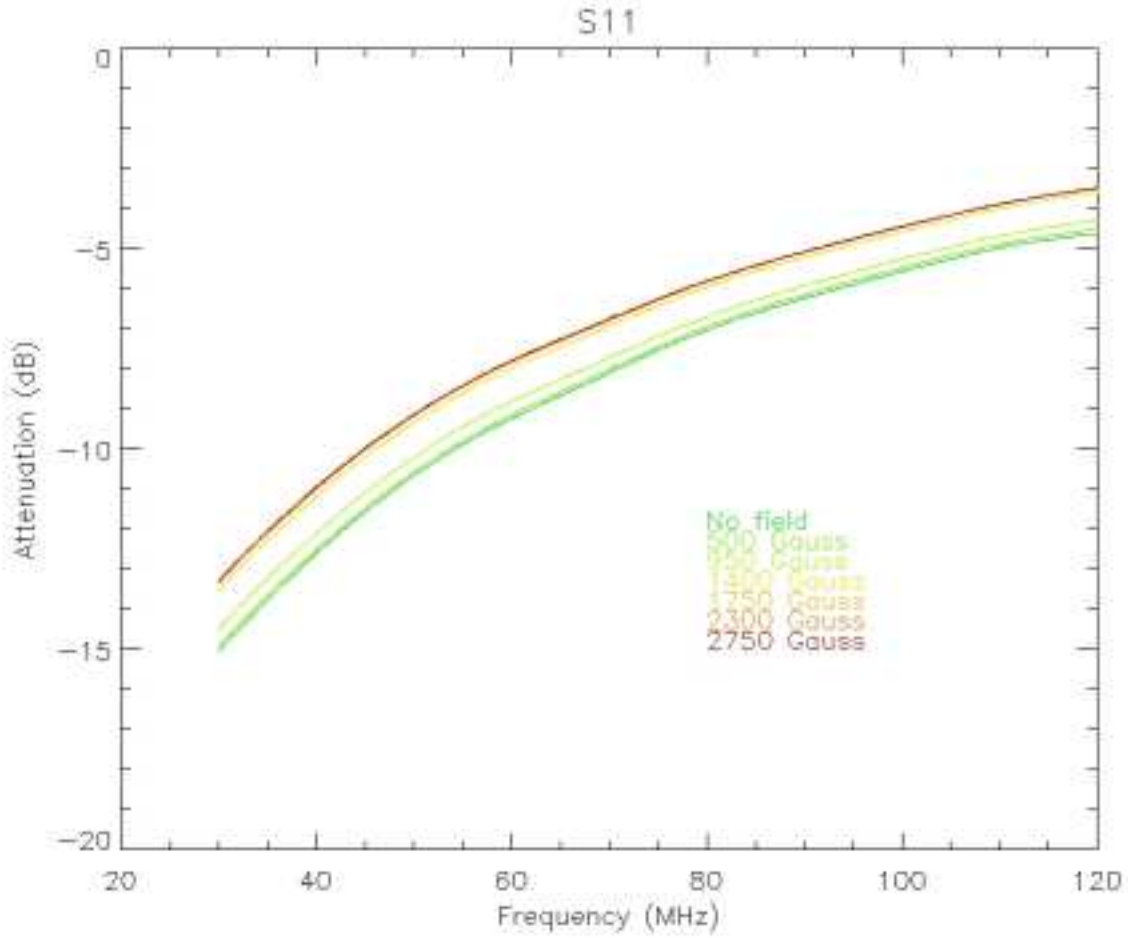

Figure 6-6: S11 attenuation for increasing values of the applied field.

up to 3000 Gauss. The results are shown on figures 6-6, 6-7, 6-8 and 6-9. Phase shifts up to 10 degrees at 80 MHz were obtained. Starting around 2500-3000 Gauss, hysteresis effects began to occur in the irreversible magnetization regime. As most of the phase shift occurs below 2000 Gauss, this means that higher magnetic fields should be avoided for the device operating range.

C. Power test For reasons of availability of transmission line sections, the power test was performed at 90 MHz. The S21 attenuation is deduced from the forward power before and after the stripline section.

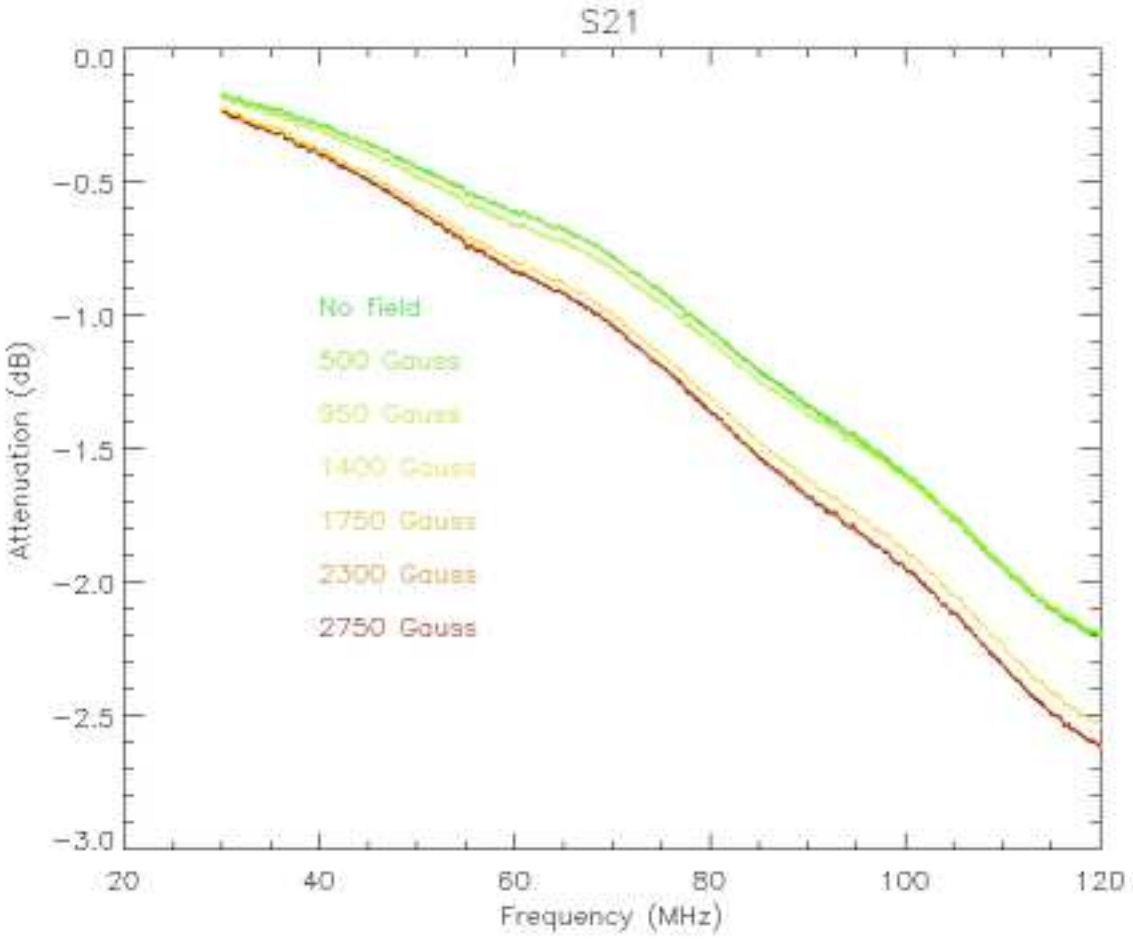

Figure 6-7: S21 attenuation for increasing values of the applied fi eld.

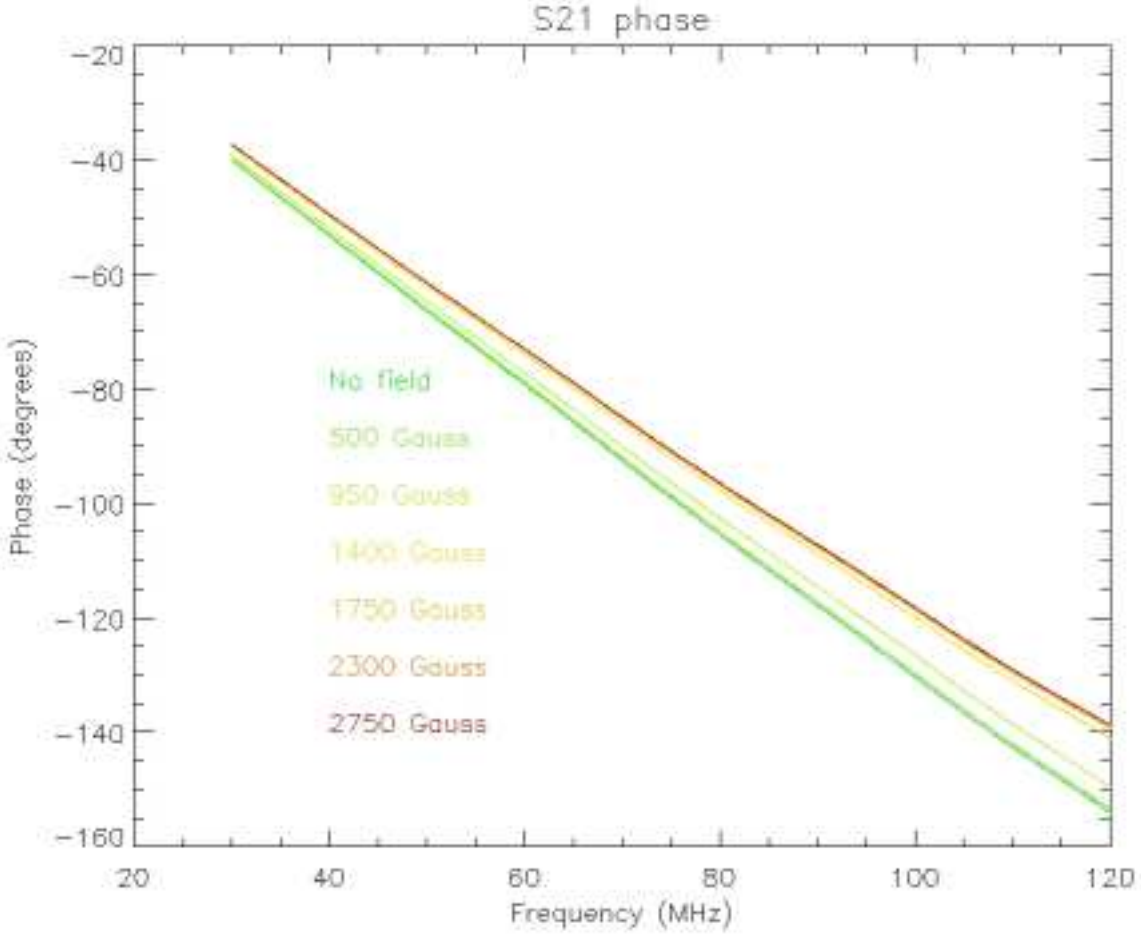

Figure 6-8: S21 phase for increasing values of the applied fi eld.

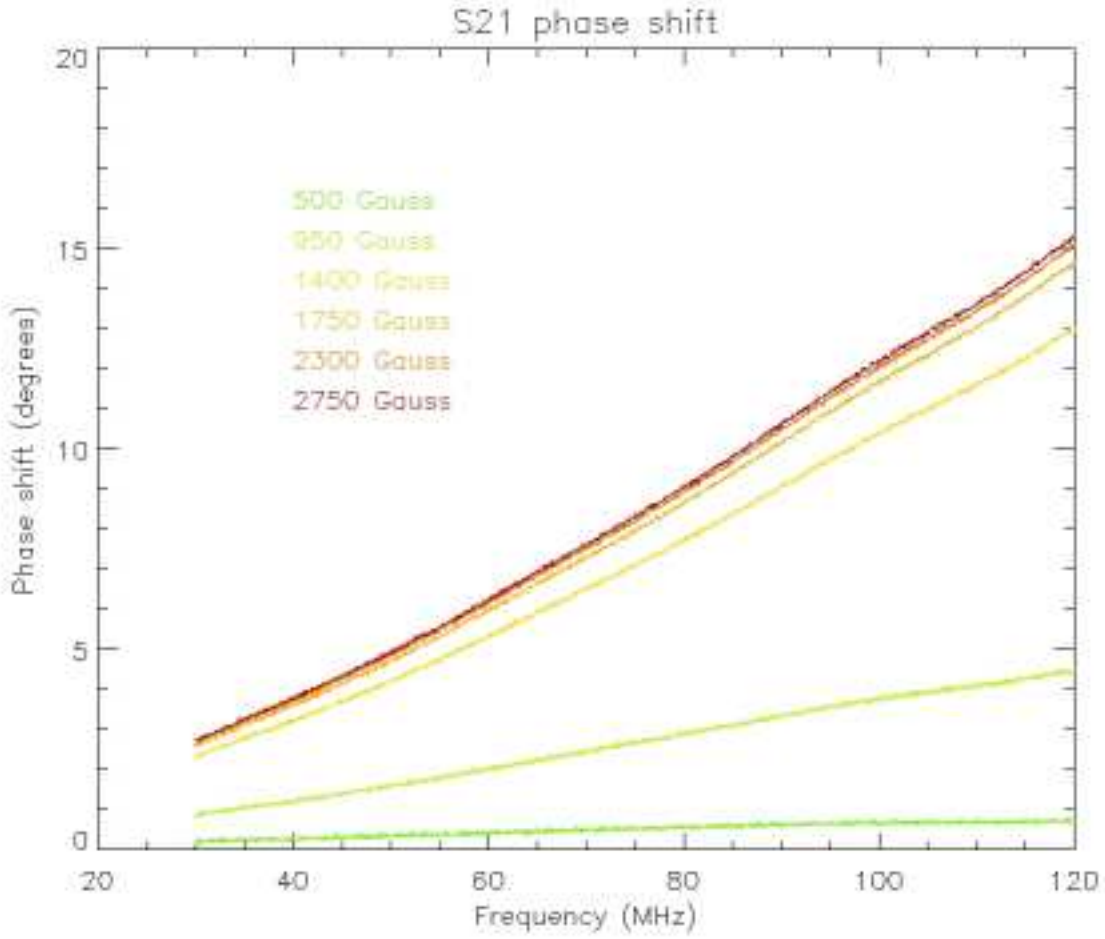

Figure 6-9: S21 phase shift (from the unmagnetized conditions) for increasing values of the applied fi eld.

Forward	No Field	1750 Gauss	4000 Gauss
100 W	73.8 W	67.0 W	67.3 W
	-1.31 dB	-1.73 dB	-1.72 dB
200 W	145.3 W	133.1 W	132.0 W
	-1.39 dB	-1.77 dB	-1.80 dB
300 W	219 W W	200 W W	202 W
	-1.36 dB	-1.76 dB	-1.72 dB
400 W	291 W	268 W	267 W
	-1.38 dB	-1.74 dB	-1.75 dB
470 W	344 W	313 W	313 W
	-1.36 dB	-1.76 dB	-1.76 dB

The maximum power density for this experiment corresponds to about half the density expected for a real size device with 1 MW of circulating power. The aim of this experiment was to detect nonlinear power effects in the guide. As can be seen from the table above, the attenuation is fairly independent of the input power, which exclude any obvious power dependence at this level.

D. Losses measurements The S11 attenuation for increasing values of the field is shown on figure 6-10. The reflected fraction increases with the applied field, which can be interpreted as reduction of the attenuation in the guide. However, mixed effects occur as the real part of the permeability is also changed ; therefore the impedance of the stripline is affected by the magnetic field, and the interpretation of this curve should be done with the EM solver.

6.2.3 CST model : analysis of the experimental curves.

The analysis of the experimental results were done using CST Microwave Studio. It is a commercial full 3D high frequency EM solver, with automated model meshing and a transient solver for time domain analysis based on Finite Integral Techniques. The code calculates generalized S-parameters, 3D electric and magnetic fields, currents and power flows. The object definition handles complex anisotropic dielectric and magnetic constants.

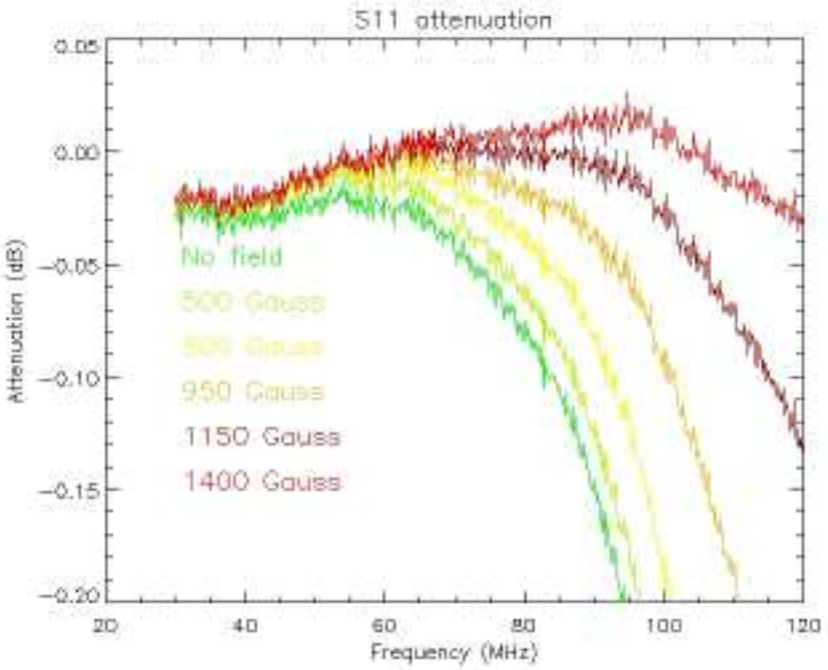

Figure 6-10: S11 attenuation for the cavity setup, for increasing values of the applied field.

In the first simulations, we assumed :

- **A. Permeability:** The permeability μ was assumed homogeneous and isotropic in the ferrite slab. We studied the effects induced by its variations over the range 1 to 40.
- **B. Losses:** The losses would induce a tractable effect on the S21 attenuation
- **C. Dielectric constant** The dielectric constant was assumed to be 13, which is the value provided at 9 GHz by the supplier.
- **D. Modes** Only the lowest order mode (quasi TEM) is relevant for this analysis.
- **E. High field permeability** At the saturation field, we expect $\mu \sim 1$

Within these assumptions, good agreement between the model and the experimental results was obtained, with input parameters in acceptable ranges. Initial curves $\mu = f(B, \nu)$ - where B is the applied induction and ν the frequency - could be obtained. $\epsilon \sim 11$ gave actually better results than ϵ = 13 (assumption C). An example of the curves obtained from the phase shift is shown on figure 6-12 for ν = 80 MHz .

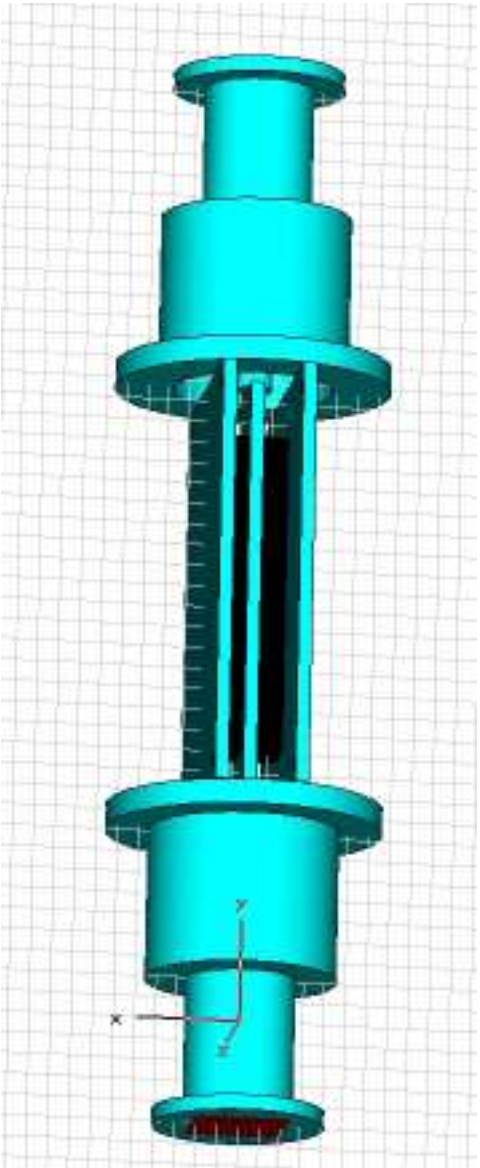

Figure 6-11: 3D view of the stripline used in the experiment, as modeled in CST.

After further analysis, it became clear that signifi cant improvements could be obtained with a frequency dependant permittivity. Mixed effects from μ and ϵ are quite common with this setup [27] ; by using the powerful CST fi eld solver and given the limited bandwidth of operation, the main effects can be captured appropriately by our approach to obtain permeability curves, but the uncertainty on ϵ makes it impossible to obtain reliable measurement of the losses from S21 measurements. Dedicated cavity experiments would be required for the estimation of the losses. In addition, the stripline was not fully loaded with ferrite, and as the target geometry emphasized a controlled and simple RF magnetic fi eld confi guration in the ferrites (namely B parallel to the midplane of the line), only a fraction of the power would actually flow in the ferrites. This introduced an additional nonlinearity from the expected $\sqrt{\mu}$ and $\sqrt{\epsilon}$ dependence of the impedance and electrical length of the line : at a fi xed frequency, the reflection and transmission CST curves were not monotonic functions of the permeability at fi xed permittivity, as shown on fi g 6-14, 6-15, 6-16.

The permeability at high fi eld can be considered as fairly accurate, but at low fi eld, the method allows a less accurate determination, resulting mainly from the assumption **E.** (above) and the $\sqrt{\mu}$ dependence, which tends to make induced variations in phase shift and impedance higher at low permeability. The curves reproduce the trends and are acceptable for initial design studies, as the permeability is only a working parameter. The fi nal analysis focus more on the impedance and phase shift, and the exact permeability curve is not critical.

The following approach was then conducted :

- **S11** Both the loss factor and the value of the permeability at zero fi eld have limited effect on the S11 curve, whereas the effect of dielectric constant variations are signifi cant. The experimental curve crosses the model curves for different values of ϵ, which we can then take as values of ϵ in the ferrite. By taking acceptable limiting values for μ 20-50 and the loss factor 0 - 0.1, we can estimate the error of this approach and it is found to be quite acceptable. The results are shown on fi g 6-13

- **S21 phase** Once the dielectric constant is determined, the variations of the phase, which are affected by changes in the phase velocity - which scales with $\frac{1}{\sqrt{\epsilon\mu}}$ - , gives a

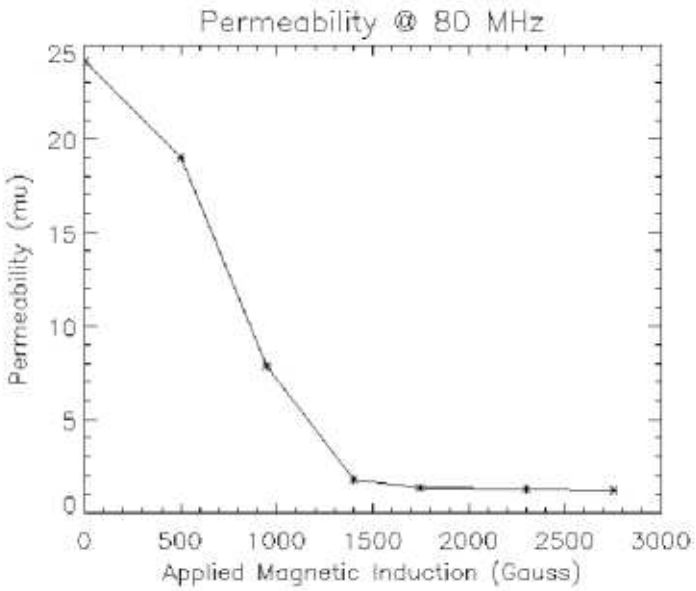

Figure 6-12: Permeability curve at 80 MHz from experimental phase shift.

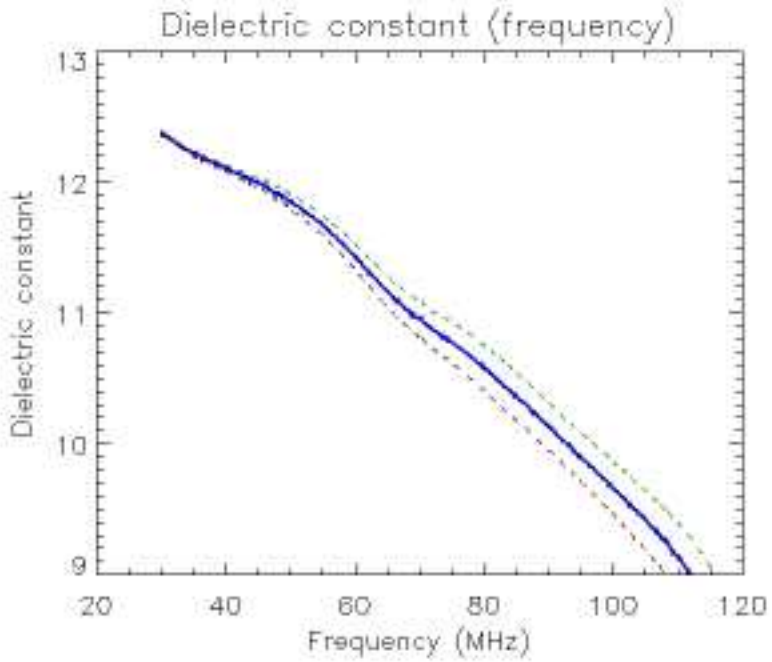

Figure 6-13: Dielectric constant versus frequency from S11. The central curve corresponds to $\mu = 35$, while the upper (green) and lower curve (red) are $\mu = 20$ and $\mu = 50$ respectively.

value of the permeability μ. With rerunning all the simulations, curves obtained with ϵ = 11 can be corrected considering the phase velocity changes with ϵ. Assuming that the dielectric constant does not change with the applied magnetic field, comparison between the model and the experimental measurements gives also the dependence on the applied field.

- **S21** The S21 curve is used to validate the process. An estimation of the losses can be obtained and confronted with losses obtained from cavity measurements. At this point, the values of ϵ and μ should give a good agreement between the S21 attenuation from the model and the experiment

The corresponding curves for this approach are shown on figures 6-14, 6-15 and 6-16 in the 80 MHz case - with $\epsilon = 10.75$. The black curve represents the modeled dependence with the permeability as computed by the CST field code. The horizontal lines correspond to the measured value of S11, S21 and the phase shift respectively, for different values of the applied field. Figures 6-14 and 6-15 can be used to deduce a permeability curve. No losses were assumed in these simulations, therefore figure 6-15 does not allow any relevant comparison.

The small deviations between the model and the experimental curves, resulting most likely from higher order modes, do not allow to obtain a precise value of μ at high field. Small deviations from the expected $\mu \to 1$ dependence lead to large errors on the value of μ at zero field, ± 5. As a result, the second approach resulted in only small improvement over the first one. This uncertainty was not judged critical for the design, as larger phase shifts occur for low values of μ, and as a permanent magnetic field would be used to suppress low field losses. The large-scale design would target a window for μ, 2-15 typically, as the results above show that external magnetic fields from 500 to 1500 can lead to permeability in this range.

Losses

The estimation of the losses is a critical part of this study, as significant losses could lead to power dissipation and heat release in the ferrites. The resonator measurements (D. above) were compared with CST simulations for different values of the loss factor, taking

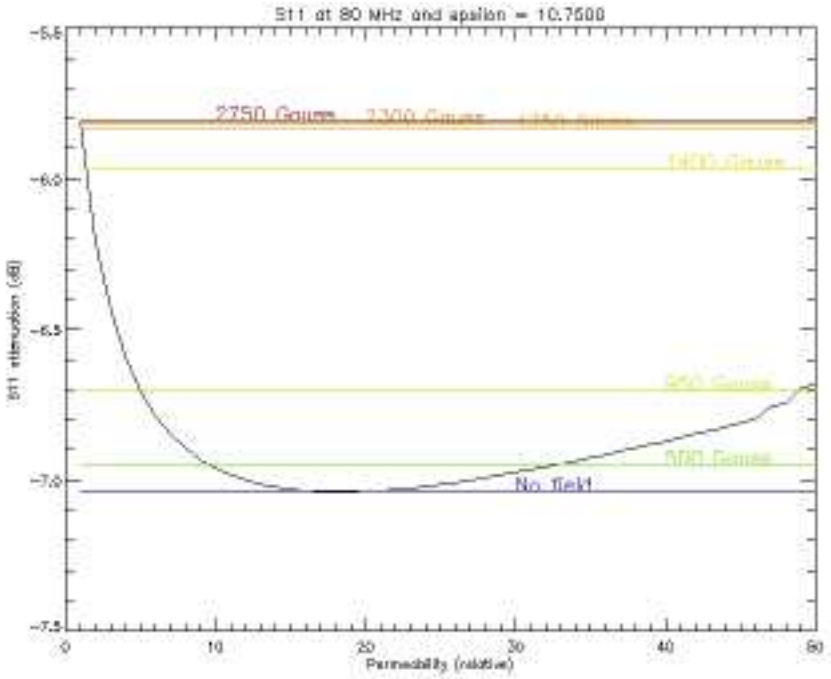

Figure 6-14: S11 attenuation comparison at 80 MHz for increasing values of the applied field.

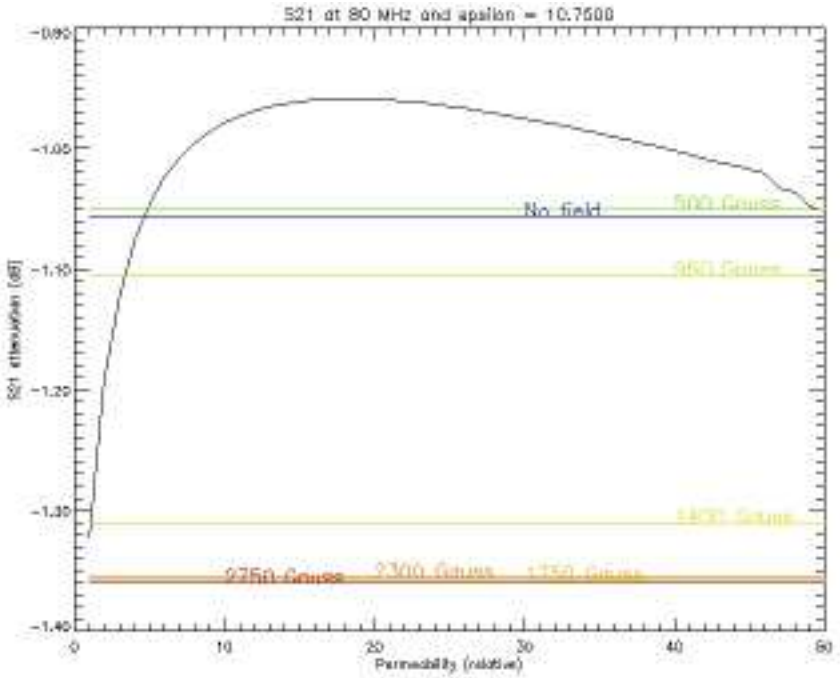

Figure 6-15: S21 attenuation comparison at 80 MHz for increasing values of the applied field.

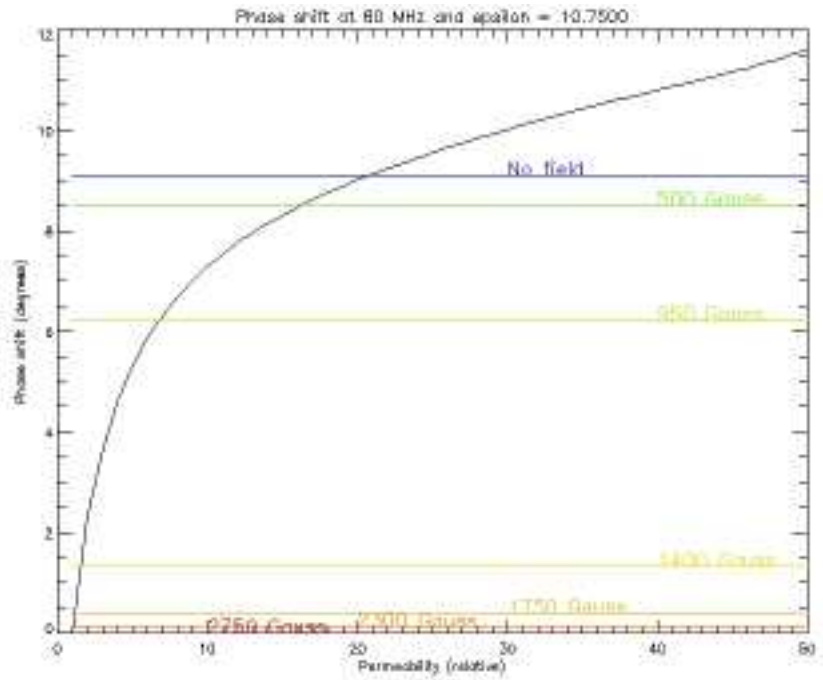

Figure 6-16: S21 phase shift comparison at 80 MHz for increasing values of the applied field.

into account the $\mu = f(B, \nu)$ and $\epsilon = f(\nu)$ dependence. The results are shown on figure 6-17. The low field losses lead to a very lossy behavior at low field, but as the field is increased, the loss factor is significantly reduced. If the field is higher than 800 Gauss, the loss factor at 80 MHz is about 0.04, and it goes below 0.02 for fields higher than 950 Gauss. This minimum field is essential for the tuner operations, and it can be obtained with permanent magnets.

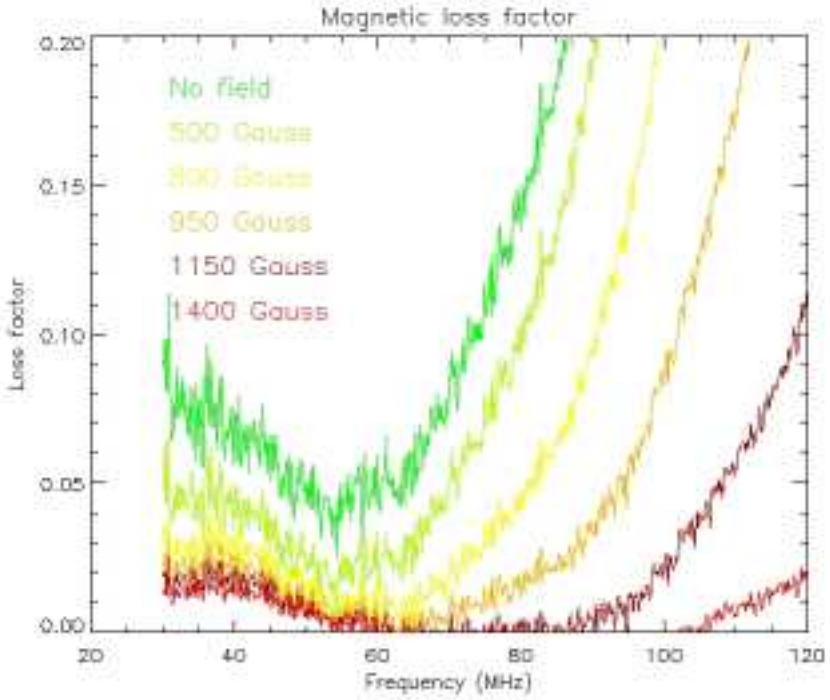

Figure 6-17: Loss factor versus frequency and magnetic field from resonator measurements.

Chapter 7

Prototype design of ferrite tuners for Alcator C-Mod

In chapter 6, we introduced the principle design for a tunable ferrite-loaded phase shifter section. While the stripline geometry could be retained before reviewing the physics of ferrite materials, many aspects of the design had to be deferred until the choice and characterization of specific ferrite species was carried out. In this chapter, we follow up on this task and review different design issues associated with the ferrite-loaded tunable stripline. Only guidelines for a practical design are given here.

7.1 Target specifications and constraints

A prototype design of ferrite tuners for ICRF fast-matching systems in Alcator C-Mod could target the following objectives for plasma operations :

Ferrite-loaded stripline phase shifter The stripline geometry was retained in chapter 5 from general considerations. The design of a phase shifter allows the inclusion in both matching systems described in chapter 5, as minor changes in the design lead to stub tuners.

1 msec tuning speed The response time of the tuners depends in the first place on the ability to change rapidly the magnetic field in the ferrites. This impacts both the design of the coils and the choice of material and configuration, as we want to minimize eddy currents.

20 MW circulating power This constraint gives an acceptable margin compared to the usual power levels in Alcator C-Mod ICRH systems, and impacts the geometric dimensions of the stripline through breakdown limits. The configuration of the external magnetic field sources must also take into account the fact that the breakdown voltage threshold is usually lowered in the direction parallel to magnetic field. The maximum electric field is usually in the space between the inner and outer plates, and perpendicular to them (vertical direction). Therefore the magnetic field direction should be oriented in the horizontal direction (figure 7-5).

45 degrees phase shift at 80 MHz The maximum achievable phase shift imposes a constraint mainly on the length of the line and level to which the line is loaded with ferrite material. 45 degrees correspond to $\frac{\lambda}{8}$ and should be appropriate for prototype testing.

Less than 3 $\%$ losses in ferrites According to the analysis in the last chapter, the losses can be reduced with the chosen ferrite material by operating at sufficiently high magnetic field, which will lower the low field losses in the operating frequency range. The final attenuation over the tuner depends also on its length and on the level to which the line is loaded with ferrite material, introducing therefore a trade-off with the phase shift requirement.

5 sec operations This will affect the cooling requirements both for the coils and the ferrites. As temperature effects could also change the behavior of the ferrites, cooling could be critical.

Minimum power demand This is an optimization goal. Given the constraints above, the target is to minimize the power demand, which means reducing the volume between the tuning coils.

The ferrite phase-shifter will be used in a coaxial transmission line network, so a transition between the ferrite tuner stripline and the coaxial lines at both end must be included in the design. High pressure SF_6 (typically 3 bars) can be used to increase the power limits for given dimensions ; this in turn imposes vacuum insulation constraints. In order to reduce the stresses on the structure and allow proper control on the magnetic fields in the stripline, non magnetic materials (copper, aluminium) should be used for the inner and outer conductors. Copper has higher electrical and thermal conductivity than aluminium, but is also

heavier. To lower the skin depth dissipation, copper plating can be used on aluminium.

The background field ~ 800 Gauss can be obtained with a set of permanent magnets surrounding the stripline. The varying magnetic field will be generated through a pair of coils, with an Helmholtz geometry. Their position will be optimized for spatial homogeneity and minimum power demand within the operating range.

For the ferrite material, we consider slabs of the TT-101 material characterized in chapter 6, with the following dimensions : 6" x 1" x 0.25".

7.2 Design guidelines

In order to optimize with the constraints above, some additional computation is required.

7.2.1 Possible stripline dimensions

The stripline geometry was investigated using the CST code, for 80 MHz. Typical parameters were inferred from the study in chapter 6 : the dielectric constant was assumed to be 10.5, and a variation of the relative permeability between 2 and 15 was considered. The CST provides an excitation of 1 Watt on one port, and determines the fields, reflection and absorption parameters.

Different runs were made to find an acceptable configuration given the constraints above. We give here one particular configuration, for which the electric field is shown on figures 7-1 and 7-1 for $\mu = 2$ and $\mu = 15$ respectively. The dimensions can be seen on figure 7-5. The electric field pattern is stronger between the plates. As sharp edges were not taken into account in the modeling, a rather conservative $15kV/cm$ breakdown limit and a maximum circulating power of 20 MW was used. With the 1 W excitation, this corresponds to 335 V/m. The magnetic field would be in the horizontal direction on these plots. The variation in μ leads to a variation in the characteristic impedance of the line from 35 to 65 Ω, which is centered around 50Ω, as desired.

A 45 cm long stripline with such dimensions leads to a 45 degrees phase shift at 80 MHz, as seen on fig 7-3. Assuming a loss factor of 0.02, these runs also allow a calculation of the dissipation, through the S21 attenuation (figure 7-4). The 3 $\%$ requirement

corresponds to an attenuation of -0.13 dB (assuming VSWR = 1).

7.2.2 Possible coil and magnets configuration

Given this geometry, we can deduce the geometry for the magnets and coils surrounding the stripline. The background field from the permanent magnet is required to be fairly homogeneous, at least within the 700-900 Gauss range for all locations covered by ferrites. One possible geometry is shown on figure 7-5. The typical remanence of Neodymium (11000 Gauss) was used for the calculation. We can see on figures 7-6 and 7-7 that the field is between 600 and 900 everywhere in the ferrite slabs. The low value at the ends of the stripline may be corrected by additional magnets if required.

Two rectangular coils create the additional magnetic field required to vary the permeability in the ferrites. This leads to the assembly shown in figure 7-8. Both the tuning speed and the volume between the coils determine the power requirements, for a given maximum magnetic field in the ferrites. With computer simulations using the COSMOS EMS 3D-field simulator [30], we can evaluate the required power for a maximum magnetic field of 1500 Gauss in the ferrites and a 1 ms tuning speed. With this particular geometry, the required power is about 50 kW.

To the assembly in figure 7-8 need to be added metallic structures in Aluminum for mechanical support and two transitions from stripline to coaxial lines at both ends. The complete assembly will also be embedded in a vacuum-sealed metallic box, in order to pressurize with SF6.

7.2.3 Cooling requirements

Losses in the ferrite slabs will tend to heat the ferrites during operations. For 20 MW of circulating power and a 3% dissipation, about 1 kW/cm^3 will be generated in the ferrites for the geometry above. With a typical density of 5 gm/cm^3 and a specific heat of about 1000 J/kgK [29], we obtain a temperature rise of 200 degrees for one second. Apart from the mechanical stress, such significant variations in the ferrite temperature can also directly impact the electrical properties.; therefore the temperature rise must be controlled.

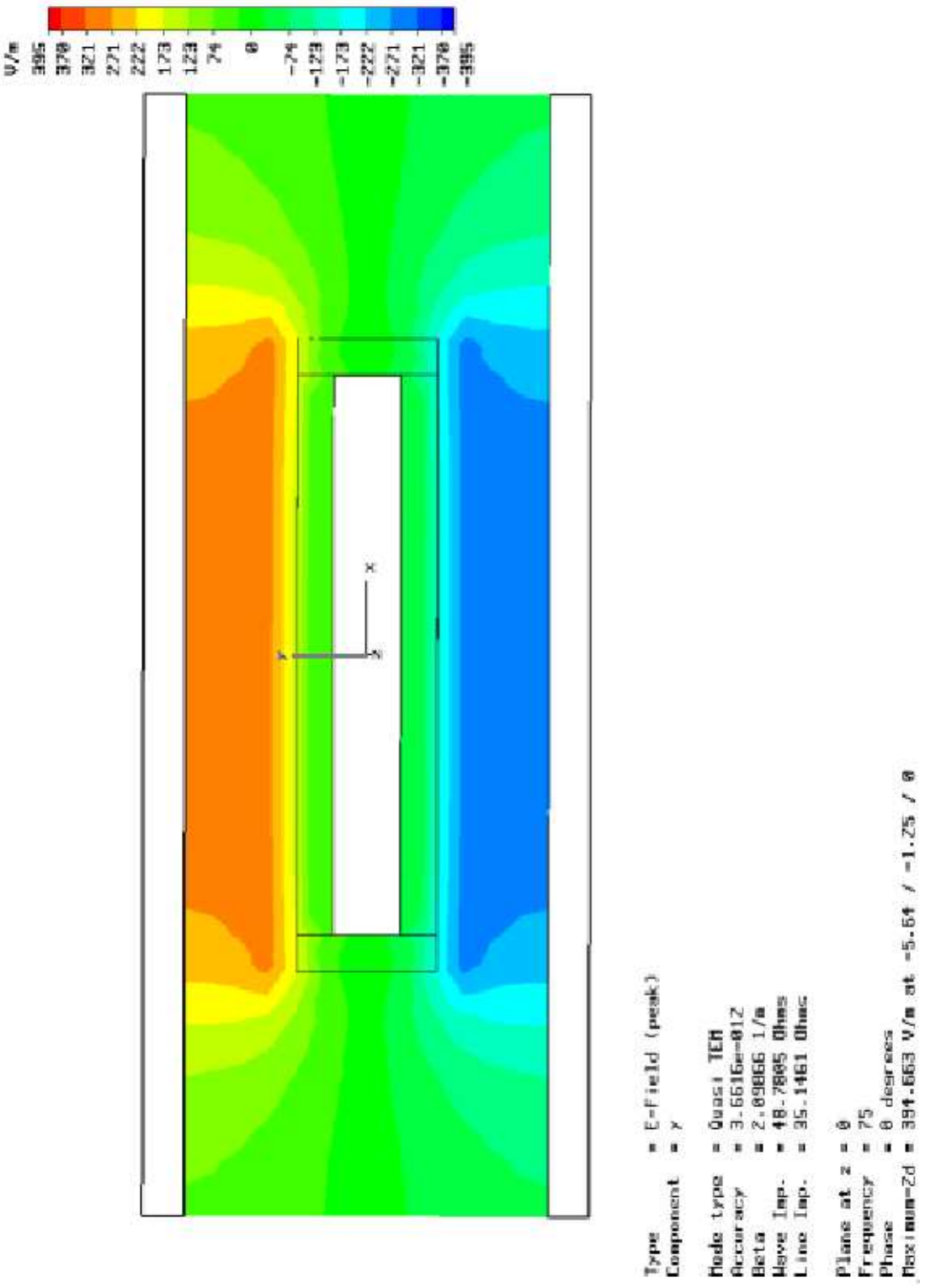

Figure 7-1: Electric fi eld strength in the stripline cross-section for μ = 15

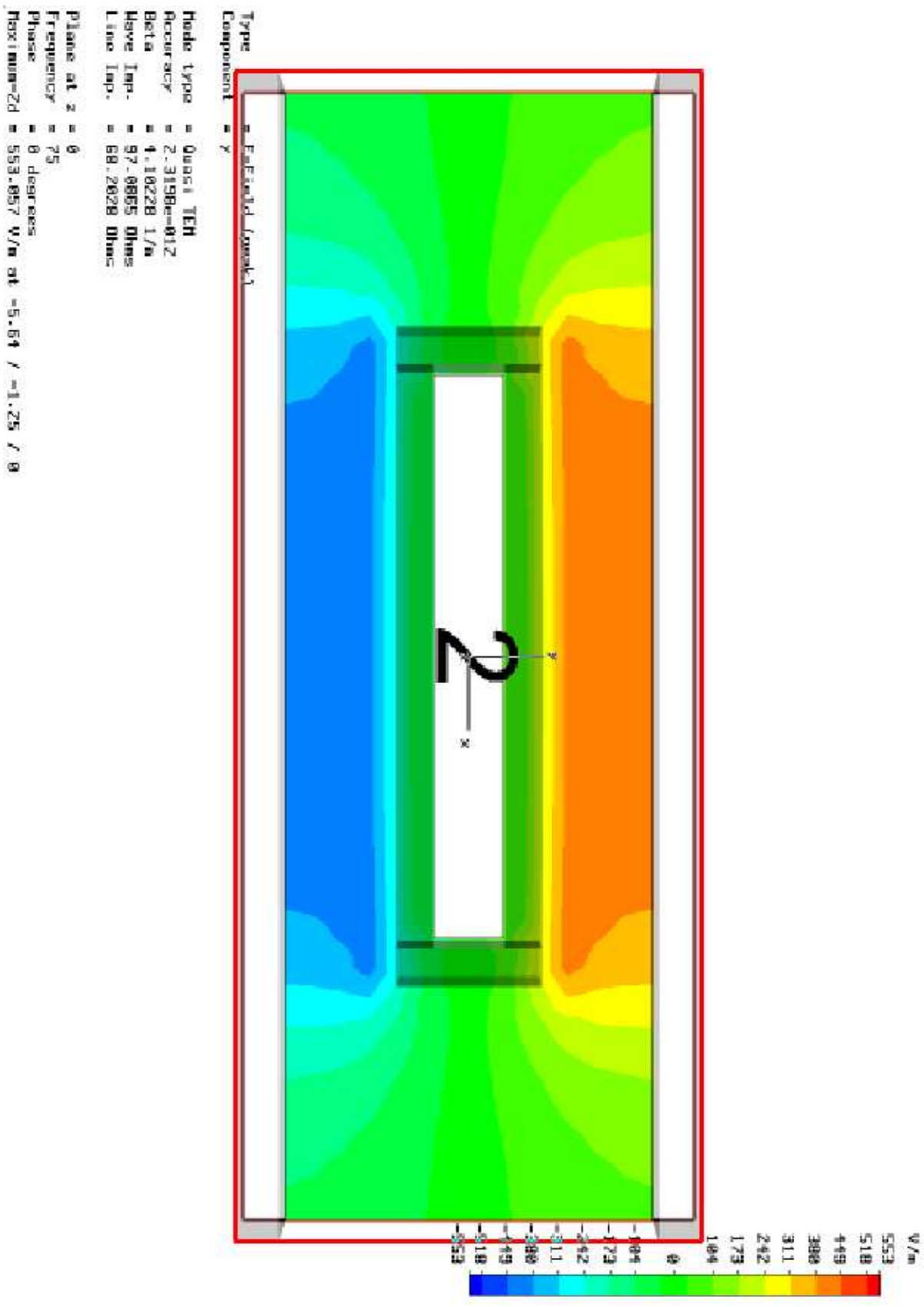

Figure 7-2: Electric fi eld strength in the stripline cross-section for μ = 3

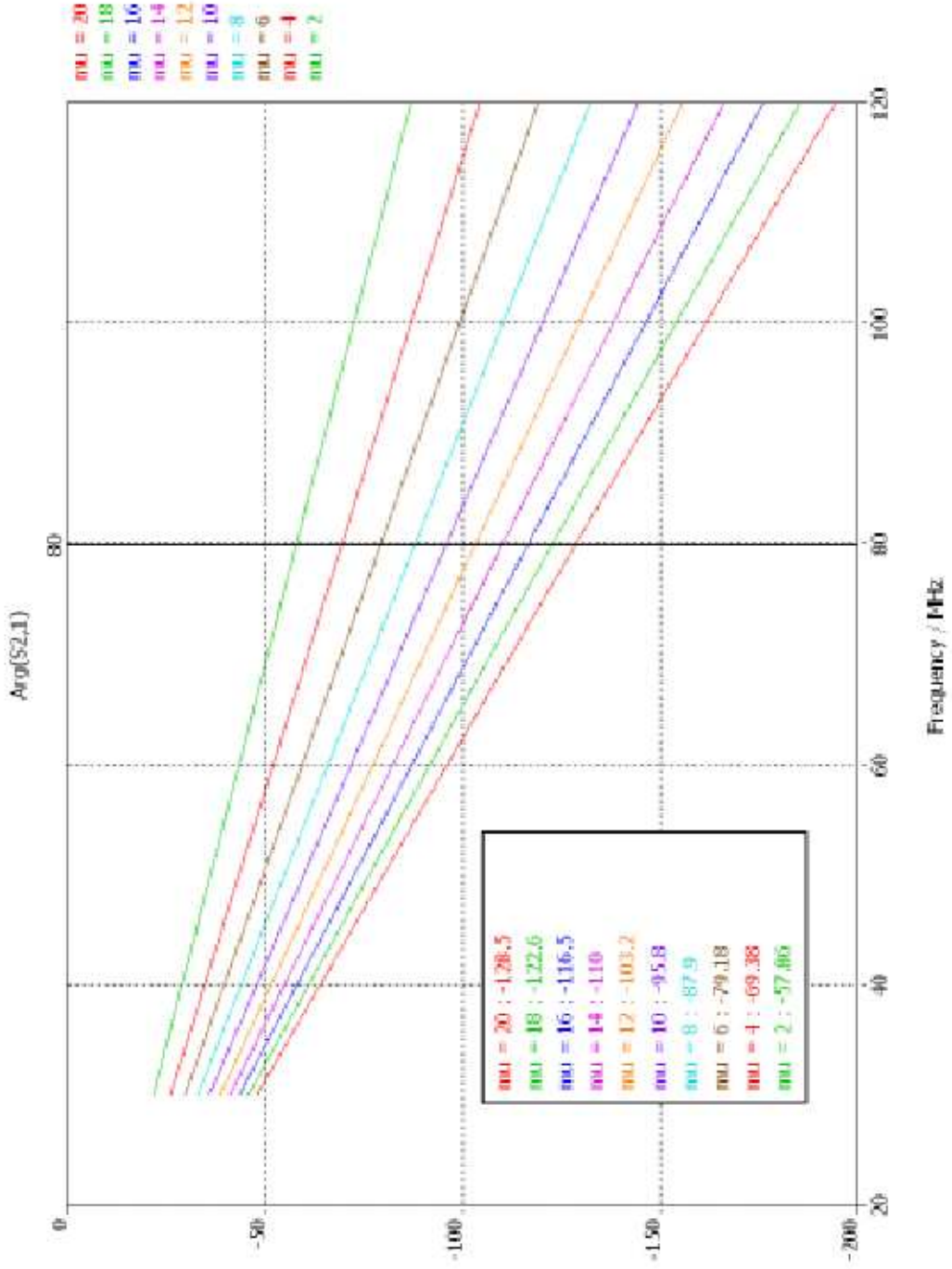

Figure 7-3: Phase shift in the stripline section as μ is varied.

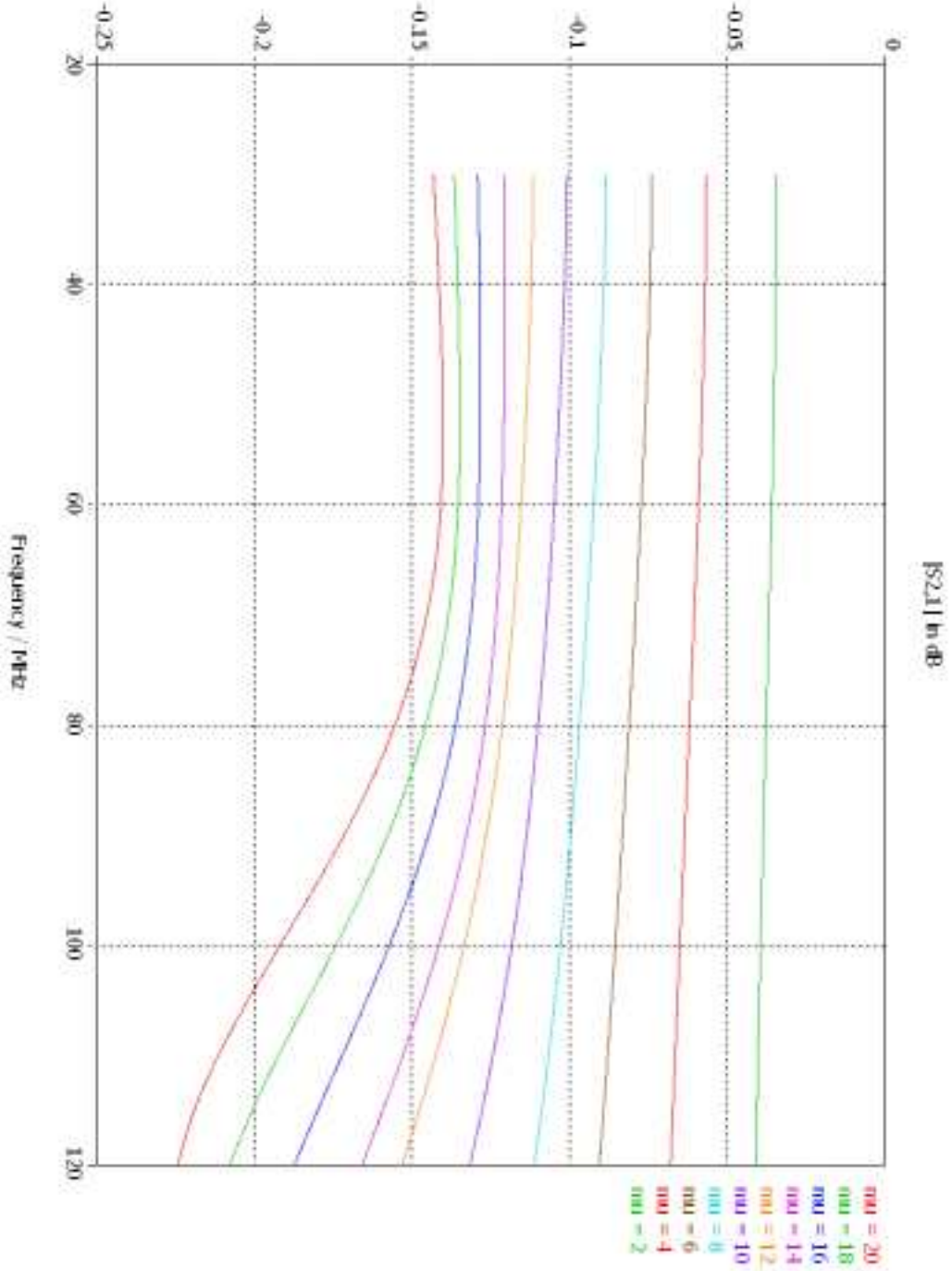

Figure 7-4: Attenuation through the stripline section as μ is varied for a 0.02 loss factor.

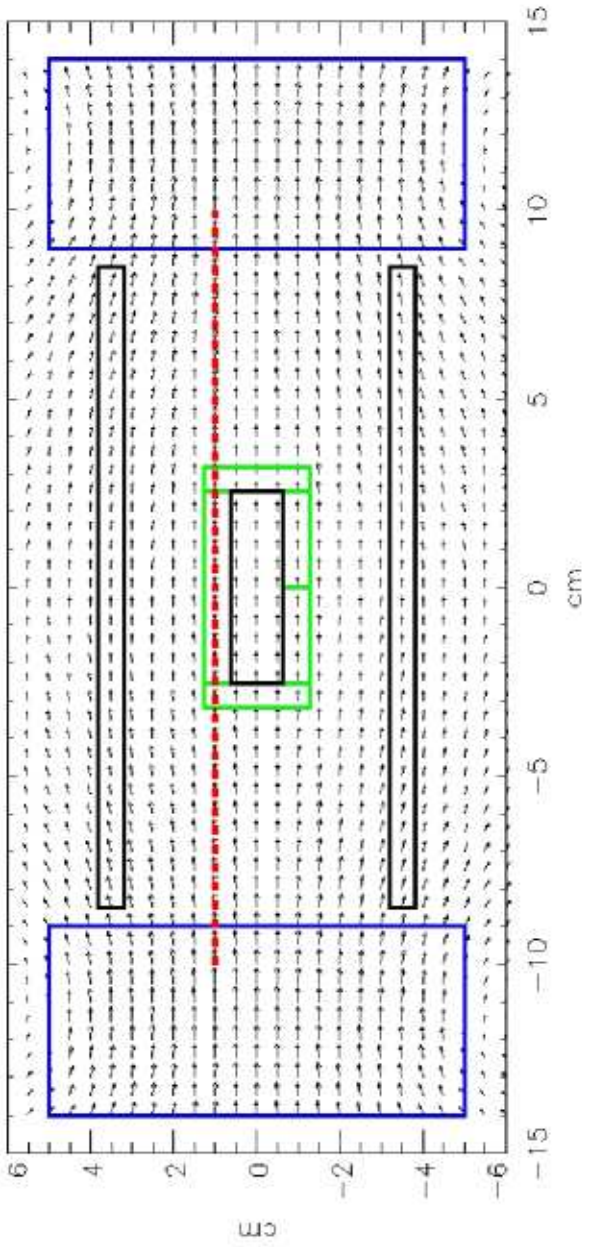

Figure 7-5: Cross section of the stripline with permanent magnets (in blue)

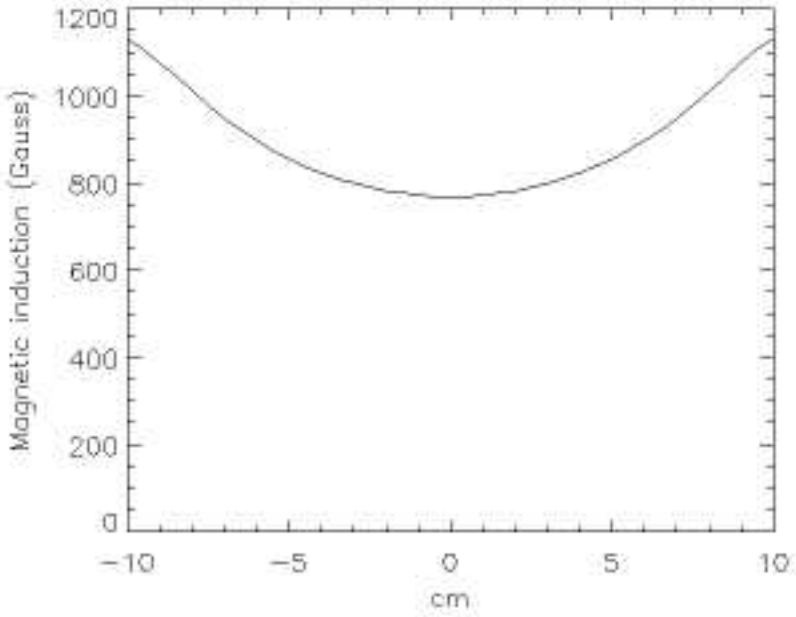

Figure 7-6: Magnetic induction along the red dash line in fi gure 7-5, at the center.

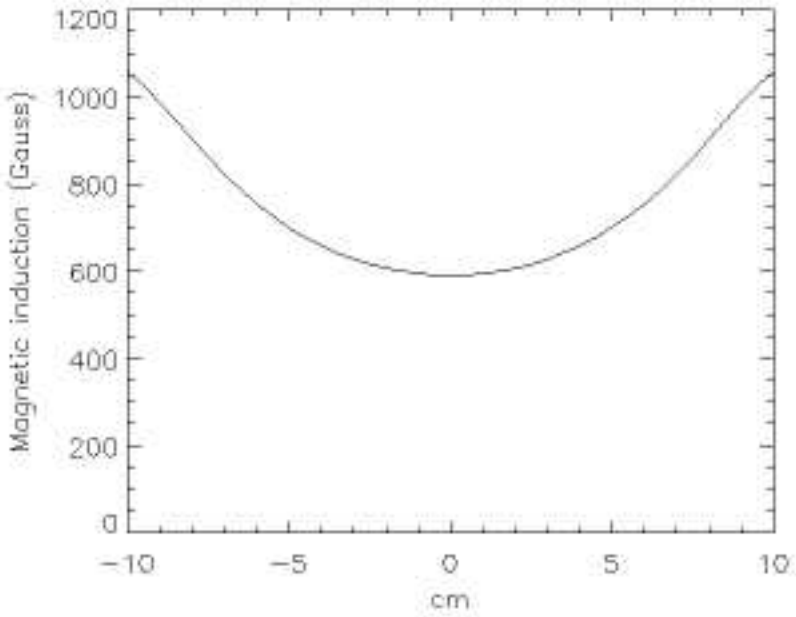

Figure 7-7: Magnetic induction along the red dash line in fi gure 7-5, at the extremity.

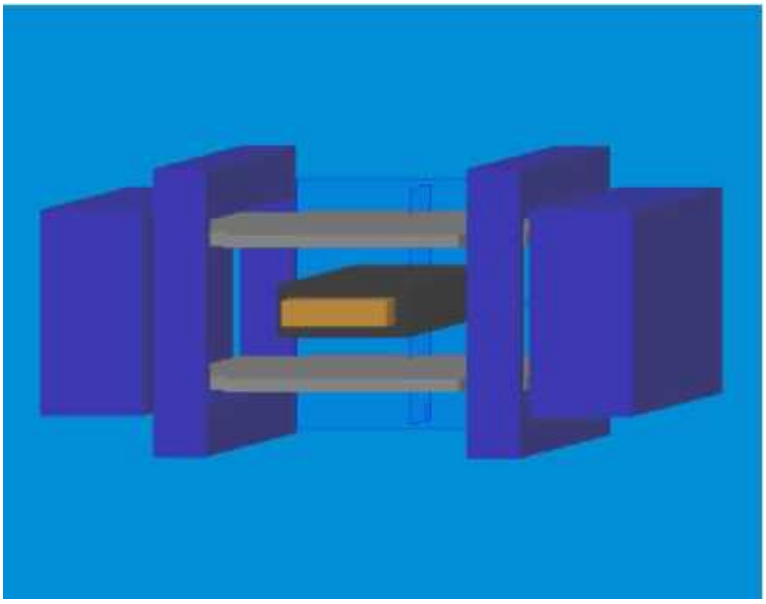

Figure 7-8: Drawing of the tuner assembly, with the inner conductor (orange), ferrite (black), outer conductor (brown) and coils/permanent magnets (blue).

In order to limit the thermal effects of power dissipation, the center conductor may be made out of copper and water-cooled. While the design of a water-cooling system for the stub tuner is rather straightforward, the phase-shifter introduces some complications as the center conductor must be electrically isolated from the outer conductor. The teflon support at both ends of the tuner can be used to connect the water circuit, or a separate isolating tube may be used in the stripline section. The water resistance should also be controlled in order to avoid direct currents along the water. Although a water cooling system may help controlling the temperature in the ferrite slabs, the heat conductivity of most ferrite materials is very low (4 W/m/K). Therefore, even the most effective water-cooling circuit might prove ineffective at controlling the temperature in the outside parts of the ferrite slabs if the power dissipation is too high. This may impose additional limits on the maximum circulating power. As it is diffi cult to predict the effect of temperature rise on the electrical properties of the ferrites, thermal constraints will be determined from high-power tests of the prototype.

7.2.4 Arc protection and detection

Arc detection and protection is also an essential component of a fast-matching system. As presented in chapter 3, the present arc detection on Alcator C-Mod relies on increases of the reflected power on the matched side to track evidences of electrical breakdown in the line. With an impedance matching network which is only adjustable between discharges, this system is robust and efficient. However, with a fast-matching system, the impedance matching may react to the effective loading resulting from arcing phenomena, which casts doubt on the ability of the present system to detect breakdown in these circumstances. The target response time for this work is of the order of the milliseconds, whereas the increase of the reflected coefficient associated with breakdown in the transmission line network occurs typically within a few tens of microseconds. Therefore, we could expect that the fast matching system would be unable to perform the required adjustments in this timescale and so breakdown occurrences would still result in an increase of the reflection coefficient in the matched side. However, during tests with the Fast Ferrite Tuners designed by AFT, the ASDEX team reported that the system was able to *screen* the loading variations resulting from arcs, and therefore the arc detection system used there, which is similar to the C-Mod scheme, was unable to detect the breakdown. This ability to match arcs is most unexpected due to the timescales involved, but arc detection is so critical in high power operations that an investigation of systems fully compatible with fast-matching networks is highly desirable. During the experiment at ASDEX, arcs in the network were not noticed by the operators until smoke detectors in the tokamak cell went off.

Several alternative systems have been proposed for arc detection in coaxial transmission lines. We present here some of the systems which are compatible with an ICRH transmission line network using fast matching technologies. Some proposed schemes include the possibility of arc localization.

Detection by photodiodes

Photodiodes can detect light emission associated with arcs at specific locations in the transmission line network. This method is robust but prohibitive given the lengths to cover. It might be used at known *weak* points in the lines, such as the tuners for example.

Higher frequency test signal [31]

This technique involves the introduction of a low power ($\sim$ 1-10 W) swept frequency signal whose frequency is chosen far above the operating frequency of the transmitters, but below the cutoff frequency for high order modes in the coaxial transmission lines. Arcs are located through changes in the reflected coeffi cients. As presented in [31], the emphasis is more on arc localization than arc detection for fast matching systems. However, this approach might be applicable for matching system, provided that :

- The test signal frequency is such that loading variations in the antenna are small compared to changes in the standing wave pattern resulting from arcs.
- The test signal is not affected by the ferrite tuners.

If these two conditions are met, the only source of changes in the standing wave pattern for the frequency swept test signal would be the effective load introduced by arcs.

Phase measurements

This arc detection scheme is based on the constraints imposed by the physical structure of the network on the phase between RF signals at different locations. For ideal transmission lines, the phase difference induced by propagation of the RF signals depends on the electrical length of the line and the effective loading impedance at the ends of the line if the forward-reflected pattern is not resolved. Breakdown occurrences in the line also affect this pattern signifi cantly over very short timescales, which suggests the potential use of phase measurements for arc detection. Typically, this is done by measuring the phase between voltage probes signals at different location in the network, and faults would be triggered for quick phase variations above a certain threshold.

We have investigated this possible means for arc detection based on the voltage probes installed in the network for D and E. Fast acquisition can given data points every 10 μs. As the existing detection scheme was maintained, the goal was to determine if signifi cant phase changes could be observed before faults were triggered by the present system, or if there was any evidence of undetected arcing. We looked at the derivative of the phase and imposed a threshold compatible with the noise level. Although in some instances this threshold would be exceeded 10 to 20 μs before the faults, in most cases the threshold was

not passed until the forward power started decreasing in the line ; this transient affects the phase balance directly and therefore it was not clear whether the phase balance threshold was exceeded because of breakdown in the line or because of the transient decay of the transmitter output.

More recently, we found evidences that phase balance faults on the J-port network could actually detect arcs before or at the onset of the reflected power increase in some conditions. The reflected power system and phase balance threshold were both increased and an arc started to develop, significant phase changes were induced, above the normal threshold for arc detection. Eventually, the reflected power exceeded the threshold and a fault was triggered. The occurrence of these faults for all possible breakdown locations in the line has not been demonstrated. There is also some evidence that fault balances might be triggered by asymmetric loading in the antenna straps.

Observation of harmonics [32] or low frequency signals

Arcs generate harmonics of the operating frequency which can be detected from probe signals using appropriate frequency filters. If this harmonic signal has higher amplitude that the normal level for this frequency in the system (coming from nonlinearities, pickup from the antenna or harmonics from the transmitter), this scheme can be a robust and efficient arc detection mean. Experimental verifications of this approach have been carried out in TFTR and DIII-D. The conclusions were that, although this system can detect arcs in most conditions, faults do not always correspond to those triggered by VSWR measurements ; furthermore, ELM activity for example can generate higher harmonics in the transmission line.

An alternative is the detection of broadband low frequency signals associated with arcs. This method is based on the same approach as above, but with a different frequency range. Tests at DIII-D suggest that the system can discern between arc signatures and emission of broadband low frequency signals due from sawtooth oscillations for example.

Frequency independent detection [33]

Another alternative for observation of harmonics or broadband low frequency signals is the detection of the broad spectrum signature associated with arc transients, which is a more general approach. Tests at Garching suggest that arc-induced spectrum signatures can be

distinguished from those associated with plasma-induced effects, like ELMs or sawtooth. The applicability for robust arc detection in ICRF networks has not yet been demonstrated.

To date, none of these options have proven to be a satisfactory candidate for arc detection and protection.

Chapter 8

Conclusions and future work

In this thesis, different techniques have been studied and proposed in order to improve the robustness and efficiency of ICRH transmission line systems, with a particular focus on the Alcator C-Mod case. Among the proposed solutions, the load tolerant prematching network and the ferrite tuner fast matching system are the most promising and could lead to a significant improvement over the present network used on the D and E ICRF antennas in the Alcator C-Mod tokamak.

The load tolerant network relies on a particular configuration of the transmission line network or of the antenna structure. The effect of loading variations on the reflection coefficient seen by the generator system can be significantly lowered and the voltage standing wave ratio at the generator could be maintained low for a wide range of operating conditions, including plasmas with Edge Localized Mode or plasmas with different confinement modes (L-mode or H-mode). A prototype can be designed and implemented on the D or E antenna network in C-Mod with little modification and could allow the first experimental test to date of this technique. This assessment is particularly important as the analytic and numerical study of the system highlight potential undesirable effects. Variations in the phase of the reflection coefficient at the antenna port in C-Mod result in an unbalanced current splitting between the different branches leading to the straps. This might deteriorate the system performance due to direct coupling or due to the loss of phasing control. The evaluation of the prototype system under plasma conditions will allow a relevant study of these unwanted effects, together with a proof of principle for the expected behavior and

control of the VSWR.

The load tolerant network could potentially solve the impedance matching problem in ICRF transmission line networks. However, if its performance is unsatisfactory, fast matching systems can be used to perform this task. Several designs have been proposed in the last ten years in the world fusion program, and the most promising is the ferrite-tuner based design, which uses ferrite loaded striplines whose electrical length can be changed over very rapid timescales by varying an external magnetic field. In this thesis, a design was proposed for a ferrite loaded phase shifter capable of reaching acceptable specifications for fast-matching in the Alcator C-Mod tokamak network. A suitable ferrite material was acquired and characterized. The variations in the permeability induced by magnetic fields between 800 and 1500 Gauss are sufficient to obtain a 10 degrees phase shift at 80 MHz over 6 inches, and simulations predict a 45 degrees phase shift at 80 MHz for a 50-cm long ferrite-loaded stripline section. The losses could be maintained under 3 %, which can still create thermal limits for the circulating power. A particular geometry was proposed in order to build a ferrite phase-shifter with appropriate specifications for the Alcator C-Mod D and E antennas. Two main issues remain open concerning its performance : first, the effect of the temperature rise on the mechanical and electrical properties of the ferrites may limit the maximum circulating power well under the electrical breakdown limitations. Second, the existing arc detection system may need to be upgraded ; to date, the different alternatives have not proved to meet acceptable criteria for reliability and robustness.

The design guidelines in this thesis will be used to implement and test both the load tolerant configuration network and the ferrite tuner-based fast matching system on the Alcator C-Mod tokamak. Depending on the schedule of the Alcator group, the evaluation could be done as early as 2004. If the proposed configurations prove feasible, the results will lead to an improved final design of the systems.

Bibliography

[1] WESSON, J., *Tokamaks*, Oxford University Press, 1996.

[2] OWENS, T. et al., ICRF antenna and feedthrough development at the Oak Ridge National Laboratory, volume 129 of *AIP Conference Proceedings*, p. 95, 1985.

[3] RADO, G. T., Review of modern physics **25** (1953) 81.

[4] STIX, T. H., *Waves in plasma*, AIP, 1992.

[5] COLESTOCK, P. et al., J.Vac.Sci.Technol. A **3** (1985) 1211.

[6] STEVENS, J. et al., Plasma Physics and Controlled Fusion **32** (1990) 189.

[7] BURES, M. et al., Plasma Physics and Controlled Fusion **30** (1988) 149.

[8] MYRA, J., Plasma Physics **1** (1994) 2890.

[9] D'IPPOLITO, D. et al., Nuclear Fusion **38** (1998) 1543.

[10] D'IPPOLITO, D. et al., Plasma Physics and Controlled Fusion **33** (1991) 607.

[11] MAYBERRY, M. et al., Nuclear Fusion **30** (1990) 579.

[12] PINSKER, R., Development of impedance matching technologies for ICRF antenna arrays, Technical report, General Atomics, 1998.

[13] F. DURODIE, M. V., First results of the automatic matching device for textor ICRH system, in *Fusion Technology (SOFT)*, pp. 477–480, 1992.

[14] BOSIA, G., Fusion Technology Science and Technology **43** (2003).

[15] REMSEN, D. et al., Feedback controlled hybrid fast ferrites tuners, in *15th IEEE/NPSS Symposium on Fusion Engineering*, 1993.

[16] BRAUN, F. et al., Fast matching of load changes in the ion cyclotron resonance frequency range, in *Sympsosium on Fusion Engineering*, pp. 395–398, IEEE, 25-29 Oct. 1999.

[17] BRAUN, F. et al., Fusion Engineering and Design **56-57** (2001) 551.

[18] NOMURA, G. et al., Feedback control impedance matching system using liquid stub tuner for ion cyclotron heating, in *14th Top. Conf. on RF Power in Plasmas*, pp. 502–503, 2001.

[19] IKEZI, H. and PHELPS, D., Fusion Technology **31** (1997) 106.

[20] PHELPS, D. et al., Advantages of traveling wave antennas for fast wave heating systems, in *12th Top. Conf on RF power in plasmas*, pp. 397–400, 1997.

[21] LAMALLE, P. et al., Commissionning of the wideband matching system for ICRF of ELMy JET plasmas, in AIP, editor, *14th Conf. on RF power in plasmas*, 2001.

[22] WUKITCH, S. et al., Performance of a compact four-strap fast wave antenna, in *19th Fusion Energy Conference, Lyon, France*, IAEA FT/P1-14, 2002.

[23] FRIDBERG, M. et al., Upgrading and operating of the 80 MHz transmitter on the Alcator C-Mod tokamak, in *15th IEEE/NPSS Symposium on Fusion Engineering*, volume 2, p. 1081, 1993.

[24] PARISOT, A. et al., Investigation of the coupling resistance on Alcator C-Mod, Topical Conference on RF Power in plasmas, May 2003, To be published.

[25] COLLIN, R. E., *Foundations for microwave engineering*, McGraw-Hill, 1992.

[26] D'IPPOLITO, D. et al., Nucl. Fusion **38** (1998) 1543.

[27] LAX, B., *Microwave ferrites and ferrimagnetics*, McGraw-Hill, 1962.

[28] CHIKAZUMI, S., *Physics of ferromagnetism - 2nd edition*, Oxford Science Publications, 1997.

[29] GOLDMAN, A., *Modern Ferrite Technology*, Van Nostrand Reinhold, 1990.

[30] http://www.cosmosm.com/cosmosems.htm.

[31] GOULDING, R., Conjugate matching for load-tolerant operation using shorted stubs, ORNL, june 2002.

[32] ROGERS, J. et al., Fusion Engineering **1** (1995) 522.

[33] F. BRAUN, T. S., Fusion Technology (1997) 601.